

**TOWARDS QUANTUM SIMULATION
WITH INTERACTING PHOTONS IN
SUPERCONDUCTING CIRCUITS**

JIRAWAT TANGPANITANON

CENTRE FOR QUANTUM TECHNOLOGIES

2019

**TOWARDS QUANTUM SIMULATION
WITH INTERACTING PHOTONS IN
SUPERCONDUCTING CIRCUITS**

JIRAWAT TANGPANITANON

**A THESIS SUBMITTED
FOR THE DEGREE OF DOCTOR OF PHILOSOPHY
NATIONAL UNIVERSITY OF SINGAPORE
CENTRE FOR QUANTUM TECHNOLOGIES**

Supervisors:

Assoc. Prof. Dimitris G. Angelakis

Examiners:

Prof. Jian-Sheng Wang,

Assoc. Prof. Rainer H. Dumke

Prof. Iacopo Carusotto, Università di Trento

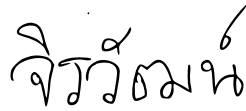
2019

DECLARATION

I hereby declare that the thesis is my original work and it has been written by me in its entirety.

I have duly acknowledged all the sources of information which have been used in the thesis.

This thesis has also not been submitted for any degree in any university previously.



Jirawat Tangpanitanon

7th February 2019

Acknowledgment

I would like to thank my supervisor Prof. Dimitris Angelakis who has trained me not only to be an independent researcher but also a good science communicator for audiences with different backgrounds. I believe that these skills will form an essential basis of my future career. I am also thankful for his generosity for giving me flexibility in exploring various research topics during my Ph.D., as well as extra financial support for my academic trips that goes beyond the usual allowance of my Ph.D. scholarship.

I would like to thank Prof. Dieter Jaksch, who has given me constructive scientific advice and involved in countless discussions since the first year of my Ph.D. His ability to analyze new concepts and to detect flaws during conversations has significantly sharpened my rigorous in science.

I would like to thank Dr. Pedram Roushan, our collaborator from the quantum hardware team at Google, for fruitful discussions and an excellent experiment that led to our joint publication in Science. I am grateful for his time during the discussions which usually happened around his midnight via video calls due to different time zone.

I would like to thank Dr. Victor Bastidas, a former postdoc in our group, who often fought with me during many physics discussions which ended up with beers. All the papers presented in this Thesis has been published with him as a co-author.

I would like to thank my collaborators, Dr. Sarah Al-Assam and Dr. Stephen R. Clark for their significant contributions to the work presented in

this Thesis, our former postdoc, Dr. Ping Ta Ma, for his training on numerical tools that formed a basis of my Ph.D., group members, Dr Changsuk Noh, Dr Changyoun Lee, Dr. Wing Chi Yu, Dr. Marc-Antoine Lemonde, See Tian Feng, and all physicist friends for fruitful discussions.

I would like to thank a few non-physicists friends in Singapore who make me feel like a non-physicist during my Ph.D. These are Charlotte Lim, Korawit Booranakit, Nuri Charoennit and Genevieve Teo, just to name a few.

Last but not least, I am also incredibly grateful for Centre for Quantum Technologies for the scholarship which allowed me to study at the National University of Singapore in the first place.

Contents

Abstract	ix
1 Introduction	1
1.1 Computer simulation	2
1.2 Quantum simulation	2
1.3 Platforms for quantum simulation	5
1.3.1 Cold neutral atoms in optical lattices	5
1.3.2 Trapped ions	6
1.3.3 Solid-state systems	6
1.3.4 Interacting photons	7
1.4 Thesis overview	8
1.5 Contribution and publications	10
2 Background	11
2.1 Quantum phase transitions	11
2.2 Quantum many-body phases of light	16
2.2.1 Light-matter interaction	16
2.2.2 Mott-to-superfluid transition of light in coupled res- onator arrays	23
2.2.3 Driven-dissipative many-body phases of interacting photons	27
2.3 Strongly-interacting photons from superconducting circuits .	33
2.3.1 Microwave photons from an LC circuit	34

2.3.2	A Kerr resonator from a transmon qubit	35
2.3.3	Nonlinear lattices from arrays of coupled transmon qubits	38
3	Spectroscopic signatures of localization with interacting photons in superconducting circuits	40
3.1	Introduction to Many-body localization	41
3.2	The superconducting Gmon chip	44
3.3	Many-body spectroscopy from time evolution	44
3.4	Realization of the Hofstadter’s butterfly	49
3.5	Signatures of a localized to a thermalized transition of interacting photons	52
3.5.1	The Interacting Harper Model	52
3.5.2	The two-photon protocol	53
3.5.3	Level statistics	54
3.5.4	Participation ratio	57
3.6	Effect of missing levels	59
3.7	Conclusions	62
4	Topological pumping of interacting photons in coupled resonator arrays	64
4.1	Introduction to topological pumping	65
4.1.1	Quantized charge transport	65
4.2	The model	68
4.3	Topological transport of Fock states	70
4.4	Effective three-photon hopping.	70
4.5	Robustness of the transport	76
4.6	Circuit QED implementation	78
4.7	Discussion	81

5	Hidden order in driven-dissipative dynamics of interacting photons in coupled resonator arrays	83
5.1	Introduction to Haldane insulator	85
5.1.1	Hidden order in the Spin-1 Heisenberg antiferromagnetic chain	85
5.1.2	The Extended Bose-Hubbard model	87
5.2	The system	89
5.3	Symmetry of the two-photon parametric process	92
5.4	The emergence of the hidden order	96
5.5	Comparison with on-site coherent drive	99
5.6	Implementation of parametric pumping using circuit QED	100
5.7	Conclusion	104
6	Conclusions	105
6.1	Summary of results	105
6.2	Future prospects	106
	Bibliography	108
	Appendix A Field quantization: mode of a simple optical resonator	149
	Appendix B Mean-field description for the interacting Harper model	151
	Appendix C Numerical methods: matrix product states	154

Abstract

Simulating quantum many-body systems on a classical computer generally requires a computational cost that grows exponential with the number of particles. This computational complexity has been the main obstacle to understanding various fundamental emergent phenomena in condensed matters such as high- T_c superconductivity and the fractional quantum-Hall effect. The difficulty arises because even the simplest models that are proposed to capture those phenomena cannot be simulated on a classical computer. Recognizing this problem in 1981, Richard Feynman envisioned a quantum simulator, an entirely new type of machine that exploits quantum coherent and operates by individually manipulating its constituting quantum particles and their interactions. Recent advances in various experimental platforms from cold atoms in optical lattices, trapped ions, to solid-state systems have brought the idea of Feynman to the realm of reality.

Among those, interacting photons in superconducting circuits has been one of the promising platforms thanks to their local controllability and long coherence times. Early theoretical proposals have shown possibilities to realize quantum many-body phenomena of light using coupled cavity arrays such as Mott to superfluid transitions and fractional quantum Hall states. Interacting photons also serve as a natural platform to simulate driven-dissipative quantum many-body phenomena. Recent 72-site superconducting circuits has been fabricated to study a phase transition of light

in the latter scenario.

In this thesis, we first examine the fundamental postulate of thermodynamics and its break down using interacting photons. Specifically, we show how signatures of the celebrated many-body localization transition can be simulated using interacting photons in a nine-site superconducting circuit. The measurements of the relevant energy eigenenergies and eigenstates were done by implementing a many-body spectroscopy method we develop in collaboration with Google Quantum Hardware Group. We benchmark our method first by measuring the Hofstadter butterfly spectrum, which is predicted for two-dimensional electrons moving in a perpendicular magnetic field. Our work introduces a many-body spectroscopy technique to study quantum phases of matter and demonstrate state-of-the-art of high controllability of interacting photons in superconducting circuits.

In the second part of the thesis, we theoretically explore topological pumping with interacting photons for robust quantum state transfer in nonlinear photonic lattices. Our proposal can be implemented with an existing superconducting circuit chip.

In the last part, the existence of hidden long-range order in driven-dissipative lattices as a function of the interplay of different external driving with dissipation is studied. Superconducting circuit implementation of our proposal is discussed in details.

In conclusion, this thesis provides detailed study of the dynamics of quantum many-body systems both in the equilibrium scenario and out-of-equilibrium scenario, including a periodically-driven system, and a driven-dissipative system. The results provide a foundation on which near-term real-world applications of superconducting circuits can be built. Possibilities of applying these results in different areas of quantum technologies are discussed throughout the thesis.

Chapter 1

Introduction

Quantum simulation is an emerging interdisciplinary field in physics [1, 2, 3]. It aims to develop a new type of devices that exploit quantum coherence to answer questions about models that describe complex quantum phenomena that are beyond the reach of a classical computer. Experimental progress in the past 30 years have made it possible to control and manipulate individual quantum systems including trapped ions [4], cold atoms in optical lattices [5], nuclear magnetic resonance (NMR) [6], interacting photons [7], quantum dots [8], superconducting circuits [9], and nitrogen-vacancy centers [10]. These new exciting developments transit quantum simulation from a theoretical proposal to the realm of reality.

In this chapter, we first discuss the concept of simulation on a classical computer, its limitation, and motivation of quantum simulation. We then review various experimental platforms for quantum simulation. We conclude the chapter by giving an overview of the thesis which will be focused on interacting photons in superconducting circuits for quantum simulation of both in and out-of-equilibrium quantum many-body systems.

1.1 Computer simulation

Imitating a complex real-world process or system by simulating corresponding models on a classical computer has been an essential technique for the development of science and technology. To simulate something, one needs first to develop a model that describes characteristics and behavior of such system [11]. By changing variables of the model in the simulator, one can make predictions about the behavior of the simulated systems. These predictions can be used to reduce a high cost of performing several trial-and-error experiments on the real system. For example, the drug design process can be drastically speed up by appropriately modeling the molecular systems [12]. An airplane wing can be designed by simulating relevant drag forces via fluid dynamics models [13].

In some cases, simulation is useful when it is difficult or not possible to perform experiments on a real system. For example, the climate system can be predicted by solving differential equations that represent essential factors of climate and their interactions including atmosphere, oceans, land surface, and ice [14]. We note that the act of simulation itself, i.e., imitating real-world processes or systems, is not necessarily done on a classical computer. For example, simulating a weightless in the outer space can be done by aerobatic maneuvers on the Earth that undergo a parabolic motion [15].

1.2 Quantum simulation

Despite the tremendous success of computer simulation over the past 70 years from the nuclear detonation process in the Manhattan Project in World War II [16] to forecasting of prices on financial markets [17], there remains a large class of systems that are too complex to be simulated by any conceivable classical computer. In physics, this usually involves simulating systems that are non-linear or chaotic due to their non-integrability. In

quantum mechanics, although the Schrodinger equation is a linear equation, simulating it generally requires a computational cost that grows exponential with the number of particles. For example, to describe a wavefunction of N spin-1/2 particles, one needs to store 2^N complex coefficients. Also, one needs to perform linear algebra to such vectors to predict physical observables that describe the dynamics or the ground state of the system. This task can be impossible when N is as small as 50 which requires several petabytes of classical memories [18, 19]. This number is far less than the number of electrons in real materials which can be in the order of 10^{23} . This computational complexity is the main obstacle to understanding various fundamental emergent phenomena such as high- T_c superconductivity [20] and the fractional quantum-Hall effect [21].

Recognizing this problem, in 1981 Richard Feynman envisioned an idea of a quantum simulator, a machine that exploits quantum coherence and operates by individually manipulating its constituting quantum particles and their interactions [22]. Predictions are made by performing appropriate measurements on those particles. Feynman proposed to quantize both space and time to allow such simulator to be universal, i.e., can be programmed to simulate any quantum systems. The idea was later proven by Seth Lloyd in 1996 [23], who proved that by evolving in small time steps, or trotterization, such simulator could simulate the dynamics of any local quantum many-body Hamiltonian with the time scale that grows only polynomially with the number of particles.

Such universal or a ‘digital’ quantum simulator, however, requires full control over quantum many-body systems and may still be a long time ahead. Alternatively, one may aim at a less ambitious goal of an ‘analog’ quantum simulator. The idea is to use reasonably well-controlled quantum systems to simulate only certain classes of quantum systems which are, nevertheless, interesting and cannot be simulated on a classical computer.

Building the later may be less prone to errors because it does not require trotterization and phases of matter are typically robust against local perturbation. Nevertheless, as pointed out in Ref.[2], a functioning quantum simulator should (i) be able to mimic a simple model, or a family of simple models, (ii) simulate models that are of some relevance for applications, (iii) simulate models that are computationally hard for classical computers, and (iv) allow for broad control of the parameters of the simulated model. Also, a quantum simulator should allow for validation, for example, by benchmarking against a classical computer in the regimes where numerical or analytical techniques exist or against different quantum simulators, ideally implemented in different platforms which subjected to different noises.

It might be hard, if not impossible, to prove that a given system cannot be efficiently simulated with a classical computer. Many quantum many-body systems can be simulated on a classical computer with approximate numerical methods such as artificial neural networks [24], tensor networks [25], dynamical mean-field theory, density matrix renormalization group (DMRG) theory [26], density functional theory [27] and quantum Monte-Carlo [28]. However, they are known to be limited to certain classes of problems. For example, DMRG is appreciable only to gapped systems in one dimension. Quantum Monte Carlo does not work with fermionic statistics or frustrated models, due to the sign problem. Mean-field theory only works when the correlation between sites is weak and often fails in one dimension.

With this in mind, the models that benefited most from a quantum simulator are expected to be the ones that involve a large amount of entanglements such as zero-temperature ground states of many-body Hamiltonians near the phase transition, non-equilibrium dynamics of driven or quenched systems, and dissipative dynamics of open systems. A quantum simulator can, for example, rule out or validate candidate models such as the

Fermi-Hubbard model for describing high-temperature superconductivity [29], check the eigenstate thermalization hypothesis with various quantum many-body systems [30], and compute accurate calculations of molecular properties for quantum chemistry [31, 32].

1.3 Platforms for quantum simulation

1.3.1 Cold neutral atoms in optical lattices

Ultracold atoms in optical lattices represent one of the most versatile platforms for quantum simulation [5, 33, 34]. Optical lattices are formed by interfering laser beams in different directions to create a controllable standing-wave pattern that mimics the crystal lattice of a solid. Atoms can be trapped in the optical lattice due to an effective periodic potential landscape induced by laser beams via a dipole moment of the atoms. Ultracold atoms in optical lattices were first used to simulate the celebrated Mott to the superfluid phase transition in the Bose-Hubbard model [35]. Subsequent work has shown quantum gas microscopes which enable fluorescence detection of atoms in single sites [36], quantum magnetism [37], possibilities to create artificial gauge fields by lattice shaking or by laser-induced tunneling [38], and realization of the Fermi-Hubbard model [39, 40, 41, 42]. The Bose-Einstein condensation to Bardeen-Cooper-Schrieffer crossover was also observed in the continuum limit [43]. Recently, cold atoms in optical lattices were recently used to study the breakdown of thermodynamics description of interacting boson gas in two-dimensional disordered lattices [44]. Predicting a thermalized to a many-body localized phase transition in such a system is currently not possible with a classical computer due to the lack of efficient numerical techniques. A quantum simulator with 51-cold atoms trapped using optical tweezers has also been realized to observe different ordering in quantum Ising model [45].

1.3.2 Trapped ions

An alternative approach for atom-based quantum simulators is the use of trapped atomic ions held in linear radio-frequency traps [46, 47]. Here ion crystals are formed by balancing the Coulomb repulsion between ions and trap confinement force, allowing them to be accurately controlled and manipulated. A wide range of models have been simulated in trapped ion systems from spin models [48, 49], to dynamical phase transitions [50] and discrete time crystal [50]. High controllability in trapped ions also makes it a promising platform for quantum computing [51, 52]. The number of ions in a quantum simulator varies by a large factor depending on their controllability. For example, in 2012 a few hundreds of trapped ions with no local control was used to realize the quantum Ising model [53], while a fully-programmable quantum simulator was only recently realized with five atoms in 2016 [54]. This controllability is also a crucial factor for building a scalable quantum simulator in addition to the number of constituting atoms. Building a scalable quantum processor with high controllability and long coherent time over a few hundred qubits and defining relevant real-world applications are near-term challenges faced by all quantum technologies platforms [55].

1.3.3 Solid-state systems

There are also platforms for quantum simulation that based on solid state systems. For example, nitrogen-vacancy centers in diamond have been recently used to observe signatures of discrete time crystal [45]. Donor spins in silicon have been used together with Nuclear Magnetic Resonance technique to demonstrate quantum gates between two qubits [6]. A programmable quantum processor consisting of two single-electron-spin qubits in a silicon/silicon germanium (Si/SiGe) double quantum dot has been illustrated [56]. The Fermi-Hubbard model has also been simulated using a

quantum dot array in a GaAs/AlGaAs heterostructure semiconductor [8].

1.3.4 Interacting photons

In parallel to the above progress, a new type of quantum simulators based on photons and hybrid light-matter excitations, known as polaritons, has been slowly emerging [57, 58], inspired by advances in the field of quantum nonlinear optics and cavity quantum electrodynamics (QED) in the last two decades [7]. Pioneer theoretical works have shown possibilities to realize strongly correlated states of lights in coupled resonator arrays (CRAs) and to observe the Mott to the superfluid phase transition of light [59, 60, 61]. Subsequent works extend the results to a family of many-body phenomena including an artificial field for the fractional quantum Hall effect [62, 63, 64], effective spin models [65, 66, 67, 68], and topological transport of quantum states [69]. Signatures of localization of interacting photons in a quasi-periodic potential have recently been observed with a nine-site superconducting circuit by directly measuring statistics of eigenenergies and spreading of energy eigenstates [70]. The latter will be discussed in Chapter 3 in details.

In complementary with cold atoms, interacting photons provide a natural setting for simulating open quantum systems because light-matter systems dissipate to the environment and because they can be driven both coherently and incoherently. The coupling to the environment is usually weak, and the bath is memoryless. Consequently, the system may reach a dynamically-stable steady state that depends on the symmetries of the system [71]. Early theoretical works have shown that such steady states manifest various quantum many-body phases [72, 73, 74, 75, 76, 77] and can exhibit dissipative phase transitions (DPT) [78, 79]. A nonlinear superconducting circuit has recently been fabricated to study DPT with light [80].

We note that there is also active research in the field of exciton polaritons in semiconductor materials, realizing quantum fluid of light [81]. However, the interaction strength of such a system is typically weak at a few-photon level. Nevertheless, there are possibilities to enhance such interaction, for example, by resonantly coupling a pair of cavity polaritons to a biexciton state [82]. Experiments in this platform have led to realization of exotic phases of matter such as non-equilibrium Bose-Einstein condensation [83, 84] and non-equilibrium polariton superfluidity [85, 86].

Interacting photons in superconducting circuits

Perhaps, the most promising platform for realizing interacting photons is superconducting circuits where conventional optical and electron-beam lithography is used, allowing CRAs to be designed with great flexibility and high controllability [9]. The circuit is made superconducting by cooling to few milli-Kelvins using a dilution refrigerator. Photonic modes can be realized from the co-planar transmission line or an LC circuit which effectively acts as a Fabry-Perot microwave cavity [87]. An ‘artificial’ two-level atom can be made from the use of Josephson junctions [88]. Both strong coupling [89] and ultra-strong coupling [90] between an artificial atom and transmission line have also been reported. A small size non-linear coupled resonator arrays have been implemented [70, 91, 92].

1.4 Thesis overview

This thesis is concerned with the use of interacting photons in superconducting circuits for quantum simulation of in and out of equilibrium quantum many-body phenomena. It is organized as follows.

In Chapter 2, we review the basic concept of quantum phase transition with a specific example of the Mott to the superfluid phase tran-

sition in the Bose-Hubbard model. We then discuss the basic concepts in light-matter interaction, including field quantization in a cavity QED, the Jaynes-Cummings model, and photon blockade. We then consider the early proposal for Mott to superfluid transitions of light and review various works on realizing both equilibrium and driven-dissipative many-body phases of light in CRAs. Lastly, we discuss circuit quantization and recent experimental progress in achieving interacting photons in superconducting circuits.

In Chapter 3, we show how signatures of the celebrated many-body localization transition can be simulated using interacting photons in a nine-site superconducting circuit. The measurements of the relevant energy eigenenergies and eigenstates were done by implementing a novel many-body spectroscopy method based on time evolution we develop in collaboration with Google Quantum Hardware Group. Our approach was benchmarked by measuring the energy spectrum predicted for the system of electrons moving in two dimensions under a strong magnetic field - the Hofstadter butterfly. Our work introduces a many-body spectroscopy technique to study quantum phases of matter and demonstrate state-of-the-art of high controllability of interacting photons in superconducting circuits.

In Chapter 4, we show how to implement topological or Thouless pumping of interacting photons in one-dimensional nonlinear resonator arrays, by simply modulating the frequency of the resonators periodically in space and time. The interplay between interactions and the adiabatic modulations enables robust transport of Fock states with few photons per site. We analyze the transport mechanism via an effective analytic model and study its topological properties and its protection to noise. The transport can be used to probe topological phases of interacting systems. We conclude by a detailed study of implementation with existing circuit QED architectures.

In Chapter 5, we study the dynamics of nonlinear photonic lattices

driven by two-photon parametric processes. By means of matrix-product-state based calculations, we show that a quantum many-body state with long-range hidden order can be generated from the vacuum. Although this order resembles that characterizing the Haldane insulator, our system is far from equilibrium due to the drive and photon loss. A possible explanation highlighting the role of the symmetry of the drive, and the effect of photon loss are discussed. An implementation based in superconducting circuits is proposed and analyzed.

1.5 Contribution and publications

Here I summarise my contribution to the work presented in this thesis.

- The work in Chapter 3 led to the publication of *Spectroscopic Signatures of Localization with Interacting Photons in Superconducting Qubits* [70], for which I provided theoretical support for the experiment and equally contributed to the work with the first author.
- The work in Chapter 4 led to the publication *Topological Pumping of Photons in Nonlinear Resonator Arrays* [69], for which I was the first author.
- The work in Chapter 5 led to the publication *Hidden Order in Quantum Many-body Dynamics of Driven-Dissipative Nonlinear Photonic Lattices*, for which I was the first author.

Chapter 2

Background

2.1 Quantum phase transitions

Identifying phases of matter are one of the main goals in condensed matter and material science. During a phase transition of a given material, specific properties of the material change abruptly as a result of the change of some external parameters. In classical physics, these parameters could be, for example, temperature, pressure, electric or magnetic fields. Classical phase transitions are driven by thermal fluctuations and cease to exist at zero temperature. Quantum phase transitions (QPTs), on the other hand, exist at zero temperature and are driven by quantum fluctuations according to Heisenberg uncertainty principle [93]. Although, strictly speaking, absolute zero temperature is not physically realizable, signatures of QPTs can be observed when the energy scale of the thermal fluctuation $k_B T$ is much smaller than that of the quantum fluctuations $\hbar\omega$, where ω is a typical frequency of the quantum oscillation.

To concretize the above description of QPT, let us consider a Hamiltonian of the form

$$\hat{H} = \hat{H}_1 + g\hat{H}_2, \quad (2.1)$$

where g is a dimensionless parameter. The QTP concerns with non-analytic

dependence of the ground-state energy $E(g) = \langle G | \hat{H} | G \rangle$ as the parameter g changed. Here $|G\rangle$ is the ground state of the system, i.e. $\hat{H}|G\rangle = E(g)|G\rangle$. In the case of $[\hat{H}_1, \hat{H}_2] = 0$, non-analyticity can happen due to crossing of eigenvalues. In the case of $[\hat{H}_1, \hat{H}_2] \neq 0$, non-analyticity can happen due to the closing of the energy gap between the ground state and the first excited state which happens in the thermodynamic limit. The latter is more common and has a closer analogy to classical phase transitions, while the former often occurs in conjunction with the latter. The QPT is usually accompanied by an abrupt change in the correlations in the ground state.

Example: the Mott-to-superfluid phase transition

The Fermi-Hubbard model was originally proposed in 1963 by Hubbard [94] to approximately describe a conducting to an insulating QPT of electrons in solids. Its bosonic version was proposed in the same year by Gersch and Knollman [95] and named the Bose-Hubbard model. The phase diagram of the latter was first calculated in 1989 [96] and the corresponding QPT was realized in cold atoms in optical lattices in [35]. Specifically, the Bose-Hubbard (BH) model describes the system of N bosonic particles moving on a lattice consisting of L lattice sites,

$$\hat{H}_{\text{BH}} = -J \sum_{\langle i,j \rangle} \hat{a}_i^\dagger \hat{a}_j - \mu \sum_{i=0}^{L-1} \hat{n}_i + \frac{U}{2} \sum_{i=0}^{L-1} \hat{n}_i (\hat{n}_i - 1), \quad (2.2)$$

where \hat{a}_j (\hat{a}_j^\dagger) is a bosonic annihilation (creation) operator at site i , $\hat{n}_i = \hat{a}_i^\dagger \hat{a}_i$ is the number operator at site j , $\langle \dots \rangle$ denotes the sum over nearest-neighbour, J is the hopping strength between site i and j , μ is the chemical potential, and U is the on-site interaction. The first term in Eq. 2.2 describes kinetic energy of particles, the second term determines the number of particles in the ground state, and the last term describes interaction between particles.

To understand different phases exhibited by the BH model, let us first consider the limit $J = 0$. In this case, \hat{H}_{BH} reduces to the sum of on-site Hamiltonians, i.e. $\hat{H}_{\text{BH}} = \sum_j \hat{h}_j$, where $\hat{h}_j = -\mu \hat{n}_j + \frac{U}{2} \hat{n}_j(\hat{n}_j - 1)$. Hence, the ground state takes the form of a product state $|G\rangle = \prod_j |n\rangle_j$, where $|n\rangle_j$ is an n -particle Fock state at site j , i.e. $\hat{n}_j |n\rangle_j = n |n\rangle_j$. The corresponding ground state energy is $E(n) = L [-\mu n + \frac{U}{2} n(n - 1)]$. As shown in Fig. 2.1(b), there are different level crossing between states with different integer fillings n for $\mu = nU$. The ground state has an energy gap, hence they should be stable against small changes in the Hamiltonian such as small tunneling. This integer-filling ground states are known as Mott insulating states.

Another phase can be revealed by considering the limit $U = 0$, where the Hamiltonian is reduced to the tight-binding model $\hat{H}_{\text{tight-binding}} = -J \sum_{\langle i,j \rangle} \hat{a}_i^\dagger \hat{a}_j - \mu \sum_j \hat{n}_j$. The Hamiltonian can be diagonalized by applying the quantum Fourier transform $\hat{a}_k = \frac{1}{\sqrt{L}} \sum^{ikj} \hat{a}_j$. The Hamiltonian is then casted into the form $\hat{H}_{\text{tight-binding}} = \sum_k \omega_k \hat{a}_k^\dagger \hat{a}_k$, where ω_k is a constant depending on μ and k . For example, for a one-dimensional periodic lattice, we have $\omega_k = -\mu - 2J \cos(k)$. For $\mu, J > 0$, the ground state is then $|G\rangle = (\hat{a}_{k=0}^\dagger)^N |000\dots\rangle$ which is a product state in the momentum space, not in the position space as in the Mott. This state is known as the superfluid state.

The mean-field phase diagram

Now let us consider an approximate method to calculate the many-body phases for the full range of J/U . The key idea is to decompose $\hat{a}_j = \psi + \delta\hat{a}_j$, where $\delta\hat{a}_j$ is the fluctuation from the mean value $\psi \equiv \langle \hat{a}_j \rangle$. The mean-field approximation proceeds by dropping the second order terms in $\delta\hat{a}_j$ in the Hamiltonian, assuming that correlations between sites can be ignored. This approximation becomes exact in infinite dimensions, but often fails in

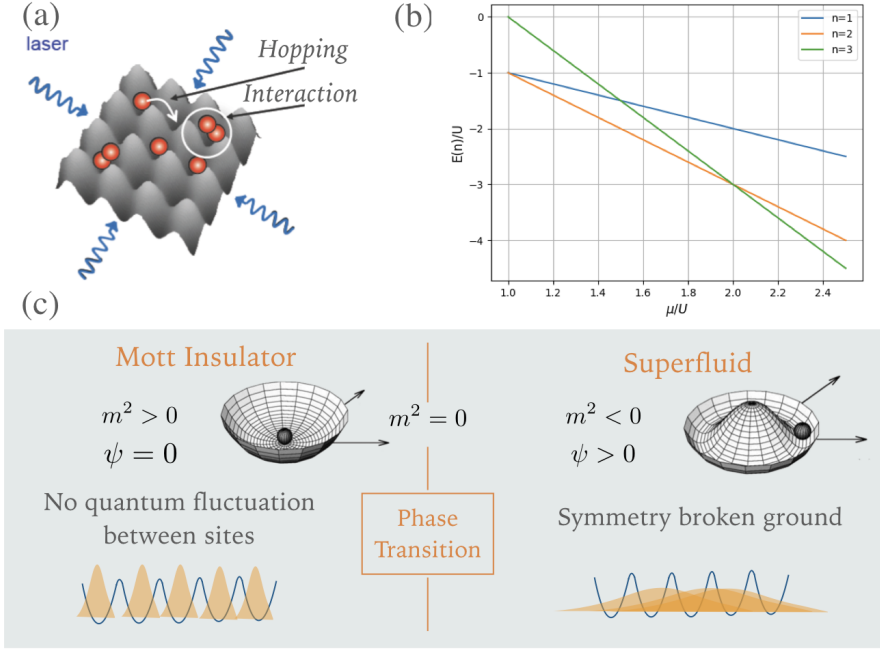


Fig. 2.1. **The Bose-Hubbard model.** (a) A sketch of cold atoms in optical lattices realizing the Bose-Hubbard model. (b) The mean-field energy as a function of μ/U for three different numbers of particles $n = 1, 2, 3$. The mean-field energy landscape in the Mott and the superfluid phase are shown in (b) and (c), respectively.

one-dimension. To see how this leads to the sum of approximated on-site Hamiltonians, let us write the hopping term as

$$\begin{aligned}
\hat{a}_i^\dagger \hat{a}_j + H.c. &= (\psi^* + \delta \hat{a}_i^\dagger)(\psi + \delta \hat{a}_j) + H.c. \\
&= \psi^* \psi + \delta \hat{a}_i^\dagger \psi + \psi^* \delta \hat{a}_j + \delta \hat{a}_i \delta \hat{a}_j + H.c. \\
&\approx \psi^* \psi + \delta \hat{a}_i^\dagger \psi + \psi^* \delta \hat{a}_j + H.c. \\
&\approx \psi^* \psi + (\hat{a}_i^\dagger - \psi^*) \psi + (\hat{a}_j - \psi) \psi^* + H.c. \\
&\approx \hat{a}_i^\dagger \psi + \hat{a}_j^\dagger \psi - \psi \psi^* + H.c.. \tag{2.3}
\end{aligned}$$

The full Hamiltonian is then written as $\hat{H}_{\text{BH}} \approx \hat{H}_{\text{BH}}^{\text{MF}} = \sum_j (\hat{h}_j^{(0)} + \hat{V}_j)$ where $\hat{h}_j^{(0)} = -\mu \hat{n}_j + \frac{U}{2} \hat{n}_j (\hat{n}_j - 1) - Jz \psi^* \psi$ and $\hat{V}_j = -Jz(\psi^* \hat{a}_j + \psi \hat{a}_j^\dagger)$ with z being the coordination number, or the number of sites connected to site j via the hopping term. We then write the mean-field energy as $E_n = E_n^{(0)} + E_n^{(1)} + E_n^{(2)} + \dots$. By doing perturbation theory with respect

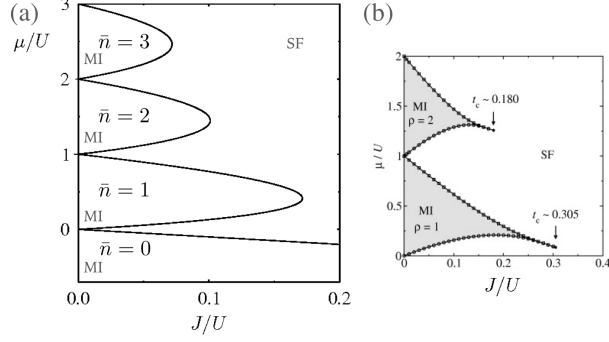


Fig. 2.2. **Phase diagram of the Bose Hubbard model.** The mean-field phase diagram showing the Mott and the superfluid phase is shown in (a). A more exact phase diagram calculated from DRMG for the one dimensional system is shown in (b). The result is reproduced from Ref. [97]

to the V -term, the zero order eigenenergy is

$$E_n^{(0)} = \begin{cases} 0 & \text{for } \mu < 0 \\ -\mu n + \frac{U}{2}n(n-1) + Jz\psi^2 & \text{for } U(n-1) < \mu < Un \end{cases} \quad (2.4)$$

The first order eigenenergy is zero $E_1^{(1)} = \langle n | \hat{V}_j | n \rangle = 0$. The second order eigenenergy is

$$E_n^{(2)} = \psi^2 \sum_{n'} \frac{|\langle n | \hat{V}_j | n' \rangle|^2}{E_n^{(0)} - E_{n'}^{(0)}} = (Jz\psi)^2 \left(\frac{u}{U(n-1) - \mu} + \frac{n+1}{\mu - Un} \right). \quad (2.5)$$

The mean-field energy is then $E_n = \text{const.} + m^2\psi^2 + \dots$ where

$$\frac{m^2}{Jz} = 1 + \frac{n}{\tilde{U}(n-1) - \tilde{\mu}} + \frac{n+1}{\tilde{\mu} - \tilde{U}n}, \quad (2.6)$$

with $\tilde{\mu} = \mu/Jz$ and $\tilde{U} = U/Jz$.

As shown in Fig. 2.1(c)-(d), for $m^2 > 0$ E_n is minimized when $\psi = 0$. Hence the ground state has $U(1)$ symmetry, i.e., invariant under the transformation $\psi \rightarrow e^{i\theta}\psi$, and no quantum fluctuation between sites corresponding to the Mott insulating states. For $m^2 < 0$, E_n is minimized when $\psi \neq 0$, implying that the ground state has a broken $U(1)$ symmetry corresponding to the superfluid state. The phase boundary can be computed

by solving the equation $m^2 = 0$. The corresponding mean-field phase diagram is shown in Fig. 2.2(a). Fig. 2.2(b) shows the phase diagram for a one-dimension Bose-Hubbard lattice calculated by a more exact density-matrix-renormalization-group (DMRG) technique [97], taking into account correlations between sites. We can see that the mean-field theory can give a qualitative approximation of the phase diagram.

2.2 Quantum many-body phases of light

2.2.1 Light-matter interaction

Having discussed phases of matter, we now turn to experimental realization of photon-photon interactions and how many-body phases of light can emerge. Engineering strong interactions at progressively low light intensity has been one of the greatest challenges in optical science. In classical regime, photon-photon interaction is achieved by shining an intense light beam to a non-linear material so that optical properties of the material such as refraction and absorption are modified and, in turn, lead to power-dependent light propagation through the material [98]. Specifically, polarization \mathbf{P} of non-linear media, defined as dipole moments per unit volume, can be written as

$$\mathbf{P}/\epsilon_0 = \chi^{(1)}\mathbf{E} + \chi^{(2)}\mathbf{E}^2 + \chi^{(3)}\mathbf{E}^3 + \dots, \quad (2.7)$$

where ϵ_0 is the electric permittivity of free space, χ^i is the electric susceptibility of order i^{th} , and \mathbf{E} is the input electric field. The higher order terms account for non-linear optical phenomena such as second or higher harmonic generation, sum-frequency generation, self-focusing, and optical solitons. However, as the light intensity is weaker, the higher order terms in Eq. 2.7 are suppressed, and eventually, the material only exhibits a linear

response, making it difficult to achieve strong interaction at a few photon levels.

Another way to see this is to consider the probability p of one photon getting absorbed by an atom. At resonance, this probability is maximized and proportional to the ratio between the wavelength of light squared (λ^2) and the transverse area of the laser beam (d^2), i.e., $p \sim \lambda^2/d^2$. The number of atoms required to modify one photon is then $N \approx 1/p$. Due to the diffraction limit that prevents the focusing of the light beam below the wavelength, this probability is typically small $p \ll 1$. Recent experiments have achieved $p \approx 0.01 - 0.1$ by concentrating laser light to a small area [99, 100, 101, 102].

In the limit $p \rightarrow 1$, the presence of one atom can substantially modify a single incident photon. Since a single two-level atom can only absorb one photon at a time, a pair of incident photons will experience an atomic response that is very different from that of a single photon, hence realizing nonlinearity at the two-photon level. One way to achieve this is to use a reflective cavity that enhances the interaction probability p by the number of bounces, F , that the photon makes inside the cavity before leaking out. The probability p approaches unity when $\eta \gg 1$, where $\eta = F\lambda^2/d^2$ is called the cooperativity.

The Jaynes-Cummings interaction

The system consisting of a two-level atom interacting with photons trapped in an optical cavity, as shown in Fig. 2.3, is described by the Hamiltonian

$\hat{H}_{\text{JC}} = \hat{H}_{\text{cavity}} + \hat{H}_{\text{atom}} + \hat{H}_{\text{int}}$, where

$$\hat{H}_{\text{cavity}} = \omega_c \left(\hat{a}^\dagger \hat{a} + \frac{1}{2} \right) \quad (2.8)$$

is the Hamiltonian of the cavity. ω_c is the fundamental frequency of the cavity. \hat{a}^\dagger (\hat{a}) is a bosonic creation (annihilation) operator, i.e. $[\hat{a}, \hat{a}^\dagger] = 1$

($\hbar = 1$). The two-level atom is described as

$$\hat{H}_{\text{atom}} = \omega_a \hat{\sigma}^+ \hat{\sigma}^-, \quad (2.9)$$

where $\hat{\sigma}^+ = |e\rangle\langle g|$ and ω_a is the energy different between the two eigenstates. The atom interacts with the cavity mode by a dipole transition operator which is defined as $\hat{\mathbf{d}} = \mathbf{d}^* \hat{\sigma}^+ + \mathbf{d} \hat{\sigma}^-$, where \mathbf{d} is the dipole moment. The interaction between the atom and the cavity is described by the dipole interaction.

$$\begin{aligned} \hat{H}_{\text{int}} &= -\hat{\mathbf{d}} \cdot \hat{\mathbf{E}}(z, t) \\ &= -E_0 (\hat{a} + \hat{a}^\dagger) \sin\left(\frac{\pi z}{L}\right) \hat{d} \\ &= g (\hat{\sigma}^+ + \hat{\sigma}^-) (\hat{a} + \hat{a}^\dagger) \\ &= g (\hat{\sigma}^\dagger \hat{a} + \hat{\sigma}^- \hat{a} + \hat{\sigma}^+ \hat{a}^\dagger + \hat{\sigma}^- \hat{a}^\dagger), \end{aligned} \quad (2.10)$$

where $g = -E_0 \sin(\frac{\pi z}{L})$ is the light-matter coupling constant. E_0 is the amplitude of the field in the cavity of length L . z is the position in the cavity. See App. A for the details of field quantization in the cavity. We can see that \hat{H}_{int} contains terms that do not conserve the number of excitation. To see the effect of these terms, we move from the Schrödinger picture into the interaction picture defined by $\hat{H}_{\text{cavity}} + \hat{H}_{\text{atom}}$, i.e.

$$\begin{aligned} \hat{H}_{\text{int}}(t) &= e^{i(\hat{H}_{\text{cavity}} + \hat{H}_{\text{atom}})t} \hat{H}_{\text{int}} e^{-i(\hat{H}_{\text{cavity}} + \hat{H}_{\text{atom}})t} \\ &= g (\hat{a} \hat{\sigma}^- e^{-i(\omega_c + \omega_a)t} + \hat{a} \hat{\sigma}^+ e^{i(\omega_a - \omega_c)t} + H.c.). \end{aligned} \quad (2.11)$$

The terms $\hat{a} \hat{\sigma}^-$ and $\hat{a} \hat{\sigma}^+$ describe an emission and an absorption process respectively. They oscillate with a slow frequency $\omega_a - \omega_c$, while the counter-rotating terms ($\hat{a} \hat{\sigma}^- e^{-i(\omega_c + \omega_a)t} + H.c.$) do not conserve number of excitations and quickly oscillates. When $|\omega_c - \omega_a|, g \ll \omega_c + \omega_a$, the latter terms can be ignored, giving rise to a solvable model known as the Jaynes-Cummings

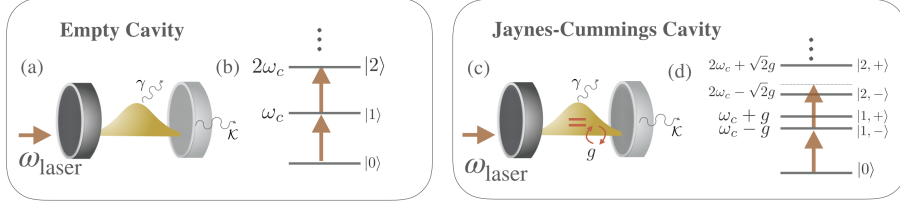


Fig. 2.3. **The Jaynes-Cummings model.** (a) A sketch of an empty cavity with (b) its linear spectrum. When the modes of the cavity coupled to the two-level system, the total system is described by the Jaynes-Cummings model (c). The resulting energy spectrum has non-linear splitting proportional to $g\sqrt{n}$. An external laser with frequency $\omega_{\text{laser}} = \omega_c - g$ will resonant with the one-excitation state $|1, -\rangle$ but off-resonant with the two-excitation state $|2, -\rangle$ leading to the photon blockade effect where only one photon can enter the cavity.

(JC) model [103, 104] first envisioned in 1963. This approximation is known as the rotating-wave approximation. The JC model is then written as

$$\hat{H}_{\text{JC}} = \omega_a \hat{\sigma}^+ \hat{\sigma}^- + \omega_c \hat{a}^\dagger \hat{a} + g(\hat{a}^\dagger \hat{\sigma}^- + \hat{a} \hat{\sigma}^+). \quad (2.12)$$

Eigenstates of the Jaynes-Cummings model

To obtain the eigenstates and the eigenenergies of the JC model, we first notice that the Hamiltonian \hat{H}_{JC} commutes with the total number excitation operator $\hat{N} = \hat{\sigma}^+ \hat{\sigma}^- + \hat{a}^\dagger \hat{a}$. For n excitations, there are only two possible states which are (i) $|\psi_1\rangle = |n-1, e\rangle$ with $n-1$ photons in the cavity and the atom is in the excited state and (ii) $|\psi_2\rangle = |n, g\rangle$ with n photons in the cavity and the atom is in the ground state. The matrix elements of \hat{H}_{JC} in this subspace, $H_{\text{JC},ij}^{(n)} = \langle \psi_i | \hat{H}_{\text{JC}} | \psi_j \rangle$ for $i, j \in \{1, 2\}$, are written as

$$\hat{H}_{\text{JC}}^{(n)} = \begin{pmatrix} (n-1)\omega_c + \omega_a & g\sqrt{n} \\ g\sqrt{n} & n\omega_c \end{pmatrix}. \quad (2.13)$$

Diagonalizing this Hamiltonian, we obtain the energy eigenstates as

$$E_{\pm}(n) = \omega_c \left(n - \frac{1}{2} \right) \pm \frac{1}{2} \sqrt{(\omega_a - \omega_c)^2 + g^2 n}. \quad (2.14)$$

with the energy eigenstates

$$\begin{aligned} |n, +\rangle &= \cos\left(\frac{\alpha_n}{2}\right) |n-1, e\rangle + \sin\left(\frac{\alpha_n}{2}\right) |n, g\rangle, \\ |n, -\rangle &= -\sin\left(\frac{\alpha_n}{2}\right) |n-1, e\rangle + \cos\left(\frac{\alpha_n}{2}\right) |n, g\rangle, \end{aligned} \quad (2.15)$$

where $\alpha_n = \tan^{-1}(2g\sqrt{n}/(\omega_a - \omega_c))$. Excitations in $|n, \pm\rangle$ are a collective mode of photonic and atomic excitations called polariton. The cavity is said to be a non-linear cavity because its eigenenergies now have non-linear dependence in n . The non-linearity becomes maximized at resonance $\omega_a = \omega_c$, i.e. $E_{\pm}(n) = \omega_c(n - 1/2) \pm \frac{1}{2}g\sqrt{n+1}$. In the large detuning limit $|\omega_a - \omega_c| \gg g\sqrt{n}$, the eigenenergies becomes approximately linear in n , i.e. $E_{\pm}(n) \approx \omega_c n \pm \frac{1}{2}|\omega_a - \omega_c|$. In this limit, the cavity modes are decoupled from the atom. In addition, the spectrum is also approximately linear for a large number of photons $n \gg 1$ where $\sqrt{n+1} \approx \sqrt{n}$ since an energy gap between adjacent energy levels are approximately the same, e.g. $E_{\pm}(n+2) - E_{\pm}(n+1) \approx E_{\pm}(n+1) - E_{\pm}(n) \approx \omega_c \pm \frac{1}{2}g\sqrt{n}$.

Early experimental realizations of strong light-matter coupling

Signatures of the atom-cavity interaction were first observed in the 1980s via the change in the spontaneous emission rate of an atom when placed in a cavity [105, 106, 107]. The cavity mode is said to be ‘strongly coupled’ to the atom when the light-matter coupling is much larger than dissipation rate both to the input and the output waveguides \mathcal{K} and to free space γ , i.e., $g^2 > \mathcal{K}\gamma$. In this limit, a single photon in the cavity has enough coherent time to allow reversible exchange between the atomic and the photonic excitation before irreversibly leaking out the cavity. Signatures of the strong light-matter interaction were first observed in the optical regime in 1992 via normal mode splitting [108] and in the microwave regime in 1996 via quantum Rabi oscillation [109]. The former led to the first experimental

demonstration that single atoms can introduce a phase shift to a single photon by approximately $\pi/10$ [110], while the latter led to the generation of Einstein-Podolsky-Rosen pair of atoms in a controllable manner [111]. In superconducting systems, strong coupling between a single artificial atom and a single microwave photon was later realized in 2004 [89].

Photon blockade effect

Photon blockade refers to a situation in which interaction between photons is so strong that the presence of a single photon in a cavity can completely ‘block’ another photon from entering the cavity. The term is used in analogy to the Coulomb blockade effect [112] where a single electron on a small metallic or semiconductor device can block the flow of another electron when the charging energy is much larger than the thermal energy. To understand photon blockade in the Jaynes-Cummings model, imagine the cavity and the atom is initially in the vacuum state and the ground state, respectively, i.e., $|0, g\rangle$. A laser beam is then shined to the system with the frequency that is resonant with one of the one-excitation eigenstates, e.g., $\omega_{\text{laser}} = E_-(1) = \omega_c - \frac{1}{2}g$ (assuming $\omega_a = \omega_c$). Due to the resonance condition, the first photon that enters the cavity will excite the cavity to the state $|1, -\rangle$. However, the frequency of the second photon is now off-resonant with that of the two-excitation state $|2, -\rangle$, $E_{\pm}(2) - E_-(1) = \omega_c \mp \frac{1}{2}g(\sqrt{2} \mp 1) \neq \omega_{\text{laser}}$. Hence the second photon is prevented from entering the cavity and the two photons effectively ‘repel’ each other. The first experimental breakthrough that showed direct signatures of photon blockade was done in 2005 [113], through the anti-bunching statistics of transmitted photons, see Fig. 2.4. The result marks an exciting new era in nonlinear quantum optics.

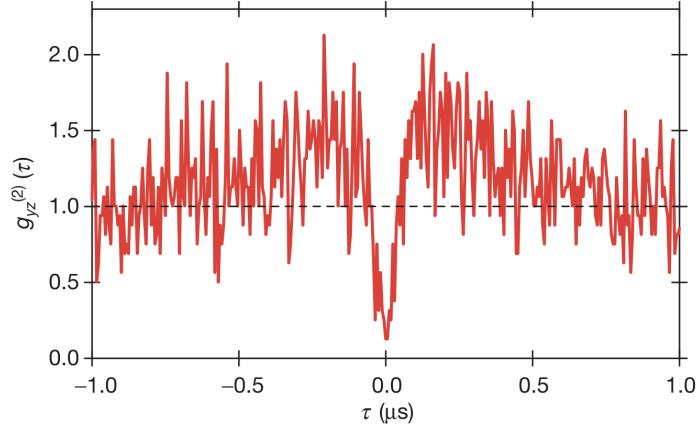


Fig. 2.4. **Experimental realization of photon blockade.** The intensity correlation function $g^{(2)}(\tau)$ as a function of the time delay τ between two photons. $g^{(2)}(\tau)$ drops to near zero at $\tau = 0$, indicating the probability of detecting two photons at the same time is strongly suppressed. The result is reproduced from Ref. [113].

Quantum nonlinear optics with atomic ensembles

Before moving on to quantum many-body physics with light, we would like to mention an alternative approach to engineer strong light-matter interaction where photons are stored in an ensemble of atoms which exhibits the so-called electromagnetically induced transparency (EIT) [114]. In EIT, the optical response of an otherwise opaque atomic gas is modified by an extra control field. This control field is strong and induces coherent coupling between a weak probe pulse and atomic states leading to collective light-matter excitations, called polaritons. The latter results in a drastically reduced group velocity of the probe field, much reduced linear susceptibility $\chi^{(1)}$, and greatly enhanced nonlinear susceptibility $\chi^{(3)}$. Effective strong polariton-polariton interaction is then induced by exciting the atoms to the metastable Rydberg state with a high principal quantum number of approximately 100 [115]. The strong interaction between two Rydberg atoms that are separated by less than the blockade radius introduces an energy shift when two of them are excited. This energy shift is maximized when both controlled field and probe field are resonant with corresponding atomic states. The latter prevents both of them to get excited

simultaneously. Effectively, each Rydberg atom behaves like a ‘superatom’ consisting of N_a atoms within the Rydberg radius but only one excitation, resulting in enhanced cooperativity of $\eta = N_a \lambda^2 / d^2$.

In addition to the above Rydberg blockade, when the control laser is detuned from resonance, it is possible to use EIT to engineer effective distance-dependent interaction between photons. The attractive interaction between photons has been realized in this way and two-photon bound states have been observed [116]. In the case of repulsive interaction, it is predicted that photon crystallization could be formed [7].

2.2.2 Mott-to-superfluid transition of light in coupled resonator arrays

Having realized strong photon-photon interactions, it is natural to ask if photons can form many-body states in analogy to real atoms in solid state. Pioneer works explored this question by envisioning an array of coupled nonlinear cavities both with the Kerr type [60] and the Jaynes-Cummings type [59, 61]. The latter, as shown in Fig. 2.5(a), is described by the Hamiltonian,

$$\hat{H}_{\text{JCH}} = \sum_{j=0}^{L-1} \left(\omega_a \hat{\sigma}_j^+ \hat{\sigma}_j^- + \omega_c \hat{a}_j^\dagger \hat{a}_j + g(\hat{a}_j^\dagger \hat{\sigma}_j^- + \hat{a}_j \hat{\sigma}_j^+) \right) - J \sum_{j=0}^{L-2} \left(\hat{a}_j^\dagger \hat{a}_{j+1} + H.c. \right), \quad (2.16)$$

where L is the size of the system, J is the hopping strength of photons between two adjacent cavities, σ_j^+ (σ_j^-) is the raising (lowering) operator for the atom at site j , and \hat{a}_j (\hat{a}_j^\dagger) is a bosonic annihilation (creation) operator at site j . The model is known as the Jaynes-Cummings-Hubbard (JCH) model. \hat{H}_{JCH} commutes with the total number of excitations $\hat{N} = \sum_j \hat{N}_j$, where $\hat{N}_j = \hat{a}_j^\dagger \hat{a}_j + \hat{\sigma}_j^+ \hat{\sigma}_j^-$. Hence, as shown in Fig. 2.5(b), the eigenspectrum of \hat{H}_{JCH} are grouped into manifold labeled by the filling factor $\bar{n} = \langle \hat{N} \rangle / L$ where $\langle \dots \rangle$ denotes an expectation value over a given eigenstate. It is

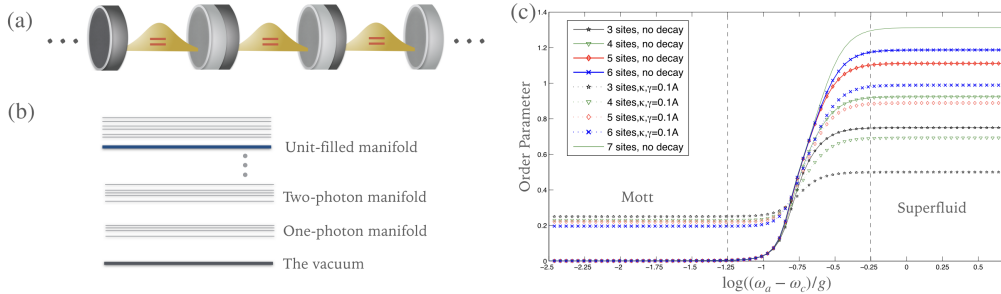


Fig. 2.5. **The Jaynes-Cummings-Hubbard model** (a) A sketch of a coupled cavity array, implementing the Jaynes-Cummings-Hubbard model. (b) Energy spectrum of the JCH model. (c) The order parameter $\text{Var}(N_i)$ of the lowest-energy state in the unit-filled manifold as a function of detuning $(\omega_a - \omega_c)/g$ for 3-7 sites with and without decay. The order parameter exhibits a jump from zero to a finite value, corresponding to the Mott and the superfluid phase, respectively. The transition gets sharper with as the system's size is increased as expected from quantum phase transition. The results are reproduced from Ref. [59].

important to recall that when deriving the Jaynes-Cummings interaction we have assumed that ω_a and ω_c are the largest energy scale in the system. This implies that the ground state of \hat{H}_{JCH} is the vacuum.

To observe many-body characteristics of \hat{H}_{JCH} , one can consider the lowest energy state $|G\rangle_{\bar{n}=1}$ in the unit-filled manifold. At resonance and $g \gg J$, photon blockade prevents two photonic excitations at the same cavity, effectively switching off the hopping process and leading to the Mott-like ground state, i.e., $|G\rangle_{\bar{n}=1} = |1, -\rangle \otimes |1, -\rangle \dots \otimes |1, -\rangle$. This state can be prepared by sending a $\pi/2$ pulse at frequency $\omega_a - g$ to each cavity to excite the vacuum state $|0, g\rangle$ to the lower polariton state $|-\rangle$. To observe the superfluid behavior of photonic excitations, one can adiabatically switch on either the coupling g or the detuning $\omega_a - \omega_c$ via, say, a Stark shift from an external field. In this limit, photon blockade is suppressed and the system is effectively described by the tight-binding model $\hat{H}_{\text{JCH}} \approx -J \sum_j (\hat{a}_j^\dagger \hat{a}_{j+1} + H.c.)$. The Mott-to-superfluid phase transition can then be probed by measuring the fluctuation of the number of excitations, i.e. $\text{Var}(N_i) = \sqrt{\langle \hat{N}_j^2 \rangle - \langle \hat{N}_j \rangle^2}$, see Fig. 2.5(c). Note that, unlike atoms in the Bose-Hubbard lattice discussed in Section 2.1, the number of excitations,

in this case, is conserved. Hence the order parameter $\langle a_i \rangle$ always vanishes both in the Mott and the superfluid phase.

The mean-field phase diagram

To make a more explicit analogy to the atoms in the Bose-Hubbard lattice, one can introduce the chemical potential term to the JCH model [61]. Note that this is done *by hand* since photons do not naturally have a chemical potential. Nevertheless, a possibility to engineer one has been proposed [117]. The JCH model with the chemical potential is written as

$$\hat{H}_{\text{JCH}}^{\text{GC}} = \hat{H}_{\text{JCH}} - \mu \hat{N}, \quad (2.17)$$

where μ is the chemical potential and the label ‘GC’ stands for the grand canonical potential. $\hat{H}_{\text{JCH}}^{\text{GC}}$ still commutes with \hat{N} . However, it is now possible that the ground state of the system is not the vacuum because the chemical potential term introduces an energy shift of $-\mu \bar{n} L$ to the excited states of \hat{H}_{JCH} . This removes the need of restricting ourselves to the $\bar{n} = 1$ manifold as before.

We then proceed to calculate the ground-state phase diagram of $\hat{H}_{\text{JCH}}^{\text{GC}}$ by applying the mean-field approximation $\hat{H}_{\text{JCH}}^{\text{GC}} \approx \sum_j \hat{H}_{\text{JCH}}^{\text{MF}}(j)$, where

$$\begin{aligned} \hat{H}_{\text{JCH}}^{\text{MF}}(j) &= (\omega_c - \mu) \hat{a}_j^\dagger \hat{a}_j + (\omega_a - \mu) \hat{\sigma}^+ \hat{\sigma}^- + g(\hat{a}^\dagger \hat{\sigma}^- + \hat{a} \hat{\sigma}^+) \\ &\quad - 2J(\psi \hat{a}^2 + \psi^* \hat{a} - |\psi|^2) \end{aligned} \quad (2.18)$$

To numerically compute the phase diagram, we first write down $\hat{H}_{\text{JCH}}^{\text{MF}}(j)$ in a matrix form, keeping up to n_{max} excitations. For example, for $n_{\text{max}} = 1$

the matrix takes the form

$$\hat{H}_{\text{JCH}}^{\text{MF}}(j) = \begin{pmatrix} 0 & 0 & -2J\psi \\ 0 & \omega_a - \mu & g \\ -2J\psi^* & g & \omega_c - \mu \end{pmatrix}, \quad (2.19)$$

where $|g, 0\rangle = (1, 0, 0)$, $|e, 0\rangle = (0, 1, 0)$, and $|e, 1\rangle = (0, 0, 1)$. For $n_{\text{max}} = 2$ the matrix takes the form

$$\hat{H}_{\text{JCH}}^{\text{MF}}(j) = \begin{pmatrix} 0 & 0 & -2J\psi & 0 & 0 \\ 0 & \omega_a - \mu & g & -2J\psi & 0 \\ -2J\psi^* & g & \omega_c - \mu & 0 & -2\sqrt{2}J\psi \\ 0 & -2J\psi & 0 & \omega_a + \omega_c - 2\mu & \sqrt{2}g \\ 0 & 0 & -2J\psi & \sqrt{2}g & 2\omega_c - \mu \end{pmatrix}. \quad (2.20)$$

The next step is to numerically obtain the ground state energy as a function of the mean-field energy $E[\psi]$ and find ψ_c that minimizes $E[\psi]$. The process is then repeated until ψ_c is converged with n_{max} . The mean-field phase diagram of $\hat{H}_{\text{JCH}}^{\text{GC}}$ as calculated in Ref. [61] is shown in Fig. 2.6(a). A more accurate phase diagram was calculated numerically using DMRG in Ref [118] and analytically in Ref [119].

Existing works on equilibrium many-body phases of interacting photons

Following the pioneer works, there has been several work investigating various aspects of the JCH model including many-body dynamics [120, 121, 122], ground-state entanglement [123, 124], critical exponents at the phase transition [125] and its applications for quantum information processing [126, 127]. Phase transitions in the JCH model and the BH model have been shown to be in the same universality class. As shown in [59] in the

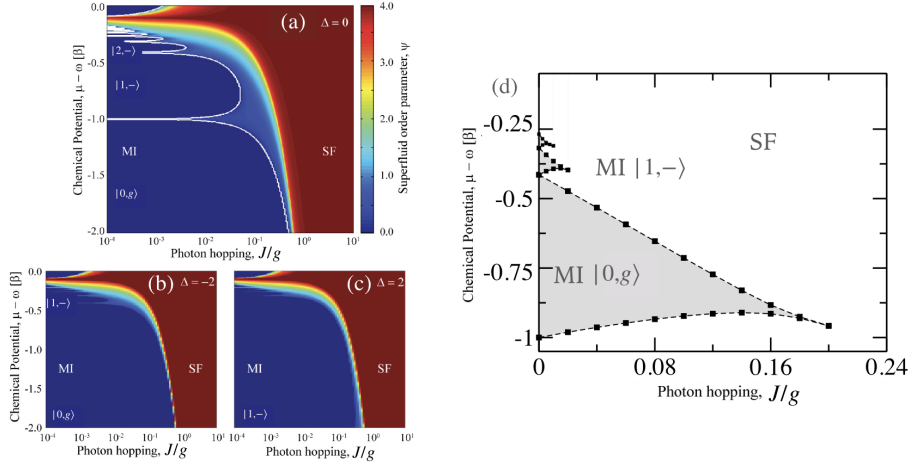


Fig. 2.6. **Phase diagram of the Jaynes-Cummings-Hubbard model.** The mean-field phase diagrams with different detuning $\Delta \equiv \omega_a - \omega_c = 0, -2J, 2J$ are shown in (a)-(c), respectively. The results are reproduced from Ref. [61]. The DRMG phase diagram for the one-dimensional system with $\Delta = 0$ is shown in (d). The result is reproduced from Ref. [118].

Mott regime, the JCH model also simulates the standard XY spin model where the presence and the absence of a polariton in each cavity represent the state of spin up and down, respectively. Subsequent works also show that the anisotropic Heisenberg spin model can be simulated using coupled cavity arrays where each cavity contains a three-level system [65, 66, 67, 68]. Artificial gauge field for photons can be engineered in a 2D array using an external drive that controls the hopping phase of photons. When combined with photon blockade, the ground state of the system can be mapped to the Laughlin state, simulating the fractional quantum Hall state of light [62, 63]. Such combination has been realized with two microwave photons in a three-site superconducting circuit chip [64].

2.2.3 Driven-dissipative many-body phases of interacting photons

Up to now, we have ignored the effect of dissipation by assuming that the dissipation rate is negligibly smaller than a typical energy scale of the system. However, light-matter systems naturally dissipate to the environ-

ment. One of the major developments in the field of many-body physics with light is the study of non-equilibrium many-body phases. The latter happens at the steady state where photon losses are compensated by external laser driving. For example, a coupled resonator array as described by the JCH model can be locally driven by a coherent laser field. The total time-dependent Hamiltonian in the lab frame is written as

$$\hat{H}_{\text{tot}}(t) = \hat{H}_{\text{JCH}} + \sum_{j=0}^{L-1} \Omega_j (\hat{a}_j^\dagger e^{-i\omega_d t} + \hat{a}_j e^{i\omega_d t}), \quad (2.21)$$

where ω_d is the frequency of the drive, Ω_j is the amplitude of the coherent drive. The time dependence can be removed by going the rotating frame defined by $\hat{U}(t) = \exp \left[i(\sum_{j=0}^{L-1} \hat{a}_j^\dagger \hat{a}_j) \omega_d t \right]$, i.e.

$$\begin{aligned} \hat{H}_{\text{tot}}^{\text{R}} &= \hat{U}(t) \hat{H}_{\text{tot}}(t) \hat{U}(t)^{-1} + i\hat{U}(t) \frac{\partial \hat{U}^{-1}(t)}{\partial t} \\ &= \hat{H}_{\text{JCH}} - \omega_d \sum_{j=0}^{L-1} \hat{a}_j^\dagger \hat{a}_j + \sum_{j=0}^{L-1} \Omega_j (\hat{a}_j^\dagger + \hat{a}_j). \end{aligned} \quad (2.22)$$

The effect of dissipation can be captured by considering the Lindblad master equation

$$\frac{\partial \hat{\rho}}{\partial t} = \mathcal{L} \hat{\rho} = -i \left[\hat{H}_{\text{tot}}^{\text{R}}, \hat{\rho} \right] + \frac{\gamma}{2} \sum_{j=0}^{L-1} \left(2\hat{a}_j \hat{\rho} \hat{a}_j^\dagger - \{ \hat{\rho}, \hat{a}_j^\dagger \hat{a}_j \} \right) \quad (2.23)$$

where γ is the loss rate, $\hat{\rho}$ is the density matrix of the system, and \mathcal{L} is the Lindblad super-operator. The master equation is then obtained by first writing down the Schrödinger for the total system and then tracing out the environment, assuming that the system and the environment are initially in a product state and the bath is memoryless [103]. Due to the memoryless bath, the system could reach a non-equilibrium steady state

(NESS) that depends on the symmetries of the system, i.e.,

$$\frac{\partial \hat{\rho}_{\text{NESS}}}{\partial t} = 0. \quad (2.24)$$

Comparison between the NESS of the JCH and the BH model in the driven-dissipative scenario is discussed in Ref. [128]. Similarities between the two models are found when NESS contains a few photons per site, and the light-matter coupling is much stronger than the dissipation rate $g/\gamma \sim 10^4$. In 2009, I. Carusotto's et al. [72] first showed fermionized photons in a driven-dissipative BH array where the NESS of the system mimics a strongly correlated Tonks-Girardeau gas of impenetrable bosons. In an independent work, Hartmann [73] has studied crystallization of photons at the NESS of a similar dissipative BH array but the with alternating local drive $\Omega_j = -\Omega e^{-i\phi_j}$, where Ω is the amplitude of the drive and $\phi_j = j\pi/2$. Similar behavior is observed in the driven-dissipative JCH array [74]. Signatures of fractional quantum Hall in a 2D driven-dissipative BH array is discussed in [75]. Exotic phases at the NESS includes photon solid phases [77] and Majorna-like mode of light [76]. The effect of non-linear driving such as parametric down conversion has been discussed in [76, 129]. Probing many-body signatures of non-linear resonator arrays using photon transport have been discussed in Ref. [130]. A nonlinear superconducting circuit with up to 72 sites has also been fabricated to study the dissipative phase transition [80]. The role of long-range order and the symmetry in driven-dissipative many-body dynamics will be discussed in Chapter 5.

Below we briefly summarize the main results of some of the above proposals and the experiment done in Ref. [80].

Fermionized photons in an array of driven-dissipative nonlinear cavities [72]. Here photons blockade is assumed to be strong such that the probability of having two photons at the same site is strongly suppressed. The latter mimics Pauli's exclusion principle of fermionic particles. In this limit,

commutation relations of bosonic operators can also be mapped to those of fermionic operators using the Jordan-Wigner transformation. In this work, the authors examine such relation for the steady state of driven-dissipative nonlinear cavities as described by Eq.2.24. The drive is assumed to be homogeneous. Fig. 2.7(a) shows the expectation value of the photon number operator $\langle n \rangle$ at NESS for different value of detuning $\Delta\omega_p = \omega_d - \omega_c$. The peaks happen when the frequency of the drive is resonant with the energy of the non-driven system $E(k) = \omega_c - 2J \cos(k)$, where k is the momentum mode. The effect of finite nonlinearities has also been also studied.

Polariton crystallization in driven arrays of lossy nonlinear resonators [73]. Here the author considers arrays of nonlinear resonators as described by the Bose-Hubbard model. The drive has an alternating phase, $\Omega_j = -\Omega e^{-i\phi_j}$. The correlation function between site j and l at NESS is defined as $g_r^{(2)}(j, l) = \langle \hat{a}_j^\dagger \hat{a}_l^\dagger \hat{a}_l \hat{a}_j \rangle / \langle \hat{a}_j^\dagger \hat{a}_j \rangle \langle \hat{a}_l^\dagger \hat{a}_l \rangle$. For strong nonlinearities, $g_r^{(2)}(i, j)$ exhibits density-density correlations indicating crystallization of photons, see Fig. 2.7(b).

Beyond mean-field bistability in driven-dissipative lattices: Bunching-antibunching transition and quantum simulation [131] Here the authors investigated the existence of multiple non-equilibrium states of a driven-dissipative lattice in the limit $U/J \rightarrow \infty$. It was found that a commonly-used mean-field approximation which ignores spatial correlations predicts regimes of bistability at the steady state. However, matrix-product-state based analysis reveals that such bistability is an artifact of the mean-field method. The authors also found a bunching-antibunching transition, Fig. 2.7(c), captured by $C(j, r) = \frac{\langle \hat{n}_j \hat{n}_{j+r} \rangle}{\langle \hat{n}_j \rangle \langle \hat{n}_{j+r} \rangle}$, as the detuning Δ changes.

Photon solid phases in driven arrays of nonlinearly coupled cavities [77] Here the authors considered arrays described by the extended Bose-Hubbard model with cross-Kerr nonlinearities. The mean-field and the matrix-product-state approaches are used to calculate the NESS phase di-

agram that includes a photon crystal phase, see Fig. 2.7(d). The latter is defined by a non-zero population imbalance between two sub-lattices.

Observation of a dissipative phase transition in a one-dimensional circuit QED lattice [80] In this work, 72 coupled microwave cavities each coupled to a superconducting qubit was fabricated to study dissipative phase transition. Microwave transmission $\langle \hat{a}_j \rangle$ is measured at the NESS. Fig. 2.7(e) shows the transmission as a function of power and driving frequency, exhibiting a transition from a suppressed transmission regime to the regime of dynamical bistability.

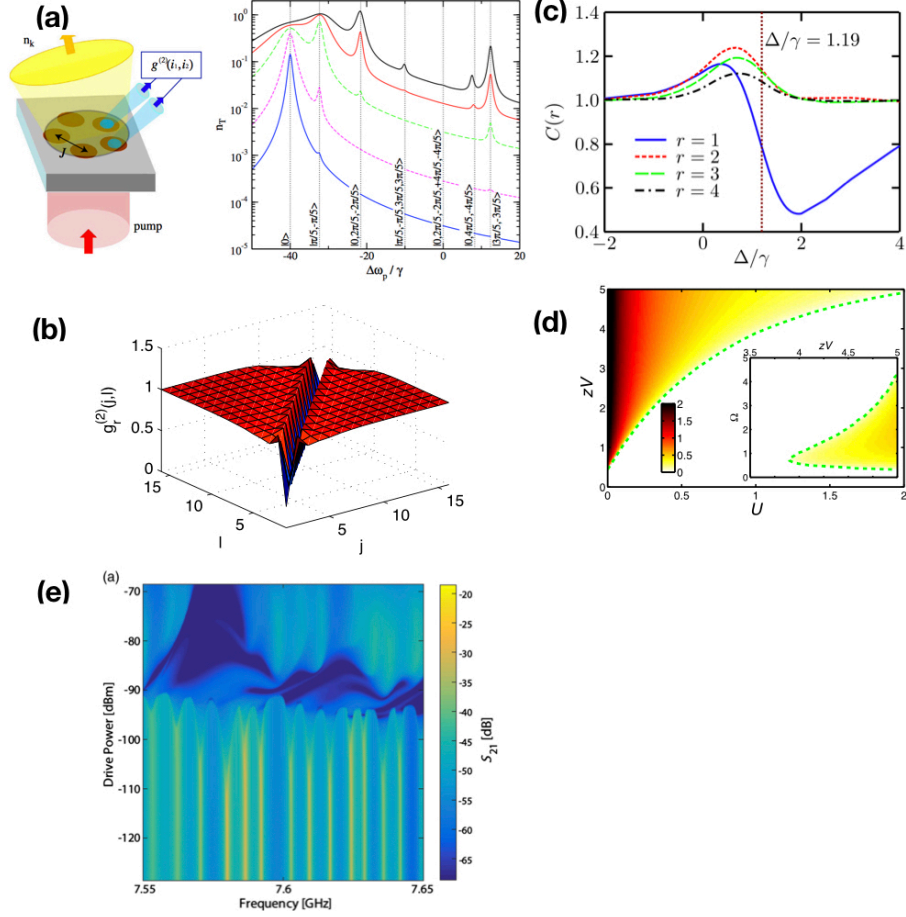


Fig. 2.7. **Driven-dissipative phases and dissipative phase transitions.** (a) fermionized photons at NESS. The plot shows total transmission spectra as a function of the detuning for 5 cavities with $J/\gamma = 20$. Difference curves correspond to the pumping amplitude $\Omega/\gamma = 0.1, 0.3, 1, 2, 3$. (b) Photon crystallization. The figure shows density correlations of the NESS for 16 cavities with $\omega_p = \omega_c$, $U/\gamma = 10$, $\Omega/\gamma = 2$, and $J/\gamma = 2$. (c) Bunching-antibunching transition. Correlations $C(j, r)$ as a function of detuning for $j = 30$, $L = 61$, $J/\gamma = 2, \Omega/\gamma = 1$. (d) Photon solid phases. The plot shows population imbalance at NESS for zero-detuning, $J = 0$, and $\Omega = 0.75$. (e) Observation of dissipative phase transitions. The plot shows the transmission as a function of power and driving frequency, exhibiting a transition from a suppressed transmission regime to the regime of dynamical bistability. The results are reproduced from Ref.[72, 73, 131, 77, 80], respectively.

2.3 Strongly-interacting photons from superconducting circuits

We now turn our discussion to the implementation of cavity QED and light-matter interactions using superconducting circuits. The idea of quantum phenomena in a macroscopic object is traced back to Josephson in 1962 [132] who predicted quantum tunneling of Cooper pairs between two superconductors separated by a thin insulating barrier known as a Josephson junction. In the late 1990s, quantized charges and Rabi oscillation of a capacitively shunted Josephson junction subjected to a weak microwave field were observed [133, 134], providing evidence that a macroscopic object can behave as an effective quantum two-level system. This ‘artificial’ two-level atom, also known as a superconducting qubit, can then be coupled to modes of a harmonic oscillator such as an LC circuit or a coplanar transmission line. The total system mimics the JC model where a single atom coupled to a cavity. This analogy was put forward in 2004 where strong coupling between a single microwave photon and a superconducting qubit was observed [89]. Since the topology of a circuit can be fabricated almost arbitrarily using the conventional electron-beam lithography, superconducting circuits serves as a scalable platform for quantum simulation with interacting photons. Artificial gauge fields for interacting photons in this system have been realized [64]. A nine-site superconducting circuit with a long coherent time has been fabricated to study signatures of a thermalized to a many-body localized transition [70]. A 72-site superconducting circuit simulating the JCH model has been made to study dissipative phase transition of light as discussed earlier [80].

In the following, we will discuss the standard circuit quantization [135] for an LC circuit as a linear element and a particular type of a superconducting qubit called a transmon qubit as a non-linear element. We

conclude the section by reviewing state-of-the-art superconducting chips implementing the BH and the JCH model.

2.3.1 Microwave photons from an LC circuit

An LC circuit is depicted in Fig. 2.8. To write down the Lagrangian for the circuit, we first write down the Kirchhoff's law as

$$\frac{q}{C} = L \frac{dI}{dt}, \quad (2.25)$$

where q is the charge stored in the capacitor, $I = dq/dt$ is the current, C is the capacitance, L is the inductance, $\Phi = LI$ is the flux. By differentiating Eq.2.27 respect to time, we arrive at an equation of motion for a harmonic oscillator

$$\frac{d^2}{dt^2}q + \omega^2 q = 0, \quad (2.26)$$

where $\omega = \frac{1}{\sqrt{LC}}$ is the frequency of the oscillator. The energies stored in the capacitor and the inductor are $E_C = \frac{q^2}{2C} = \frac{1}{2}C\dot{\Phi}^2$ and $E_L = \frac{1}{2}LI^2 = \frac{1}{2L}\Phi^2$ respectively, where $\Phi = LI$ is a flux variable. The Lagrangian of the circuit is then defined as

$$\mathcal{L}_{\text{LC}} \equiv E_C - E_L = \frac{1}{2}C\dot{\Phi}^2 - \frac{1}{2L}\Phi^2. \quad (2.27)$$

This Lagrangian can be compared to that of a particle attached to a spring as shown in Fig. 2.8(b). The flux Φ corresponds to the position of the particle x . The mass of the particle is $m = C$, while the spring constant is $k = 1/L$. Similar to the harmonic oscillator, the Hamiltonian of the LC circuit takes the form

$$H_{\text{LC}} \equiv \mathcal{L}_{\text{LC}} - Q\Phi = \frac{Q^2}{2C} + \frac{\Phi^2}{2L}, \quad (2.28)$$

On-site Hamiltonian	Circuit diagram	Equivalent Cavity QED system	Equivalent Mechanical system
(a) Linear resonator ωn			
(b) AC drive $\Omega(ae^{i\omega_p t} + H.c.)$			
(c) Attractive Kerr resonator (a transmon qubit) $\omega n - \frac{U}{2}n(n-1)$			

Fig. 2.8. **Basic elements in superconducting circuits.** Because an LC circuit is a harmonic oscillator, it can be viewed as a linear cavity operating in the microwave regime or a mass attached to a spring. The circuit can be driven coherently by applying an external voltage in the same way that an external laser can drive a cavity. A capacitively-shunted Josephson junction (c) behaves like a $\chi^{(2)}$ nonlinear cavity which has an analogy to a mechanical pendulum.

where $Q = \frac{\partial \mathcal{L}_{LC}}{\partial \dot{\Phi}} = C\dot{\Phi}$ is a conjugate momentum. By promoting Φ and Q to operators, we get a commutation relation $[\hat{Q}, \hat{\Phi}] = -i$. We define an annihilation operator as

$$\hat{a} = i \frac{1}{\sqrt{2C\omega}} \hat{Q} + \frac{1}{\sqrt{2L\omega}} \hat{\Phi},$$

respectively. The final Hamiltonian then takes the form $\hat{H}_{LC} \approx \hbar\omega(\hat{a}^\dagger \hat{a} + \frac{1}{2})$. We note that we choose to discuss an LC circuit here for simplicity. In the experiment, a loss-noise coplanar transmission is usually used as a linear element [87]. We refer the reader to Ref. [136] for the detailed derivation of the circuit quantization of the latter.

2.3.2 A Kerr resonator from a transmon qubit

Josephson junction provides a natural non-linear element for superconducting circuits. A capacitively shunted Josephson junction is described by the Lagrangian

$$\mathcal{L}_{\text{transmon}} = \frac{1}{2}C\dot{\Phi}^2 + E_J \cos\left(\frac{\Phi}{\Phi_0}\right), \quad (2.29)$$

where E_J is the Josephson energy and $\Phi_0 = \hbar/2e$ is a flux quanta. As shown in Fig. 2.8, a mechanical analogy of this system is a pendulum where C is the moment of inertia, E_J is the gravitational energy, and Φ is the angle of the pendulum. Let us first understand the harmonic oscillation limit of this system. Imagine the pendulum is initially placed at its minima $\Phi = 0$ and then subjected to a small kick that generates an oscillation around this point. If the gravitational energy is large compared to the initial kinetic energy, then this oscillation has a small amplitude. In the circuit picture, this corresponds to the limit $E_J/E_C \gg 1$ where $E_C = e^2/2C$. Subsequently, the expansion of the cosine function in Φ can be truncated at to a finite order, i.e.

$$\mathcal{L}_{\text{transmon}} \approx \frac{1}{2}C\dot{\Phi}^2 - \frac{1}{2L_J}\Phi^2 + \frac{E_J}{4\Phi_0^4}\Phi^4 + \dots, \quad (2.30)$$

where $L_J = \Phi_0^2/E_J$ is an effective linear inductance. When keeping up to the second order, the system reduces to a simple Harmonic oscillator with the frequency $\omega = 1/\sqrt{L_J C}$. Slightly away from this limit, the nonlinearity arises from the fourth order term. Hence, the system becomes a non-linear oscillator. In the following we will perform the circuit quantization while first keeping infinite orders and only apply truncation after normal ordering of ladder operators. Without truncation, the Hamiltonian can be written as

$$\mathcal{H}_{\text{transmon}} = \frac{\mathcal{Q}^2}{2C} + \frac{\Phi^2}{2L_J} + \sum_{m=2}^{\infty} \frac{(-1)^m E_J}{(2m)! \Phi_0^{2m}} \Phi^{2m}, \quad (2.31)$$

where $\mathcal{Q} = C\partial\mathcal{L}_{\text{transmon}}/\partial\dot{\Phi}$ is a conjugate momentum. As before, we promote \mathcal{Q} and Φ to operators as

$$\begin{aligned} \hat{\Phi} &= \sqrt{\frac{L_J\omega}{2}}(\hat{a}^\dagger + \hat{a}), \\ \hat{\mathcal{Q}} &= i\sqrt{\frac{C\omega}{2}}(\hat{a}^\dagger - \hat{a}), \end{aligned} \quad (2.32)$$

where $[\hat{a}, \hat{a}^\dagger] = 1$. We then apply normal ordering of the operators \hat{a} and \hat{a}^\dagger in $\mathcal{H}_{\text{transmon}}$ using the formula [137]

$$(a + a^\dagger)^{2m} = \sum_{k=0}^m \sum_{i=0}^{2m-2k} \frac{(2m)!(a^\dagger)^i a^{2m-2k-i}}{2^k k! i! (2m-2k-i)!}. \quad (2.33)$$

In the limit $E_J/E_C \approx 50 - 100$, the higher order terms in $\mathcal{H}_{\text{transmon}}$ can be truncated up to the fourth order. As a result, the final Hamiltonian can be written as

$$\hat{H}_{\text{transmon}} \approx (\omega + \delta\omega)\hat{n} - \frac{U}{2}\hat{n}(\hat{n} - 1), \quad (2.34)$$

where $U = -E_J e^{-\lambda^2} \lambda^4/4$ is Kerr nonlinearity, $\delta\omega = \lambda^2 E_J e^{-\lambda^2}$, and $\lambda = (2E_{\tilde{C}}/E_J)^{1/4}$. This Hamiltonian takes the same form of that of a Kerr resonator. Due to the n -dependent nonlinearity, a vacuum state $|0\rangle$ and a one-photon Fock state $|1\rangle$ of the resonator can also be used as a qubit. A capacitively shunted Josephson junction operating at this regime is known as a transmon qubit. A typical values of ω and U are $\sim 5 - 10\text{GHz}$ and $\sim 200 - 300\text{GHz}$, respectively [138]. Typical lifetime of photons in the transmon qubit is $10 - 20\mu\text{s}$ with the dephasing time around $2\mu\text{s}$.

Different types of superconducting qubits

For a larger nonlinearity $E_J/E_{\tilde{C}} > 100$, the transmon qubit is also known as a charge or a Cooper-pair-box qubit [133, 134] which was one of the first qubit design invented in early 1990. However, the charge qubit suffers from charge noises and only has a lifetime of a few *ns*. We note that there are several other designs of superconducting qubits such as flux qubits and phase qubits [139, 140, 141, 142, 143, 144, 145] for quantum computing applications [146]. However, only a transmon qubit can be mapped to a Kerr nonlinear resonator and will be the main focus of this Thesis.

2.3.3 Nonlinear lattices from arrays of coupled transmon qubits

The Bose-Hubbard model

Transmon qubits can be coupled in various ways such as a simple use of a capacitor of which we provide details of the circuit quantization in Chapter 4, a transmission line that creates virtual excitation exchange between qubits [147, 148], and a pair of Josephson junctions that allow the coupling to be tuned in situ using an external flux [149, 150, 151]. Arrays of coupled transmon qubits are described by the Bose-Hubbard Hamiltonian

$$\hat{H}_{\text{BHM}} = \sum_{j=0}^{L-1} \omega_j \hat{n}_j - \frac{U}{2} \sum_{j=0}^{L-1} \hat{n}_j (\hat{n}_j - 1) - \sum_{\langle j,j' \rangle} J_{j,j'} \left(\hat{a}_j^\dagger \hat{a}_{j'} + H.c. \right) \quad (2.35)$$

where $\hat{n}_j = \hat{a}_j^\dagger \hat{a}_j$ is a local number operator, $J_{j,j'}$ is the hopping coefficient between the sites j and j' , ω_j is the frequency of the resonator j . State-of-the-art superconducting chips containing arrays of coupled transmon qubits with different topologies are shown in Fig. 2.9. The 9-site one-dimensional chip in Fig. 2.9(a) was used to implement random circuits for quantum supremacy [152] and to observe stroboscopic signatures of many-body localization. The latter will be discussed in Chapter 3. The 5-site chip in Fig. 2.9(b) and 19-site chip in Fig. 2.9(c) were used to demonstrate quantum variational-based algorithms for quantum chemistry [91] and quantum machine learning [92].

The Jaynes-Cummings Hubbard model

A single superconducting qubit coupled to a transmission line can be described with the Jaynes-Cummings model, where the transmission line plays a role of a resonator, and a qubit plays a role of an atom. An array of up to 72 coupled Jaynes-Cummings resonators which leads to the

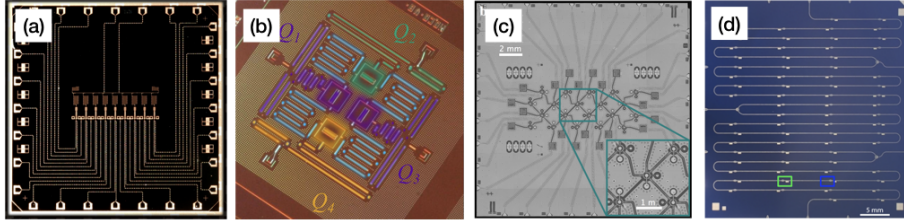


Fig. 2.9. **Arrays of coupled transmon qubits** fabricated by (a) Google with $L = 9$ [152, 70] , (b) IBM with $L = 5$ [91] , (c) Regetti with $L = 19$ [92]. A 72-site superconducting chip implementing the JCH model to study dissipative phase transition [80] is shown in (d).

JCM model has been implemented in Ref. [80] to study dissipative phase transition.

Chapter 3

Spectroscopic signatures of localization with interacting photons in superconducting circuits

Statistical thermodynamics is one of the pillars of modern physics in describing physical systems with a large degree of freedom. Its fundamental postulate states that all accessible microstates associated with a given macro-state have equal probability. In quantum physics, it has been observed that quantum many-body systems would often evolve and reach a thermal equilibrium over time, regardless of a starting state. However, disorders can prevent those systems from thermalization. The mechanism is known as many-body localization (MBL). Unlike quantum phase transitions in the equilibrium case such as the Mott to the superfluid phase transition, the thermalized to the MBL phase transition happens in dynamics and involves all many-body energy eigenstates. The latter poses a fundamental challenge to both theory and experiment.

In this Chapter, we show how signatures of such transition can be ob-

served with interacting photons in superconducting circuits, by directly measuring the spreading of the energy eigenstates and statistics of eigenenergies. Our spectroscopy technique is based time evolution which will be discussed in details in the chapter. We benchmark our method with one photon by resolving the spectrum predicted for two-dimensional electrons in a magnetic field - the Hofstadter butterfly. The experimental results in this Chapter were obtained in collaboration with the quantum hardware team at Google.

3.1 Introduction to Many-body localization

The eigenstate thermalization hypothesis

Ergodicity is a fundamental hypothesis in statistical thermodynamics. It states that, over long periods of time, an ergodic system would explore all accessible states, i.e., all those with the same energy. If a given system satisfies ergodicity, one can describe such system by equilibrium ensembles such as microcanonical, canonical, and grand canonical ensembles. However, it is not uncommon to find systems that are not ergodic. For example, as shown in Fig. 3.1, a ballistic particle moving in a two-dimensional space with an irregular boundary would explore the whole space overtime, while with a circular border the particle will not cross the center of the circle.

Understanding ergodicity and its breakdown in quantum systems have

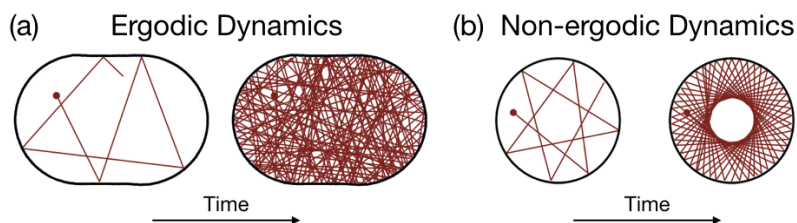


Fig. 3.1. A sketch showing (a) ergodic dynamics of a ballistic particle in an irregular boundary and (b) non-ergodic dynamics in the case of a circular boundary.

been subjected to intense research in the past three decades. Firstly, one has to define what we mean by thermalization of a closed quantum system in the absence of an external reservoir. To do this, imagine a quantum system is initially prepared in a low entropic state. We then divide the system into subsystems A and B . The system is said to be thermalized under its dynamics if at a later time t its subsystem A (or B) is described by a thermal state, i.e.

$$\hat{\rho}_A = \text{Tr}_B(\hat{\rho}_{AB}) = e^{-\hat{H}_A/k_B T}, \quad (3.1)$$

where $\hat{\rho}_{AB}$ is the density matrix of the total system, $\hat{\rho}_A$ is the density matrix of the subsystem A , \hat{H}_A is the Hamiltonian of the subsystem A , T is the temperature, and k_B is the Boltzmann's constant. The eigenstate thermalization hypothesis (ETH) then states that a quantum many-body system always thermalizes after a long enough time, regardless of a starting state. Since energy eigenstates do not evolve, this hypothesis also implies that all many-body energy eigenstates are thermal [30].

Many-body Localization

Many-body localization (MBL) is a generic mechanism that prevents quantum systems from thermalization. MBL systems violate ETH. The effect is based on the celebrated Anderson localization [153] in which non-interacting particles do not spread in a disordered lattice, regardless of its initial state. To discuss the latter effect in details, let's consider a single quantum particle hopping in a tight-binding lattice, i.e.,

$$\hat{H} = -J \sum_{\langle i,j \rangle} (\hat{a}_i^\dagger \hat{a}_j + H.c.) + \sum_i \omega_i \hat{a}_i^\dagger \hat{a}_i. \quad (3.2)$$

In one or two dimensions, the eigenstates are exponentially localized in space for non-zero disorder in ω_i . Hence, an initially localized state will

stay localized after evolving for an infinitely-long time. In three or more dimensions, there is a sharp extended to localized transition as the disorder is increased. The critical disorder strength at which the transition happens can be eigenstate-dependent, leading to the so-called mobility edge.

In the case of interacting particles, there have been extensive numerical evidence suggesting that the Anderson localization effect persists for a strong enough disorder [154, 30, 155, 156, 157, 158, 159, 160, 161, 162, 163, 164]. . In this case, the interacting system does not thermalize even after evolving for an infinitely-long time and does not obey the ETH. This ergodicity breaking phase is referred to as many-body localized (MBL) phases. Note that this thermalized-to-MBL phase transition is a dynamical phase transition, involving all interacting eigenstates. The latter posts a challenge for both theory and experiment since the exact diagonalization is required. Since the dimension of the Hilbert space grows exponentially with the number of particles, numerical studies of MBL have been limited to relatively small systems with around 20 sites in one dimension. Nevertheless, the behavior of the system at the thermodynamic limit can be unambiguously implied from a finite-size scaling [157].

Signatures of MBL have been observed in cold atoms in optical lattices [44, 165, 166], trapped ions [167] and superconducting qubits [168]. In all cases, a non-thermal evolution is probed by monitoring the time dynamics of an initially localized state. In the thermalized phase, the system spreads throughout the lattice over time leading to zero population imbalance between sites. When the disorder is increased, and the system is in the MBL phase, the system shows traces of the initial state after a long period. Although this technique reveals signatures of MBL, directly probing many-body energy eigenstates are still absent in the previous work.

3.2 The superconducting Gmon chip

In this Chapter, we show how energy eigenstates and eigenenergies of quantum many-body systems can be probed by recording the time evolution. Our many-body spectroscopy method is implemented in a nine-site superconducting circuit to resolve energy levels of interacting photons. The circuit consists of nine inductively-coupled transmon qubits. The transmon qubit in this circuit is named a gmon qubit due to the ‘G’ shape design of the coupling circuit. The latter allows the coupling to be tuned in situ using an external flux. As discussed in Chapter 2, an array of coupled transmon qubits can be thought of as coupled nonlinear resonator array with microwave photonic excitation, described by the Hamiltonian

$$\hat{H}_{\text{gmon}} = \sum_{j=0}^8 \omega_j \hat{n}_j - \frac{U}{2} \sum_{j=0}^8 \hat{n}_j (\hat{n}_j - 1) - J \sum_{j=0}^7 \left(\hat{a}_j^\dagger \hat{a}_{j+1} + H.c. \right). \quad (3.3)$$

The frequency of each resonator ω_n can be tuned within $[-4.5, 5.5]$ GHz. The hopping strength J_n can be tuned within $[-5, 50]$ MHz. Both ω_n and J_n can be tuned independently in-situ in a nano-second timescale [150]. The Kerr nonlinearity is fixed at 175 MHz. The lifetime and the dephasing time of each qubit are $20\mu s$ and $2\mu s$, respectively. For the results shown in this chapter, the time evolution was performed within $1\mu s$. Hence the effect of losses can be ignored.

3.3 Many-body spectroscopy from time evolution

In classical physics, fundamental modes of an object can be measured by perturbing the object and recording its subsequent vibrations or its ‘sound.’ Our spectroscopy method for quantum many-body systems is based on this simple principle. Consider the solution of the Schrodinger ’s equation

$$|\psi(t)\rangle = \sum_{\alpha} C_{\alpha} e^{-iE_{\alpha}t} |\phi_{\alpha}\rangle, \quad (3.4)$$

where $|\psi(t)\rangle$ is the state of a quantum system at time t , $|E_{\alpha}\rangle$ is an eigenstate with the eigenenergy E_{α} , and $C_{\alpha} = \langle E_{\alpha}|\psi(0)\rangle$ is an overlap between the initial state $|\psi(0)\rangle$ and $|E_{\alpha}\rangle$. The form of this equation hints that the Fourier transform of the time evolution can reveal the entire spectrum [70, 169, 170]. However, the wave-function cannot be measured directly but via observables. As will be shown below, the choices of initial states and observables play a crucial role in determining the eigenspectrum of quantum systems from the time evolution. To see this, let us write a Hermitian operator \hat{O} in the energy eigenstates,

$$\hat{O} = \sum_{\alpha, \alpha'} O_{\alpha', \alpha} |\phi_{\alpha'}\rangle \langle \phi_{\alpha}|, \quad (3.5)$$

where $O_{\alpha, \alpha'}$ are complex numbers. The expectation values generally contain energy differences

$$O(t) = \langle \psi(t) | \hat{O} | \psi(t) \rangle = \sum_{\alpha, \alpha'} O_{\alpha', \alpha} C_{\alpha} C_{\alpha'}^* e^{-i(E_{\alpha} - E_{\alpha'})t}. \quad (3.6)$$

However, as will be shown below, by choosing the right initial states and observables, one can fix $E_{\alpha'} = 0$ and get absolute energies $\{E_{\alpha}\}$.

Example I: two-site tight-binding model

As an example, let us consider a two-site tight-binding model,

$$\hat{H}_{\text{dimer}} = -J(\hat{a}_0^{\dagger} \hat{a}_1 + H.c.). \quad (3.7)$$

The one-particle energy eigenstates are

$$|E_{\pm}\rangle = \frac{|10\rangle \pm |01\rangle}{\sqrt{2}}, \quad (3.8)$$

where $|10\rangle$ and $|01\rangle$ are single-particle Fock states with one particle on the left and the right side, respectively. The corresponding eigenenergies are $E_{\pm} = \mp J$. As shown in Fig. 3.2, only when the initial state is prepared in the superposition between the vacuum and the one particle state

$$|\psi(0)\rangle = \left(\frac{|0\rangle + |1\rangle}{\sqrt{2}} \right) |0\rangle \quad (3.9)$$

and $\hat{\mathcal{O}} = \hat{a}_1$, the Fourier transform of the observable gives absolute energies E_+ and E_- . Here ‘absolute’ means that we get eigenenergies relative to that of the vacuum. The intuition behind this can be understood by writing the initial state as

$$\begin{aligned} |\psi(0)\rangle &= \frac{|00\rangle + |10\rangle}{\sqrt{2}} \\ &= \frac{1}{\sqrt{2}}|00\rangle + \frac{1}{2}|E_+\rangle + \frac{1}{2}|E_-\rangle \end{aligned} \quad (3.10)$$

The first term $|00\rangle$ is the vacuum which is an eigenstate of the system and does not evolve in time. Hence it serves as a ‘reference’ state. On the other hand, the term $|10\rangle$ is not an energy eigenstate. Hence at a later time it will evolve according to eigenenergies E_{\pm} , i.e.

$$\begin{aligned} |\psi(t)\rangle &= \frac{1}{\sqrt{2}}|00\rangle + \frac{1}{2}e^{-iE_+t}|E_+\rangle + \frac{1}{2}e^{-iE_-t}|E_-\rangle \\ &= \frac{1}{\sqrt{2}}|00\rangle + \frac{1}{2\sqrt{2}}(e^{-E_+t} + e^{-E_-t})|10\rangle + \frac{1}{2\sqrt{2}}(e^{-E_+t} - e^{-E_-t})|01\rangle. \end{aligned} \quad (3.11)$$

When making the measurement, the operator \hat{a}_1 then ‘connects’ the one-photon state $|10\rangle$ with the vacuum, i.e.

$$\begin{aligned} \hat{a}_1|\psi(0)\rangle &= \frac{1}{2\sqrt{2}}(e^{-E_+t} + e^{-E_-t})|00\rangle \\ \langle\psi(0)|\hat{a}_1|\psi(0)\rangle &= \frac{1}{4}(e^{-E_+t} + e^{-E_-t}). \end{aligned} \quad (3.12)$$

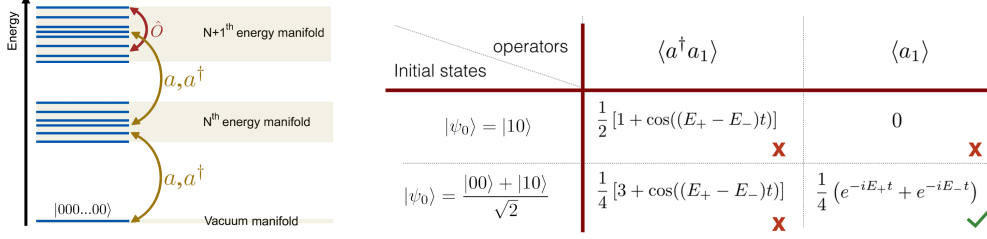


Fig. 3.2. **(a)** The schematic shows that generally, operators, such as \hat{O} connect different levels, and hence in their observables one would see the energy difference between the levels. The raising \hat{a}^\dagger and lowering \hat{a} operators connect states in different manifolds. It is a fortunate coincidence that there is a manifold with only one state in it, the vacuum manifold, which can act as an energy reference. The initial states that are a superposition of the vacuum state and some other states are necessary for having a functional protocol. **(b)** We show expectation values of different operators for two initial states, associated with the example that we used. Note that both proper initial states and choice of operators are needed to have a useful protocol.

Hence the expectation value of \hat{a}_1 oscillates with the frequencies E_+ and E_- . As shown in Fig. 3.2, the number operator \hat{n}_1 connects states within the one-photon manifold. Hence it will contain energy differences $E_+ - E_-$ which is undesirable in our experiments.

Example II: nine-site disordered lattice

Now let us generalize the above example to a nine site disordered lattice as used in the experiment in this Chapter. By placing one photon into the system, it follows that the interaction U is effectively zero. The Hamiltonian of the system is then written as

$$\hat{H}_{\text{gmon}} = \sum_{j=0}^8 \omega_j \hat{n}_j - J \sum_{j=0}^7 \left(\hat{a}_j^\dagger \hat{a}_{j+1} + H.c. \right). \quad (3.13)$$

We begin by initializing a photon at the site p in the superposition state of $|0\rangle$ and $|1\rangle$, i.e.

$$\begin{aligned}
|\psi_0\rangle_p &= |0\rangle_1|0\rangle_2\dots\left(\frac{|0\rangle_p+|1\rangle_p}{\sqrt{2}}\right)\dots|0\rangle_{L-1}|0\rangle_L \\
&= \frac{1}{\sqrt{2}}(|\text{Vac}\rangle+|1_p\rangle), \\
&= \frac{2}{\sqrt{2}}\left(|\text{Vac}\rangle+\sum_{\alpha=0}^8 C_\alpha^p|E_\alpha^{(1)}\rangle\right)
\end{aligned} \tag{3.14}$$

where $|1_p\rangle = \hat{a}_p^\dagger|\text{Vac}\rangle$, $C_\alpha^p = \langle 1_p|E_\alpha^{(1)}\rangle$, and $|E_\alpha^{(1)}\rangle$ is a one-photon energy eigenstate with the eigenenergy $E_\alpha^{(1)}$, see Fig. 3.3(a). The system at time t is given by

$$|\psi(t)\rangle_p = \frac{1}{\sqrt{2}}\left(|\text{Vac}\rangle+\sum_{\alpha} C_\alpha^p e^{-iE_\alpha^{(1)}t}|E_\alpha^{(1)}\rangle\right). \tag{3.15}$$

The operator \hat{a}_p is not Hermitian and therefore not observable. Nevertheless, one can measure

$$\langle\hat{X}_p\rangle \equiv \langle\hat{a}_p^\dagger+\hat{a}_p\rangle, \tag{3.16}$$

$$\langle\hat{Y}_p\rangle \equiv i\langle\hat{a}_p^\dagger-\hat{a}_p\rangle. \tag{3.17}$$

and compute the expectation value

$$\langle\hat{a}_p\rangle \equiv \frac{1}{2}\left(\langle\hat{X}_p\rangle-i\langle\hat{Y}_p\rangle\right) = \frac{1}{2}\sum_{\alpha} |C_\alpha^p|^2 e^{-iE_\alpha^{(1)}t}. \tag{3.18}$$

at different times. Typical values of $\langle\hat{X}_p\rangle$ and $\langle\hat{Y}_p\rangle$ as measured in the experiment as a function of time are shown in Fig. 3.3(b). The Fourier spectrum of $\langle\hat{a}_p\rangle$ for a different p is shown in Fig. 3.3(c). As shown in Eq. 3.18, the position of the peak in the Fourier spectrum corresponds to the eigenenergy $E_\alpha^{(1)}$. By varying all possible initial states with one photon, all eigenenergies are guaranteed to have appreciable amplitudes in the Fourier

spectrum. The Fourier spectrum averaged from all possible initial states is shown in Fig. 3.3(d), confirming that all eigenstates can be measured with this method. In addition, the amplitude of the peak corresponds to the overlap $|C_\alpha^p|^2$ between an initial state $|1_p\rangle$ and the energy eigenstate $|E_\alpha^{(1)}\rangle$. This information also tells us about the spreading of each energy eigenstate in real space spanned by $\{|1_p\rangle\}$.

3.4 Realization of the Hofstadter's butterfly

To benchmark our protocol, we implement the 1D Harper model by setting $\omega_j = \cos(2\pi bj)$, i.e.

$$\hat{H}_{\text{Harper}}^{1\text{-photon}} = \Delta \sum_{j=0}^8 \cos(2\pi bj) \hat{n}_j - J \sum_{j=0}^7 (\hat{a}_j^\dagger \hat{a}_{j+1} + H.c.). \quad (3.19)$$

As before, U is effectively zero because we are dealing with a single particle. The Harper model can be mapped to the 2D Quantum Hall model where b is mapped to a magnetic flux. To see this mapping, let us consider an electron moving in a 2D lattice with a perpendicular magnetic field b as described by the quantum Hall model,

$$\hat{H}_{\text{IQH}} = J_x \sum_{n,m} (\hat{a}_{n,m}^\dagger \hat{a}_{n+1,m} + H.c.) + J_y \sum_{n,m} (\hat{a}_{n,m}^\dagger \hat{a}_{n,m+1} e^{2\pi bni} + H.c.) \quad (3.20)$$

where J_x and J_y are hopping strength along x and y axes respectively, see Fig.3.4. For a periodic boundary condition in the y-direction, one can define the quantum fourier transform $\hat{a}_{n,m}^\dagger = \sum_k e^{-ikm} \hat{a}_{n,k}^\dagger$. Substituting this to Eq.3.20, we get $\hat{H}_{\text{IQH}} = \sum_k \hat{H}_k$, where

$$\hat{H}_k = 2J_y \sum_n \cos(2\pi bn + k) \hat{a}_{n,k}^\dagger \hat{a}_{n,k} + J_x \sum_n (\hat{a}_{n,k}^\dagger \hat{a}_{n+1,k} + H.c.) \quad (3.21)$$

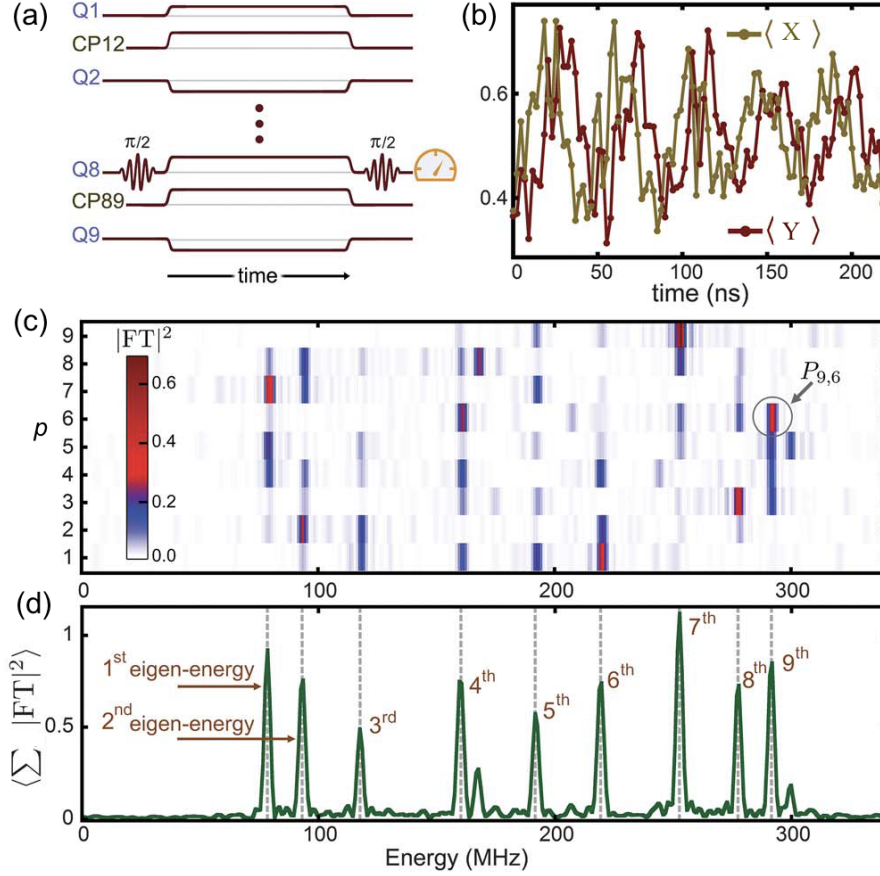


Fig. 3.3. **Time-domain spectroscopy.** (a) Pulse sequence used to measure eigenvalues of a time-independent Hamiltonian. Initially, all the qubits are in the $|0\rangle$ state. Using a microwave pulse, one of the qubits is then placed on the superposition of $|0\rangle$ and $|1\rangle$ state ($Q8$ depicted here). The coefficients in the Hamiltonian are set by applying square pulses on the qubits (Qns) and couplers (CPs). After the evolution, a microwave $\pi/2$ pulse is applied to the qubit in order to measure $\langle\sigma_j^X\rangle$ or $\langle\sigma_j^Y\rangle$. (b) Typical dataset showing $\langle\sigma_j^X\rangle$ and $\langle\sigma_j^Y\rangle$ versus time. (c) The amplitude of the Fourier transform of $\chi_1(n) = \langle\sigma_j^X\rangle + i\langle\sigma_j^Y\rangle$ for $n \in \{1, 2, \dots, 9\}$. The peaks in the FT correspond to the eigenvalues of the Hamiltonian. (d) Summation of the FT amplitudes shown in (c). $P_{9,6}$ is the probability of finding the 9th eigenstate at the site $p = 6$. Adding up all the FT amplitudes is done to show all 9 peaks in one curve.

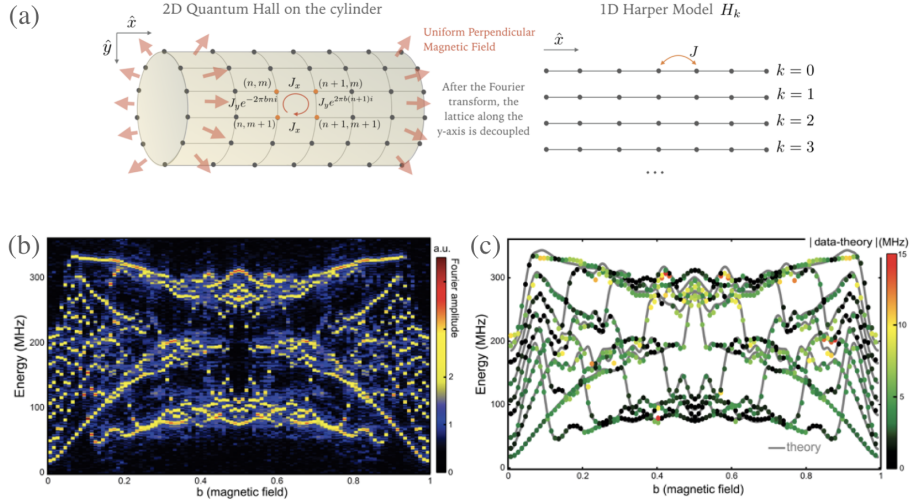


Fig. 3.4. **Hofstadter butterfly.** (a) Illustration of the 2D Quantum Hall model and its mapping to the 1D Harper model. In Eq.3.19, we set on-site potentials $\Delta/2\pi = 50$ MHz and coupling $J/2\pi = 50$ MHz. (b) Data similar to Fig. 3.3(d) is shown for 100 values of dimensionless magnetic field b ranging from 0 to 1. (c) For each b value, we identify 9 peaks and plot their location as a colored dot. The numerically computed eigenvalues of Eq. (2) are shown with gray lines. The color of each dot is the difference between the measured eigenvalue and the numerically computed one.

The 1D harper model is then achieved by dropping the index k in $\hat{a}_{n,k}$ and replacing $2J_y$ and J_x with Δ and J , respectively. Here we also set $k = 0$. Edge states in the Harper model has been studied in [171].

Due to the above mapping, the spectrum of the Harper model as a function of b exhibits a butterfly-like structure similar to its 2D counterpart. The structure was first proposed by Hofstadter in 1976 [172]. It is a fractal structure, meaning that small fragments of the structure contain a copy of the entire structure. However, observing the full butterfly in a conventional condense matter system requires an unphysically large magnetic field in the order of 10^5 Tesla that can ‘squeeze’ one flux quanta through a unit cell. Signatures of the butterfly were observed by using a superlattice structure in graphene [173, 174, 175, 176]. The 2D Hamiltonian H_{IQH} has also been realized in cold atoms [177] and in integrated waveguide arrays.

In this Chapter we realize $\hat{H}_{\text{Harper}}^{1\text{-photon}}$ by setting the qubit’s frequency $\omega_j = \Delta \cos(2\pi b j)$. Since b in $\hat{H}_{\text{Harper}}^{1\text{-photon}}$ is not related to a real magnetic,

it can be easily tuned from 0 to 1 in our setup. We then apply our spectroscopy protocol to probe eigenenergies of $\hat{H}_{\text{Harper}}^{1\text{-photon}}$. In Fig. 3.4(a), we show the plot of the Fourier transform of $\sum_p \langle \hat{a}_p \rangle$ as a function of b . We observe a clear butterfly-like structure as expected since the Fourier transform represents the eigenspectrum. However there are only nine single-particle eigenenergies for each value of b , we cannot conclude the fractal structure of the spectrum. We note that the propose of our experiment here is to benchmark and illustrate the one-photon spectroscopy protocol. In Fig. 3.4(b), we compare the measured peaks in the Fourier transform with exact numerics and found that the errors in the position of the peaks on average are less than 2%. This result illustrates high controllability and a low error rate of our setup.

We note that our protocol does not involve single / two qubit gates as in the digital approach. Hence the gate fidelity is not a requirement here. However, the ability to implement a given Hamiltonian is illustrated by the above Hofstadter butterfly. The resonator frequency ω_j is set by external voltages, which in turn sets the value of b , and can have one or two MHz error.

3.5 Signatures of a localized to a thermalized transition of interacting photons

3.5.1 The Interacting Harper Model

After benchmarking our technique with one photon, we then move to the next simplest interacting case with two photons. By placing two photons

in the system, we then implement the interacting Harper model, i.e.

$$\hat{H}_{\text{Harper}}^{2\text{-photons}} = \Delta \sum_{j=0}^8 \cos(2\pi bj) \hat{n}_j - \frac{U}{2} \sum_{j=0}^8 \hat{n}_j (\hat{n}_j - 1) - J \sum_{j=0}^7 \left(\hat{a}_{j+1}^\dagger \hat{a}_j + \hat{a}_j^\dagger \hat{a}_{j+1} \right), \quad (3.22)$$

The mean-field description of this Hamiltonian to study the spreading of an initially localized wave packet has been investigated in [178, 179, 180, 181]. In contrast to these works, our experiments are deep in the quantum regime with two photons. We randomly chose four different irrational values of b from $[0, 1]$, and the corresponding observables are averaged. The irrational choice of b ensures that the periodicity of the potential and lattice are incommensurate, mimicking the effect of disorder [182, 183]. In our experiment, we fixed $U/J = 3.5$. For this value we expect the ergodic to the localized phase transition of two photons to happen at $\Delta \approx 2J$ [183].

3.5.2 The two-photon protocol

For the two-photon protocol, we begin by placing two photons at the sites p and q with the superposition state $(|0\rangle + |1\rangle)/\sqrt{2}$, i.e.,

$$\begin{aligned} |\psi_0\rangle_{p,q} &= |0\rangle_1 |0\rangle_2 \dots \left(\frac{|0\rangle_p + |1\rangle_p}{\sqrt{2}} \right) \dots \left(\frac{|0\rangle_q + |1\rangle_q}{\sqrt{2}} \right) \dots |0\rangle_{L-1} |0\rangle_L \\ &= \frac{1}{2} (|\text{Vac}\rangle + |1_p, 1_q\rangle) + \frac{1}{2} (|1_p\rangle + |1_q\rangle), \end{aligned} \quad (3.23)$$

where $p \neq q \in \{1, 2, \dots, L\}$ and $|1_p, 1_q\rangle = |0\rangle_1 |0\rangle_2 \dots |1\rangle_p \dots |1\rangle_q \dots |0\rangle_L$ are the two-photon Fock states. The state at time t is

$$|\psi(t)\rangle_{p,q} = \frac{1}{2} \left(|\text{Vac}\rangle + \sum_{\beta} C_{\beta}^{p,q} e^{-iE_{\beta}^{(2)}t} |\phi_{\beta}^{(2)}\rangle \right) + \frac{1}{2} \sum_{\alpha} (C_{\alpha}^p + C_{\alpha}^q) e^{-iE_{\alpha}^{(1)}t} |\phi_{\alpha}^{(1)}\rangle, \quad (3.24)$$

where $\beta \in \{1, 2, \dots, \frac{1}{2}L(L+1)\}$, $|\phi_{\beta}^{(2)}\rangle$ is an energy eigenstate in the two-photon manifold with the corresponding energy $E_{\beta}^{(2)}$ and $C_{\beta}^{p,q} = \langle \phi_{\beta}^{(2)} | 1_p, 1_q \rangle$.

A generalized two-photon lowering operator can be constructed as

$$\hat{a}_p \hat{a}_q \equiv \frac{1}{4} \left(\hat{X}_p \hat{X}_q - \hat{Y}_p \hat{Y}_q - i \hat{X}_p \hat{Y}_q - i \hat{Y}_p \hat{X}_q \right). \quad (3.25)$$

This operator measures the phase difference between the vacuum and the two-photon state, while projecting out the one-photon component to avoid measuring the energy differences $E_\beta^{(2)} - E_\alpha^{(1)}$. Its expectation value takes the form

$$\langle \psi(t) | \hat{a}_p \hat{a}_q | \psi(t) \rangle_{p,q} = \frac{1}{4} \sum_{\beta} |C_\beta^{p,q}|^2 e^{-iE_\beta^{(2)} t}. \quad (3.26)$$

Typical values of $\langle \sigma_p^X \sigma_q^X \rangle$, $\langle \sigma_p^Y \sigma_q^Y \rangle$, $\langle \sigma_p^X \sigma_q^Y \rangle$ and $\langle \sigma_p^Y \sigma_q^X \rangle$ and the Fourier spectrum of $\langle \hat{a}_p \hat{a}_q \rangle$ are shown in Fig. 3.5.

One might observe, that with our choice of initial states one does not directly cover all the space in the two-photon subspace since we did not include double-occupancy states such as $|2_p\rangle \equiv |0\rangle_1 |0\rangle_2 \dots |2\rangle_p \dots |0\rangle_L$. However, in the soft-core limit $U/J = 3.5$ where we operate, all 45 peaks have appreciable amplitudes in the total system's state, which are measured in the experiment, as shown in 3.5(c). This is because the eigenstates $|\phi_\beta^{(2)}\rangle$ have large overlaps with the single occupancy states $|1_p, 1_q\rangle$ as well as the double occupancy states $|2_p\rangle$. As one gets to the hardcore limit with $U/J \rightarrow \infty$, mainly 36 out of 45 eigenenergies will be picked up by $\langle \hat{a}_p \hat{a}_q \rangle$, which again are all the physically relevant ones to probe the physics of the system in this regime.

3.5.3 Level statistics

Definition of level spacing distribution

The origins of level statistics can be traced back to Wigner, who developed random matrix theory to investigate the statistical behavior of many-body systems [184]. Wigner discovered that the repulsion between levels depends

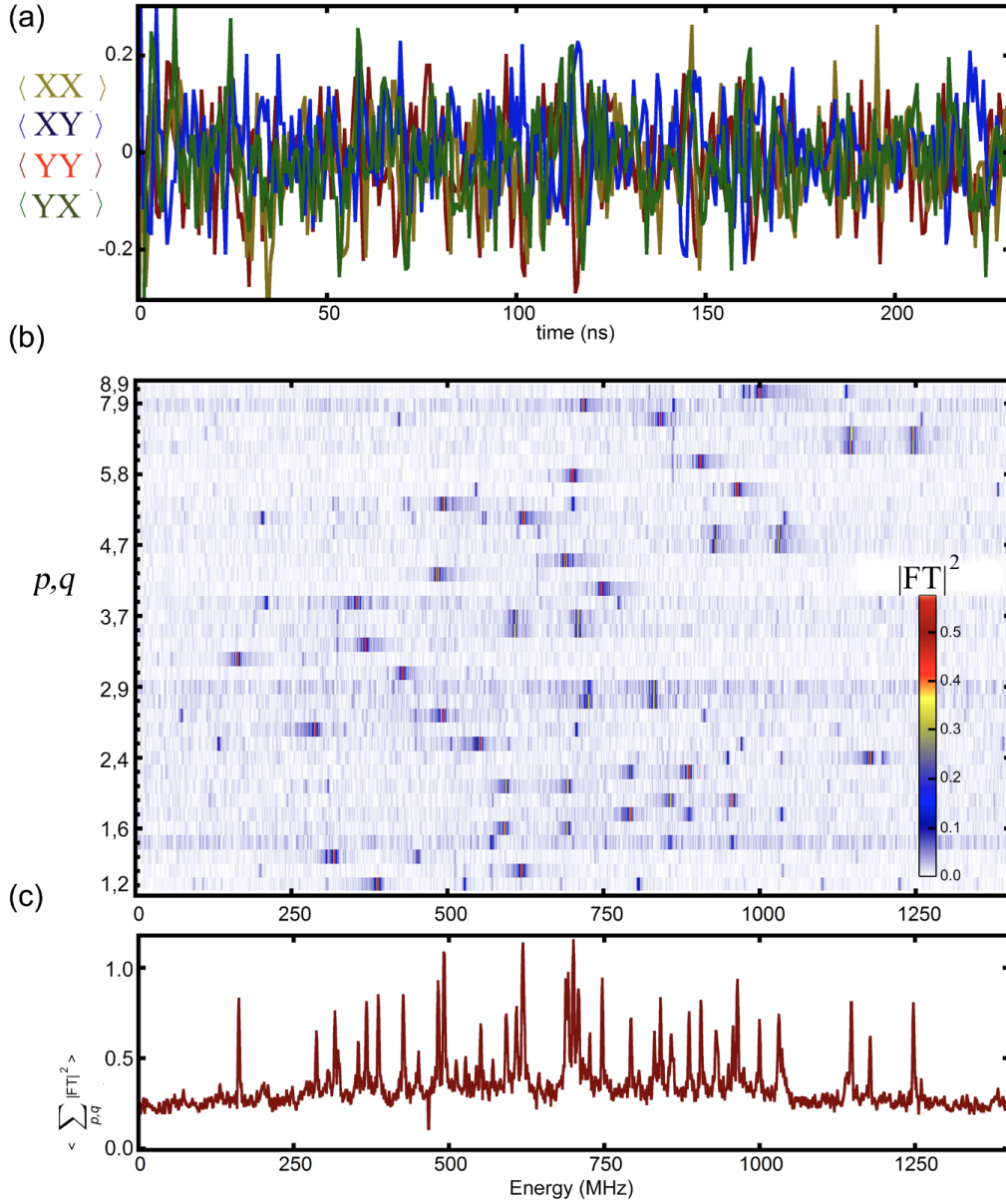


Fig. 3.5. **Spectroscopy of energy levels in the two-photon manifold** (a) A typical time-domain measurement of the two-point correlations that are needed for constructing $\langle \hat{a}_p \hat{a}_q \rangle$. For this data set $p = 5$ and $q = 7$. Similar measurements are done for every $p, q \in \{1, 2, \dots, L\}$ with $n \neq m$. (b) The magnitude of the Fourier transform of $\langle \hat{a}_p \hat{a}_q \rangle$ for all p and q choices with $p, q \in \{1, 2, \dots, L\}$ and $p \neq q$. (c) Average of Fourier transforms presented in (b).

on the symmetries of the underlying Hamiltonian, given that the levels are in the same symmetry class. This tool has proven to be enormously useful in diverse areas such as nuclear physics, disordered systems, and classically chaotic quantum systems [184]. More recently it has been conjectured that there is a relation between many-body localization, thermalization and level statistics [185]. There are three well-known ensembles used in theory for random matrices. The one relevant to our work is the Gaussian orthogonal ensemble (GOE), which applies to systems with time-reversal symmetry. For this kind of systems, the Hamiltonian matrix is symmetric and real and can be diagonalized employing an orthogonal similarity transformation [184].

In level statistics, one is usually interested in the level fluctuations about the smooth part of the integral of the density of states. The procedure to obtain these fluctuations is referred to as the unfolding of levels. However, the success of this approach relies upon our ability to have a good guess for the smooth density of states, which can lead to wrong results in the statistics [186]. Therefore, it is desirable to carry out a statistical analysis of the level spectrum which is independent of the unfolding. This is precisely the motivation to introduce the level spacing distribution $P(r)$ [187].

Since the difference between the ergodic and the localized phase is in its dynamics which are determined by eigenenergies, one of the most direct way to probe the transition is to study the distribution of energy level [188, 189, 190]. Using the two-photon protocol, we measure the two-photon eigenenergies $E_\beta^{(2)}$. Then we calculate the level spacing $s_\beta = E_{\beta+1}^{(2)} - E_\beta^{(2)}$ between two adjacent levels and level separation uniformity, see Fig. 3.6(a),

$$r_\beta \equiv \frac{\min\{s_\beta, s_{\beta-1}\}}{\max\{s_\beta, s_{\beta-1}\}}. \quad (3.27)$$

The level statistics is then defined as a histogram $P(r_\beta)$ of r_β . In the localized phase when the disorder is large, the levels are uncorrelated resulting

in the Poisson distribution

$$P_{\text{Poisson}}(r_\beta) = \frac{2}{(1 + r_\beta)^2}. \quad (3.28)$$

In the ergodic phase, it has been postulated that the statistics of energy levels is the same as the ensemble of real random matrices, following the Gaussian orthogonal ensemble (GOE) [190],

$$P_{\text{GOE}}(r_\beta) = \frac{27}{4} \frac{r_\beta + r_\beta^2}{(1 + r_\beta + r_\beta^2)^{5/2}}. \quad (3.29)$$

Experimental results

Employing our two-photon protocol to resolve the full energy spectrum of $\hat{H}_{\text{Harper}}^{2\text{-photons}}$, we plot the histogram of level spacing $P(r_\beta)$ as a function of disorder strength Δ in Fig. 3.6(b). It can be seen that at $\Delta < 2J$ the peak of the distribution $P(r)$ is located away from $r = 0$. As the disorder is increased beyond $2J$, this peak starts to shift towards $r = 0$, as expected from a finite precursor of the thermalized to the MBL phase transition. Comparisons between our measured $P(r_\beta)$ and the Poisson and the GOE distribution for different values of Δ are shown in Fig. 3.6(c). Unlike the Poisson distribution, at $\Delta > 2J$, we observe that $P(r_\beta)$ tends towards zero as $r_\beta \rightarrow 0$. This behavior is expected from a finite size system, and this effect can also be seen from numerical simulation showed with a blue dashed line in Fig. 3.6(c).

3.5.4 Participation ratio

Definition of the participation ratio

The amplitude of the peaks in the Fourier spectrum in our protocol also provide informations about the probability of each energy eigenstate being present at each lattice site $\{P_{\beta,j}\}$. Perhaps, the most common way to

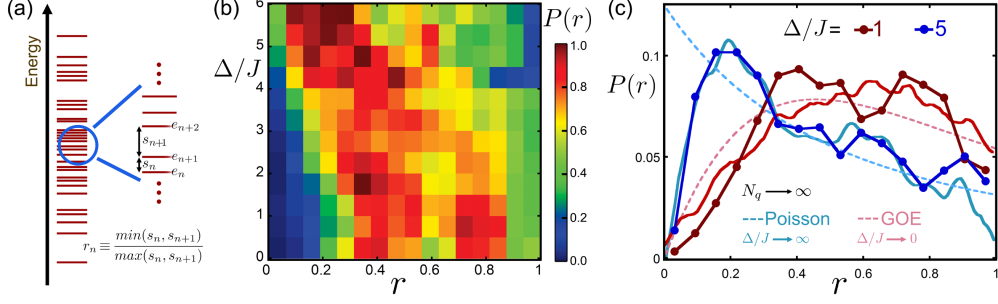


Fig. 3.6. **Level statistics and transition from GOE to Poisson.** (a) The schematic of energy levels shows how r_β is defined. (b) The measured histogram of $P(r)$ measured for various Δ/J values is presented in color. (c) The measured histogram $P(r)$ of r_β s for $\Delta/J = 1$ and 5. The dashed lines are plots of P_{Poisson} and P_{GOE} according to Eq. 3.28 and Eq.3.29, and the solid lines are numerical simulations.

quantify the spreading of the eigenstates is to use the participation ratio (PR) [185]

$$PR_{\text{Space}}(\beta) = \frac{1}{\sum_j |C_j^\beta|^4}, \quad (3.30)$$

and

$$PR_{\text{Energy}}(j) = \frac{1}{\sum_\beta |C_\beta^j|^4}. \quad (3.31)$$

Here $|C_\beta^j|^2$ is the probability of having one or two photons at site j . PR_{Space} indicates the number of states that are present in each site. PR_{Space} indicates the number of lattice sites that are covered by each eigenstate.

The measured PR_{Space} and PR_{Energy} as a function of Δ/J is shown in Fig. 3.7. For low disorder $\Delta/J < 2$, PR_{Space} is close to 45 which is the number of two-photon eigenstates, as expected. This PR_{Space} implies that each eigenstate is fully spread over the lattice. In the same regime of Δ/J , PR_{Energy} is close to 9, indicating that indeed each eigenstate covers the whole lattice. As Δ/J is increased, the eigenstates with the highest and the lowest energies start to shrink, and each eigenstate undergoes a delocalized to a localized transition at different disorder strength. This energy-dependent transition is a finite-size signature of the mobility edge in the thermodynamic limit [191].

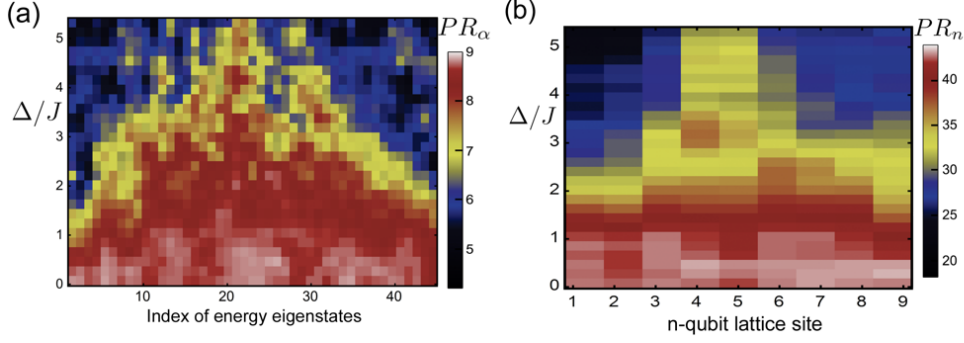


Fig. 3.7. **Mobility edge and localization.** The data is collected using the same parameter settings as used in Fig. 3.6. In Eq. 3.22, we set $b = (\sqrt{5} - 1)/2$ and hopping to $J/2\pi = 50$ MHz which fixes $U/J = 3.5$. We measure the evolution of $\langle \hat{a}_p \hat{a}_q \rangle$ for all $p, q \in \{1, 2, \dots, 9\}$ as a function time for various strengths of disorder Δ . From the magnitude of the peaks seen in the FT of the data the coefficients of expansion of a Fock state (lattice basis) in energy landscape $|C_j^\alpha\rangle$'s and the coefficients for expansion of an energy eigenstate in lattice basis $|C_j^\beta\rangle$'s are extracted. The computed (a) PR_{Space} and (b) PR_{Energy} are plotted. The $E_{\text{max}} - E_{\text{min}}$ is the width of the energy band at a given Δ .

3.6 Effect of missing levels

All of the previous discussion was based on the assumption that one has access to all the energy levels. As the system's size is increased, it will be inevitable that some levels cannot be resolved as the total time evolution fixes the resolution. To estimate the validity of our approach one has to perform statistics $P(r)$ with missing levels. Fig. 3.8(c) and Fig. 3.8(d) depict the level spacing distributions with missing levels for the Hamiltonian in Eq. 3.22 for the resolutions of the Fourier spectrum 0.5MHz and 0.05MHz , respectively with $L = 18$. One can observe that for a resolution 0.5MHz , 10 percent of the levels are missed [see Fig. 3.8(a)] and the histogram does not fit the canonical level spacing distributions $P_{\text{Poisson}}(r)$ and $P_{\text{GOE}}(r)$. In contrast, for a better resolution 0.05MHz , Fig. 3.8 shows a very good agreement of the histogram with the Poisson distribution $P_{\text{Poisson}}(r)$.

As a measure of how close the statistics $P(r)$ are to the canonical probability distributions, i.e., the Gaussian orthogonal ensemble P_{GOE} and the Poisson P_{GOE} distributions, we use the Kullback-Leibler (KL) divergence

from Q to P

$$D_{KL}(P\|Q) = \sum_l P(r_l) \log \left(\frac{P(r_l)}{Q(r_l)} \right) . \quad (3.32)$$

The KL divergence is close to zero when the two distributions P and Q are close. Fig. 3.8(a) and Fig. 3.8(b) show the LK divergence from the canonical distributions $P_{\text{Poisson}}(r)$ and $P_{\text{GOE}}(r)$ to the distribution $P(r)$, which is obtained from the spectrum for different system sizes L . For a low resolution 0.5MHz , Fig. 3.8(a) shows that $D_{KL}(P\|P_{\text{Poisson}}) = D_{KL}(P\|P_{\text{GOE}})$. This occurs for a system size $L = 18$, for which we miss 10 percent of the levels. For $L > 18$, the distribution $P(r)$ gets closer to $P_{\text{GOE}}(r)$. For a better resolution 0.05MHz , Fig. 3.8(b) shows that the distribution $P(r)$ remains close to be Poisson for a wide range of system sizes. When the system size is close to $L = 50$, however, the curves get close together and $P(r)$ is far from the canonical distributions. This intriguing result, i.e., the change in statistics due to missing levels is expected, because one is missing the levels due to a systematic error. In this case, the error arises because of the resolution of the Fourier spectrum. When one has Poisson level statistics, the levels are very close to each other and are uncorrelated. If the resolution is of the order of some level spacings, the two peaks overlap and one would detect one peak instead of two in the Fourier spectrum. This systematic way to drop levels leads to a change from $P_{\text{Poisson}}(r)$ to $P_{\text{GOE}}(r)$ depicted in Fig. 3.8(b) for a low resolution 0.5MHz .

The situation would be different if the levels are dropped randomly. In this case, one can exploit statistical correlations between the levels to compensate for the missing information [192]. For example, if the spectrum is uncorrelated, i.e., described by a Poisson distribution of level spacings, missing data in a random way will not change the statistics. This distribution is the case of a system in the many-body localized phase. On the other hand, when the spectral statistics of the system is given by the Gaussian Orthogonal Ensemble (GOE)—as in the ergodic phase of a many-body sys-

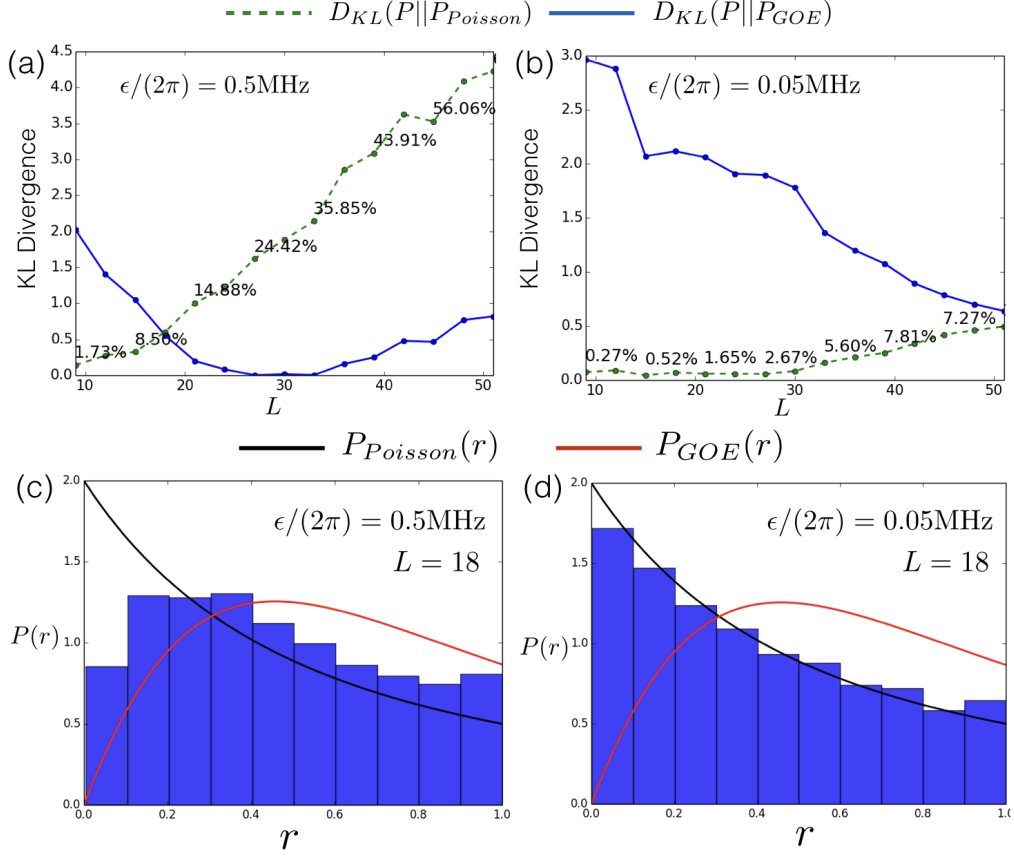


Fig. 3.8. **Level spacing distributions for missing levels.** To determine the efficiency of our method we use the Kullback-Leibler (KL) divergence $D_{KL}(P||Q)$ from Q to P . **(a)** Shows the KL divergence for a resolution 0.5MHz and **(b)** for a resolution 0.05MHz as a function of the system size L . The percentages represent the number of missing levels for a given system size. As one can see from **(a)**, the histogram depicted **(c)** does not fit neither of the canonical distributions P_{GOE} and $P_{Poisson}$ for $L = 18$. At this point, 10 percent of the levels are missing. In contrast, **(d)** shows that for the resolution 0.05MHz the histogram is very close to a Poisson distribution $P_{Poisson}$ for the same system size $L = 18$ as shown in **(b)**. The histograms represent the level spacing distribution obtained from 200 realizations of the Hamiltonian assuming 5 percent of error in b , for $\Delta/2\pi = 200\text{MHz}$, $J/2\pi = 50\text{MHz}$, and $U/2\pi = -175\text{MHz}$.

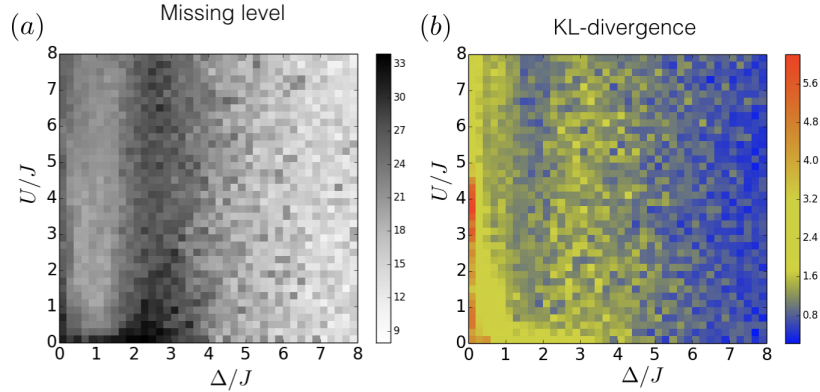


Fig. 3.9. The effect missing levels in level statistics: We numerically simulate a system of two interacting particles in a lattice with $L = 18$ sites and $J = 50\text{MHz}$. **(a)** For a fixed resolution of 1 MHz, we calculate the percent-age of missing levels for dearameter regimes. **(b)** To determine the effect of missing levels on the statistics we use the Kullback-Leibler (KL) divergence between the measured distribution (which had missing levels) to the distribution without missing levels.

tem, the correlations between the levels are strong. As a consequence of this, even if one loses information of some percentage of levels randomly due to the experimental errors, there is a modified GOE statistical distribution that fits the experimental data [192].

In Fig. 3.9(a), we calculate percentage of missing levels for a range of U/J and Δ/J with a fixed resolution of 1 MHz and $L = 18$. It also shows that most of the missing levels (up to 30%) happen around $\Delta \approx 2J$ where the phase transition is expected to happen in the thermodynamic limit. The KL divergence that measures how far the corresponding $P(r)$ is from the perfect case (no missing levels) is shown in Fig. 3.9(b). This result suggests that the current spectroscopy method has to be revised for a large system, such as the one proposed in Ref. [193, 194].

3.7 Conclusions

Using a novel time-evolution based many-body spectroscopy, we have experimentally observed finite-site signatures of the thermalized to the localized phase of two interacting photons in a nine-site lattice via participation

ratio of the eigenstates and level statistics of the eigenenergies. Our results demonstrate high controllability and a long coherent time of small-site superconducting circuits and pave the way for quantum simulation of phases of matter beyond ground states.

Chapter 4

Topological pumping of interacting photons in coupled resonator arrays

In the previous chapter, we have shown how to experimentally extract eigenenergies and eigenstates of time-independent quantum many-body systems and to probe signatures of the thermalized to the MBL transition using superconducting circuits. In this chapter, we theoretically explore how superconducting circuits can be used to study many-body dynamics of periodically and adiabatically driven systems. Specifically, we will be discussing topological pumping of interacting photons in coupled resonator arrays which enables reliable transport of Fock states. The theory proposed here is general and can be implemented in various quantum technologies platform with applications in quantum information processing. We choose to discuss superconducting circuits implementation here in particular as an example since our proposal can be implemented in the superconducting chip used in the previous chapter. We begin the chapter by reviewing the concept of topological pumping in non-interacting systems. We then describe the many-body Hamiltonian used in our proposal and discuss the

intuition behind topological pumping in the interacting case. We then back up the intuition by numerical simulations showing the quantized transport and its robustness against disorders. Lastly, we discuss implementation of our proposal in superconducting circuits and consider the effect of losses. We show that finite-size signatures of our proposal can be observed with realistic parameters that are applicable for the existing superconducting circuit architecture.

4.1 Introduction to topological pumping

In the third century B.C., Archimedes figured out how to pump water up a hill using a rotating screw simply by exploiting the laws of classical physics. Even though the motion of the machine is periodic, the motion of water is unidirectional. This broken discrete time translation symmetry is due to the symmetry of the screw. For example, if the screw were a ladder like, then the water will come back to itself after one driving period. Two millennia later, Thouless translated this idea into a quantum system [195]. He proposed topological pumping for the robust transport of electrons in 1D periodic lattices with a fully-filled band by means of an analogous adiabatic and cyclic deformation of the underlying Hamiltonian. In addition, he showed that the number of particles transported during one pump cycle is quantized and can be related to a topological invariant known as the Chern number [196], as will be discussed in more details below. As a consequence, the transport is robust against small disorder and perturbation [197, 198, 199, 200, 201].

4.1.1 Quantized charge transport

For simplicity, we will discuss the concept of topological pumping via a concrete example of the Su-Schrieffer-Heeger (SSH) model which describes

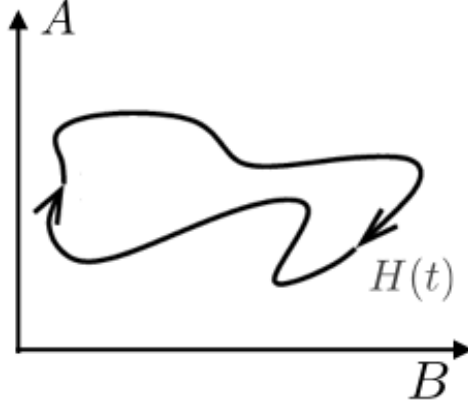


Fig. 4.1. Thouless pumping protocol. The figure shows a path in the space spanned by parameters A and B of a generic Hamiltonian. The transport of quantum particles in a 1D chain arises from a periodically and adiabatically modulated Hamiltonian in analogy to Archimedes's screw. The robust and quantized transport is intimately related to whether or not the path encloses a critical point.

spinless fermions hopping on a dimerized 1D lattice,

$$\hat{H}_{\text{SSH}} = - \sum_{j=0}^{L-2} \left(J_1 \hat{b}_j^\dagger \hat{a}_j + J_2 \hat{a}_{j+1}^\dagger \hat{b}_j + H.c. \right) + \frac{\Delta}{2} \sum_{j=0}^{L-1} \left(\hat{a}_j^\dagger \hat{a}_j - \hat{b}_j^\dagger \hat{b}_j \right), \quad (4.1)$$

where L is the number of unit cells, J_1 is the hopping between sites A and B within the unit cell, J_2 is the hopping between unit cells, $\Delta(t)$ is the onsite energy difference between sites A and B , and \hat{a} (\hat{b}) is an annihilation operator acting at site A (B).

Let $|E_\alpha\rangle$ be single particle eigenstates of \hat{H}_{SSH} with eigenenergies E_α where $\alpha \in \{1, 2, \dots, 2L\}$, i.e.

$$\hat{H}_{\text{SSH}}|E_\alpha\rangle = E_\alpha|E_\alpha\rangle. \quad (4.2)$$

Next we will explicitly express the external degrees of freedom $m \in \{0, 1, \dots, L-1\}$ which is the position of a unit cell and the internal degrees of freedom $m' \in \{A, B\}$. For example we will write a one-particle Fock state of an electron at the site $j = 0, 1, 2$ as $|0\rangle \otimes |A\rangle$, $|0\rangle \otimes |B\rangle$, and $|1\rangle \otimes |A\rangle$, respectively. The Fourier transform of the external degree of freedom is then

defined as

$$|k\rangle \equiv \frac{1}{\sqrt{L}} \sum_{m=1}^L e^{imk} |m\rangle, \quad (4.3)$$

where $k \in \{2\pi/L, 4\pi/L, \dots, 2\pi\}$. Now we can write the eigenstate $|E_\alpha\rangle$ in this new basis as

$$|E_\alpha\rangle \rightarrow |E_k^\nu\rangle = |k\rangle \otimes |u_k^\nu\rangle, \quad (4.4)$$

where the index α is replaced by the momentum k and a band index $\nu \in \{1, 2\}$. The vector

$$|u_k^\nu\rangle \equiv a_k^\nu |A\rangle + b_k^\nu |B\rangle \quad (4.5)$$

with $a_k^\nu, b_k^\nu \in \mathbb{C}$, are eigenstates of the bulk-momentum Hamiltonian defined as

$$\hat{H}_k \equiv \langle k | \hat{H}_{\text{SSH}} | k \rangle$$

i.e. $\hat{H}_k |u_k^\nu\rangle = E_k^\nu |u_k^\nu\rangle$. The current operator is defined as

$$\hat{j}_k = \frac{1}{L} \partial_k \hat{H}_k. \quad (4.6)$$

We then adiabatically modulate the Hamiltonian with the period T i.e. $H_k(t) = H_k(t + T)$ by changing $J_1(t)$, $J_2(t)$, and $\Delta(t)$. The initial state is a fully-filled state. The pumped charge across the lattice after one period in the thermodynamics limit ($L \rightarrow \infty$) is then

$$\mathcal{Q}^\nu = \int_{\text{B.Z.}} \int_{t=0}^{T_d} dt dk \langle \psi^\nu | \hat{j}_k(t) | \psi^\nu \rangle. \quad (4.7)$$

By considering small but non-vanishing contributions from non-adiabatic process, it can be shown that \mathcal{Q} takes the form of the well-known Chern number [195],

$$\mathcal{Q}^\nu = \int_{\text{B.Z.}} \int_{t=0}^{T_d} dt dk (\langle \partial_t u_k^\nu | \partial_k u_k^\nu \rangle - \langle \partial_k u_k^\nu | \partial_t u_k^\nu \rangle). \quad (4.8)$$

The Chern number only takes integer values and only depends on the topology of the path in the parameter space. The topology of the path is determined by whether or not it encloses the critical point. Hence the transported charge in one period is robust against disorder.

Topological pumping has been realized with cold atoms [202, 203]. A related adiabatic pumping machine involving only one eigenstate instead of a fully-filled band has been realized in waveguide arrays [171, 204], quantum wires [205], quantum dots [206, 207, 208], electrons in a mesoscopic conductor [209]. Topological pumping in interacting systems have also been formally explored in [210, 211, 212, 213].

4.2 The model

In this chapter, we propose topological pumping of interacting particles for the reliable transport of bosonic Fock states in 1D lattices. This is quantitatively different from the standard Thouless pumping which does not allow transporting Fock state. Also, we propose to use the quantized transport as a way to probe the topology of quantum many-body systems where the usual Chern number is not well-defined. The mechanism we propose here can be realized in a variety of quantum technology platforms such as ultra-cold quantum gas, trapped ions, and interacting photons in circuit QED.

We consider a nonlinear resonator array of size L described by the Bose-Hubbard model with attractive interactions and spatially modulated on-site energies

$$\hat{H}_{\text{pumping}}(t) = \sum_{j=0}^{L-1} \omega_j(t) \hat{n}_j - \frac{U}{2} \sum_{j=0}^{L-1} \hat{n}_j (\hat{n}_j - 1) - J \sum_{L=0}^{L-2} \left(\hat{a}_j^\dagger \hat{a}_{j+1} + H.c. \right), \quad (4.9)$$

where

$$\omega_j = \omega_0 + \Delta \cos \left[\frac{2\pi j}{3} + \phi(t) \right], \quad (4.10)$$

This model is similar to the one discussed in the previous Chapter except that the cosine potential is now commensurate with the system and its phase $\phi(t) = \omega_d t + \phi_0$ is time-dependent where ω_d is the ramping speed and ϕ_0 is an initial modulation phase. This sweeping is possible in circuit QED, as the frequency of the resonator can be tuned on the fly using a flux bias. Since the wavelength of the cosine modulation is 3, the system can be thought of as an array of trimers of size $L/3$. For convenience, we introduce the index $l \in \{0, 1, \dots, L/3 - 1\}$ to label the trimers. Later in the text, we will refer to the three sub-lattices at positions $3l$, $3l + 1$, and $3l + 2$ within the l th trimer as A , B and C , respectively [see Fig. 4.3(b)].

Our pumping protocol is shown in Fig. 4.3(b). It corresponds to a loop in a 2D parameter space with $U = -J$. Our two varying parameters are the frequency difference $\omega_A - \omega_B$ and $\omega_A - \omega_C$ between two resonators in a trimer, where

$$\omega_A = \omega_0 + \Delta \cos(\phi(t)) \quad (4.11)$$

$$\omega_B = \omega_0 + \Delta \cos\left(\phi(t) + \frac{2\pi}{3}\right) \quad (4.12)$$

$$\omega_C = \omega_0 + \Delta \cos\left(\phi(t) + \frac{4\pi}{3}\right) \quad (4.13)$$

In the Appendix B, we show that for $U = -J$ this loop encloses the critical point when $\omega_A = \omega_B = \omega_C$. We will later show that the spectrum along this loop is gapped. As a result, the topology of the pump is said to be invariant under deformation of this loop as long as it encloses the critical point.

4.3 Topological transport of Fock states

Let us begin by considering three-photon Fock states within a given trimer, i.e. $|300\rangle_l$, $|030\rangle_l$, and $|003\rangle_l$. In the following, we will show that at the right regime, an effective three-photon hopping can be derived, allowing the three-photon Fock states to be efficiently transported through the array.

To illustrate the above, let us decompose the Hamiltonian as $\hat{H}_{\text{pumping}}(t) = \sum_l \hat{H}_0^l(t) + \lambda \hat{V}$, where

$$\hat{H}_0^l(t) = \sum_{j=3l}^{3l+2} \left[\Delta \cos \left[\frac{2\pi j}{3} + \phi(t) \right] \hat{n}_j + \frac{U}{2} \hat{n}_j (\hat{n}_j - 1) \right] \quad (4.14)$$

and

$$\lambda \hat{V} = -J \sum_{j=1}^{L-1} (\hat{a}_j^\dagger \hat{a}_{j+1} + H.c.). \quad (4.15)$$

In the case $J = 0$, we define the on-site energies of the three-photon Fock states as $E_0^\mu(t) = \langle \mu | \hat{H}_0^l | \mu \rangle$ for $\mu \in \{300, 030, 003\}$. Note that the energies $E_0^\mu(t)$ do not depend on the trimer index l . The energies $E_0^\mu(t)$ are simply cosine functions and are depicted in Fig. 4.3(c1) as a function of $\phi(t)$. When including a small but nonvanishing hopping strength $J \ll \Delta$, the crossing in Fig. 4.3(c1) becomes anti-crossing, as shown in Fig. 4.3(c2). This is due to an effective three-photon hopping between two neighbouring sites that happens near an anti-crossing. The mechanism is outlined below. As a result, the energy spectrum when $0 < J \ll \Delta$ is separated into three gapped bands for $\forall \phi(t) \in [0, 2\pi)$, as depicted in Fig. 4.3(c2). The quantized transport of the three photons can then be understood simply by adiabatically following one of these bands [see Fig. 4.3(c2) and (d)].

4.4 Effective three-photon hopping.

To derive the effective three-photon hopping at the crossing points, we will resort to the Schrieffer-Wolff (SW) transformation [214]. As discussed

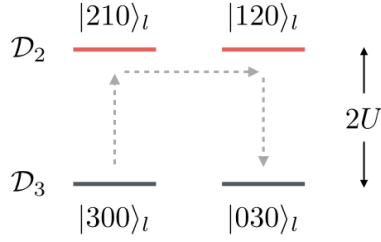


Fig. 4.2. Diagram showing a third-order three-photon hopping process. For the l -th trimer, the states $|300\rangle_l$ and $|030\rangle_l$ have the same on-site energy as well as $|210\rangle_l$ and $|120\rangle_l$. Hence, they can be grouped into two manifolds, labeled as \mathcal{D}_3 and \mathcal{D}_2 respectively. The two manifolds are separated by $\Delta E = 2U$. Since the hopping element between $|210\rangle_l$ and $|300\rangle_l$ is $\sqrt{3}J$, we have $\sqrt{3}J/\Delta E < 1$ for $U = J$. This allows a relatively strong third-order hopping process where the three photons hop from $|300\rangle_l$ to $|030\rangle_l$ via the intermediate states $|210\rangle_l$ and $|120\rangle_l$ and vice versa.

earlier, we restrict ourselves to a three-photon manifold of the l -th trimer, i.e. $|300\rangle_l, |030\rangle_l, |210\rangle_l$ and $|120\rangle_l$. In this subspace, the Hamiltonian is decomposed as $\hat{H}_l = \hat{H}_l^0 + \lambda\hat{V}_l$, where

$$\hat{H}_l^0 = \sum_{j=3l}^{3l-2} [\Delta \cos(2\pi j/3 + \phi(t^*))\hat{n}_j + \hat{n}_j(\hat{n}_j - 1)], \quad (4.16)$$

$$\lambda\hat{V}_l = -J \sum_{j=3l}^{3l-2} (\hat{a}_j^\dagger \hat{a}_{j+1} + \text{H.c.}), \quad (4.17)$$

with $\phi(t^*) = 2\pi/3$. When $J = 0$, the states $|300\rangle_l$ and $|030\rangle_l$ have the same on-site energy ϵ_3 and so do the states $|210\rangle_l$ and $|120\rangle_l$ with the energy ϵ_2 . Hence, the spectrum of \hat{H}_l^0 can be grouped into two manifolds, labelled as $\mathcal{D}_3 = \{|300\rangle_l, |030\rangle_l\}$ and $\mathcal{D}_2 = \{|210\rangle_l, |120\rangle_l\}$ respectively (see Fig.4.2). The two manifolds are separated by a gap $\Delta E = \epsilon_2 - \epsilon_3 = -2U$. We consider the hopping term $\lambda\hat{V}_l$ as a perturbation that couples these manifolds.

Our aim is to find an effective Hamiltonian \hat{H}_l' which has no matrix elements between the two manifolds. We require that the effective Hamiltonian is related to the original Hamiltonian by a unitary transformation $\hat{H}_l' = e^{i\hat{S}^l} \hat{H} e^{-i\hat{S}^l}$, where \hat{S}^l is a Hermitian matrix. By expanding $\hat{S}^l = \lambda\hat{S}_1^l + \lambda^2\hat{S}_2^l + \lambda^3\hat{S}_3^l + \dots$, the effective Hamiltonian can be expressed

up to the third order in λ as $\hat{H}'_l = \hat{H}_l^0 + \hat{H}'_l^{(1)} + \hat{H}'_l^{(2)} + \hat{H}'_l^{(3)}$, where

$$\begin{aligned}
\hat{H}'_l^{(1)} &= [i\lambda\hat{S}_1^l, \hat{H}_l^0] + \lambda\hat{V}_l, \\
\hat{H}'_l^{(2)} &= [i\lambda^2\hat{S}_2^l, \hat{H}_l^0] + [i\lambda\hat{S}_1^l, \lambda\hat{V}_l] + \frac{1}{2}[i\lambda\hat{S}_1^l, [i\lambda\hat{S}_1^l, \hat{H}_l^0]], \\
\hat{H}'_l^{(3)} &= [i\lambda^3\hat{S}_3^l, \hat{H}_l^0] + [i\lambda^2\hat{S}_2^l, \lambda\hat{V}_l] \\
&\quad + \frac{1}{2}[i\lambda^2\hat{S}_2^l, [i\lambda\hat{S}_1^l, \hat{H}_l^0]] + \frac{1}{2}[i\lambda\hat{S}_1^l, [i\lambda\hat{S}_1^l, \lambda\hat{V}_l]] \\
&\quad + \frac{1}{6}[i\lambda\hat{S}_1^l, [i\lambda\hat{S}_1^l, [i\lambda\hat{S}_1^l, \hat{H}_l^0]]]. \tag{4.18}
\end{aligned}$$

Let us consider the first order term $\hat{H}'_l^{(1)}$. Since the matrix element of H'_l between two manifolds is zero, we have $\langle\alpha|\hat{H}'_l^{(1)}|\beta\rangle = 0$, where $|\alpha\rangle$ and $|\beta\rangle$ are states from manifolds \mathcal{D}_α and \mathcal{D}_β with $\alpha \neq \beta$, respectively. For example, one has that $\langle 300|_l\hat{H}'_l^{(1)}|210\rangle_l = 0$. However, the S^l matrix that satisfies this condition is not unique. To avoid this, we choose the \hat{S}^l matrix such that it does not have matrix elements inside each manifold, i.e. $\hat{P}_\alpha S^l \hat{P}_\alpha = 0$, for $\alpha \in \{2, 3\}$ where \hat{P}_α is a projector over the manifold \mathcal{D}_α . Therefore, one has $\hat{P}_2 = |210\rangle_l\langle 210|_l + |120\rangle_l\langle 120|_l$ and $\hat{P}_3 = |300\rangle_l\langle 300|_l + |030\rangle_l\langle 030|_l$.

With this, the first-order matrix \hat{S}_1^l can be written as

$$i\lambda\hat{S}_1^l = \sum_{\alpha,\beta} \frac{\langle\alpha|\lambda\hat{V}_l|\beta\rangle}{\epsilon_\beta - \epsilon_\alpha} |\alpha\rangle\langle\beta| = \frac{\sqrt{3}J}{2U} (|300\rangle_l\langle 210|_l + |030\rangle_l\langle 120|_l - h.c.). \tag{4.19}$$

Similarity, since $\langle\alpha|\hat{H}'_l^{(2)}|\beta\rangle = 0$, the second-order matrix \hat{S}_2^l is

$$\begin{aligned}
i\lambda^2\hat{S}_2^l &= \sum_{\alpha,\beta} \frac{\langle\alpha|[j\lambda\hat{S}_1^l, \lambda\hat{V}_l]|\beta\rangle}{2(\epsilon_\beta - \epsilon_\alpha)} |\alpha\rangle\langle\beta| \\
&= \frac{\sqrt{3}J^2}{4\sqrt{2}U^2} (|300\rangle_l\langle 120|_l + |030\rangle_l\langle 210|_l - h.c.). \tag{4.20}
\end{aligned}$$

The third order commutator $[i\lambda^3\hat{S}_3^l, \hat{H}_l^0]$ is off-diagonal and, by definition, does not contribute to the term $\hat{H}'_l^{(3)}$. By restricting to the \mathcal{D}_3 manifold, i.e. $\hat{P}_3\hat{H}'_l\hat{P}_3$, the three-photon hopping can be derived from the third-order

term as

$$\hat{H}_{l,J}^{(3)} = -\frac{J^3}{\sqrt{2}U^2}(|300\rangle_l\langle 030|_l + |030\rangle_l\langle 300|_l). \quad (4.21)$$

Other terms in $\hat{P}_3\hat{H}'_l\hat{P}_3$ result in a normalization factor of the on-site energies.

We note that the above scheme is somewhat reminiscent of stimulated Raman adiabatic passage (STIRAP) [215], which employs partially overlapping pulses in time to achieve adiabatic transfer between discrete atomic or molecular quantum states. In contrast, our scheme can be used to transport particles that move adiabatically in a continuous energy band between discrete neighboring lattice sites without dispersion. This is only made possible by the topological properties of the Hamiltonian and results in reliable and robust quantum transport of Fock states in the bulk. We stress here that this perturbation does not work in the absence of interactions, i.e., when $U = 0$. Hence, the effective three-photon hopping is only available with interactions.

The three gapped bands in Fig. 4.3(c2), resulting from the effective three-photon hopping, are said to have different topologies due to their distinct transport properties. For example, as shown in Fig. 4.3(d), the states in the middle band move in the opposite direction with twice the speed as those in the upper band. We define the effective Chern number \mathcal{C} as the number of trimers that the three photons pass during one pump cycle, which is equivalent to the Wannier center displacement [196]. Hence, the states in the highest and the middle bands can be assigned with the Chern numbers $\mathcal{C} = +1$ and $\mathcal{C} = -2$, respectively. The sign indicates whether the direction of motion is the same (+) as or opposite (−) to that of the pump. (Recall that the modulation wave $\Delta \cos(2\pi j/3 + \Omega t + \phi_0)$ moves towards the leftmost site $j = 0$).

In Fig. 4.5(a), we numerically show the quantized transport by plotting the density $\langle \hat{n}_j \rangle$ as a function of time. The three-photon Fock state

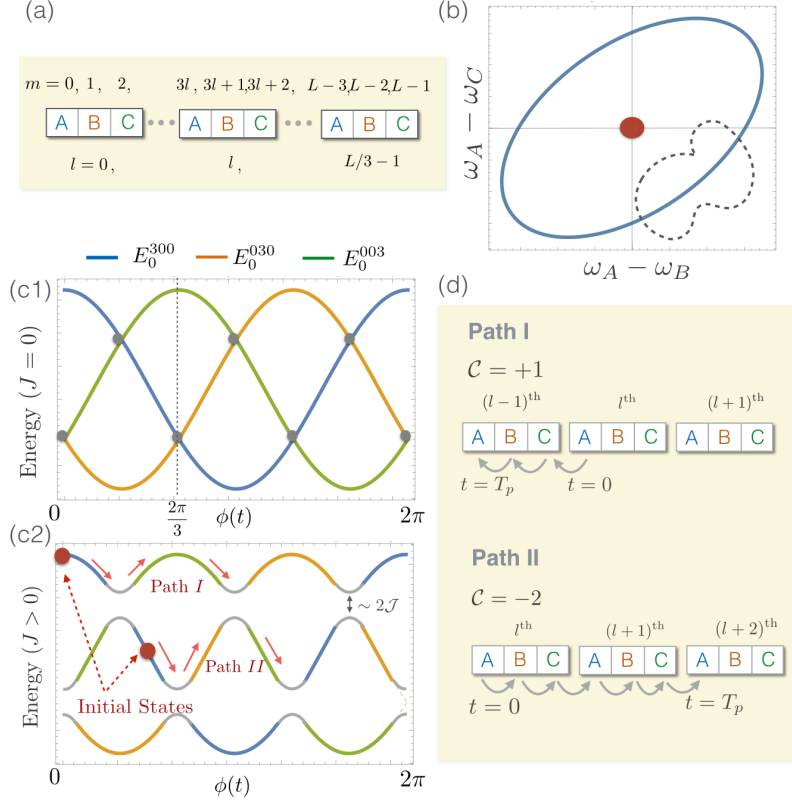


Fig. 4.3. **(a)** Depicts of the sublattices A, B , and C at the sites $3l, 3l+1$ and $3l+2$, respectively. **(b)** Pump cycle in the 2D parameter space spanned by $(\omega_A - \omega_B)$ and $(\omega_A - \omega_C)$ for $U = -J$. It encircles the critical point at $\omega_A = \omega_B = \omega_C$, labelled as a red dot. A gray-dashed path is displayed as an example of a topologically-trivial path. **(c1)** On-site energies, $E_0^\mu(t) = \langle \mu | H_0^l(t) | \mu \rangle_l$, as a function of the modulation phase $\phi(t)$. Different bands $\mu = 300, 030, 003$ are labelled as blue, green and orange, respectively. Crossing points between two bands are labelled as grey dots. **(c2)** Eigenenergies emerging in the presence of a small photon hopping $J \ll \Delta$. As discussed in the text, near every crossing points in **(c1)** an effective three-photon hopping can be derived, which convert these points into the anti-crossing points, shown in **(c2)** with the gap $2\mathcal{J} = \sqrt{2}J^3/U^2$. As a result, the quantized transport of the Fock states can then be understood by adiabatically following one of the bands in **(c2)**. **(d)** Illustration of the quantized transport. $T_p = 2\pi/\Omega$ is the pumping period. In the path I , the state $|300\rangle_l$ is initialized at the highest band with $\phi(0) = 0$. The three photons hop from one site to another when passing through each anti-crossing point. Since in the upper band there are three anti-crossing points for $\forall \phi(t) \in [0, 2\pi)$. After one pump cycle, the three photons are pumped from $|300\rangle_l$ to $|300\rangle_{l-1}$. The transport corresponds to the effective Chern number $\mathcal{C} = 1$. For the path II , the transport has different topology with $\mathcal{C} = -2$. The lowest band has the same topology as the highest one.

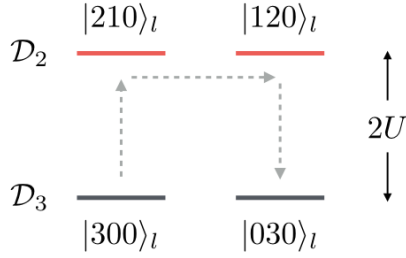


Fig. 4.4. Diagram showing a third-order three-photon hopping process. For the l -th trimer, the states $|300\rangle_l$ and $|030\rangle_l$ have the same on-site energy as well as $|210\rangle_l$ and $|120\rangle_l$. Hence, they can be grouped into two manifolds, labeled as \mathcal{D}_3 and \mathcal{D}_2 respectively. The two manifolds are separated by $\Delta E = 2U$. Since the hopping element between $|210\rangle_l$ and $|300\rangle_l$ is $\sqrt{3}J$, we have $\sqrt{3}J/\Delta E < 1$ for $U = J$. This allows a relatively strong third-order hopping process where the three photons hop from $|300\rangle_l$ to $|030\rangle_l$ via the intermediate states $|210\rangle_l$ and $|120\rangle_l$ and vice versa.

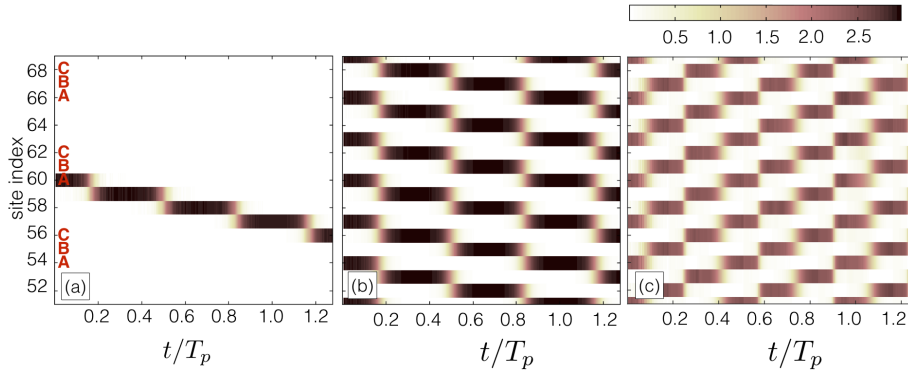


Fig. 4.5. Density plot $\langle \hat{n}_m \rangle$ as a function of time, illustrating a quantized transport of a three-photon state. In **(a)**, a three-photon Fock state $|3\rangle$ is prepared at the sublattice A, located at the middle of an array of size $L = 120$ ($\Delta = 10J$, $\phi_0 = 0$, $U = -J$, $T_p = 2\pi/\Omega$, and $\Omega = 0.01J$). In **(b)**, each sublattice A is filled with the three-photon Fock state. We left five trimers near the edges empty to avoid boundary effects during the evolution. The density plot shows a clear step-like behavior in both cases. In **(c)**, the initial modulation phase is set at $\phi_0 = \pi/2$ and the ramping speed is $\Omega_p = 0.002J$. As discussed in the text, this results in a quantized transport in the reversed direction and twice the speed of the pump. In **(b)** and **(c)**, the local Hilbert space in the numerics is truncated at the five photon Fock state .

is initialized at the site $j = 60$ (sublattice A) of an array of size $L = 120$. Time evolution is performed using Time-Evolving Block Decimation (TEBD) [216, 217] with parameters given in Appendix C. The parameters of the Hamiltonian are $\Delta = 10J$, $U = -J$, $\Omega = 0.01J$ and $\phi_0 = 0$. The density plot shows a clear step-like motion with $\mathcal{C} = 1$, as expected.

One can also imagine filling each trimer l with the same three-photon Fock states $|300\rangle_l$, i.e. the unit-filling condition [see Fig. 4.5(b)]. Because photons between neighboring trimers are always two-sites apart, they are effectively decoupled from each other throughout the evolution. Hence, a similar quantized transport occurs for many-photon states.

The quantized transport with $\mathcal{C} = -2$ is shown in Fig. 4.5(c), where the initial modulation phase is changed to $\phi_0 = \pi/2$ while keeping the initial state the same as that in Fig. 4.5(b). The motion is reversed with twice the speed compared to the one in Fig. 4.5(b), as expected. To further emphasize the topological nature of the transport, in Fig. 4.6(a1) we also change our pumping scheme to the one that does not enclose the critical point in the 2D parameter space, while keeping the starting and the end points the same as before. As shown in Fig. 4.6(a2), photons following this path remain localized throughout the evolution, corresponding to a topologically-trivial transport with $\mathcal{C} = 0$, as expected.

4.5 Robustness of the transport

The quantized transport discussed here so far is protected by the energy gap proportional to $2\mathcal{J}$. Hence, it is robust against small perturbations. To illustrate this, we add random noise to the system as

$$\hat{H}_\eta = \eta \sum_{j=0}^{L-1} r_j(t) \hat{n}_j \quad (4.22)$$

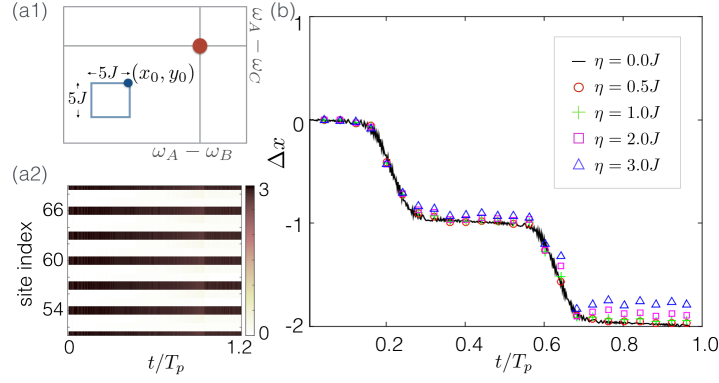


Fig. 4.6. **(a1)** Illustration of a topologically-trivial pumping scheme in the 2D parameter space. We fix $\omega_A = \omega_0$ and vary ω_B and ω_C as a square loop with the starting point $(x_0, y_0) = (-\Delta \cos(2\pi/3), -\Delta \cos(4\pi/3))$. The pumping period T_p and the initial state are the same as in Fig. 4.5(b). **(a2)** Density plot showing the corresponding motion. **(b)** Center-of-mass (COM) displacement, Δx , of a three-photon state as a function of time with the non-trivial pumping topology in the presence of random noise. A black solid line corresponds to the perfect case with no noise $\eta = 0$. The parameters of the Hamiltonian and the initial state are the same as those in Fig. 4.5(a). The plot shows that the quantized motion is robust against weak perturbations, such that the amplitude of the noise, η , is smaller than the smallest energy gap $2\mathcal{J}$.

where η is the noise amplitude and $r_j(t) \in [0, 1]$ is a random number, drawn differently for each site at each time step. The parameters of the Hamiltonian and the initial state are the same as in Fig. 4.5(a). The center-of-mass (COM) of the three photons as a function of time, with an increasing η , is shown in Fig. 4.6. It can be seen that the quantized motion is robust against weak perturbations, $\eta \lesssim J$. As the noise amplitude η becomes comparable to the smallest energy gap, which in this case is $2\mathcal{J} \sim 1.4J$, the COM is biased towards the rightmost site ($j = L - 1$). This is expected, as random noise introduces coupling to states from other bands. As shown before, these states are transported in the opposite directions. Therefore when $\eta \gtrsim \mathcal{J}$, the COM deviates from the ideal case over time.

4.6 Circuit QED implementation

In the last section of this Chapter, we will discuss how an array of capacitively-coupled transmon qubits can be mapped to a nonlinear coupled resonator array, as described by the Bose-Hubbard Hamiltonian. The derivation provided here can be generalized to a more complex coupler such as a transmission line [218, 219, 220] and an inductive tunable coupler [149]. Similar approaches have been followed recently in the field of quantum metamaterials where superconducting meta atoms are coupled to photons [221, 222, 223, 224].

Our circuit diagram is shown in Fig.4.7. The flux variable is defined as $\phi_j = -\int V_j dt$, where V_j is a voltage at the corresponding position. As will be shown below, this quantity can be quantized to the form $\phi_j = \alpha(\hat{a}_j + \hat{a}_j^\dagger)$, where $\hat{a}_j, \hat{a}_j^\dagger$ are bosonic operators at site j and α is some constant that depends on the circuit's elements. As shown in [225], two parallel-connected Josephson junction with a flux bias Φ_g can be thought of as an effective single Josephson junctions E_J where

$$E_J = (E_{J1} + E_{J2}) \cos\left(\frac{\Phi_g}{2\Phi_0}\right) \sqrt{1 + d^2 \tan^2\left(\frac{\Phi_g}{2\Phi_0}\right)}, \quad (4.23)$$

with $\Phi_0 = \hbar/2e$ and $d = (E_{J2} - E_{J1}) / (E_{J2} + E_{J1})$. The resonator's frequency ω_j is related to E_J , hence it can be tuned on the fly, by changing the flux bias Φ_g .

Following the standard circuit quantization procedure [135], we first write down the circuit's Lagrangian as

$$\mathcal{L} = \sum_{j=0}^{L-1} \left(\frac{1}{2} C_J \dot{\phi}_j^2 + E_J \cos\left(\frac{\phi_j}{\Phi_0}\right) \right) + \sum_{j=0}^{L-2} \frac{1}{2} C (\dot{\phi}_j - \dot{\phi}_{j+1})^2, \quad (4.24)$$

Assuming $C/(C_J + 2C) \ll 1$, the Hamiltonian can be obtained using the

Legendre transformation [226],

$$H = \sum_{j=0}^{L-1} \left(\frac{\dot{\phi}_j^2}{2\tilde{C}} + \frac{\phi_j^2}{2\tilde{L}} + \sum_{n=2}^{\infty} \frac{(-1)^n E_J}{(2n)! \Phi_0^{2n}} \phi_j^{2n} \right) + \sum_{j=0}^{L-2} \frac{C}{\tilde{C}^2} q_j q_{j+1}, \quad (4.25)$$

where

$$q_j = \sqrt{2C + C_J} \frac{\partial \mathcal{L}}{\partial \dot{\phi}_j} \quad (4.26)$$

is a conjugate momentum of ϕ_j , $\tilde{C} = C_J + 2C$ is an effective capacitance and $\tilde{L} = \Phi_0^2/E_J$ is an effective inductance. We then quantized ϕ_j and q_j by defining ladder operators $\hat{a}_j, \hat{a}_j^\dagger$ according to

$$\hat{\phi}_j = (\tilde{L}/4\tilde{C})^{1/4} (\hat{a}_j + \hat{a}_j^\dagger) \quad (4.27)$$

$$\hat{q}_j = i(\tilde{C}/4\tilde{L})^{1/4} (-\hat{a}_j + \hat{a}_j^\dagger) \quad (4.28)$$

The first two terms in Eq.4.25 become $\sum_j \omega \hat{a}_j^\dagger \hat{a}_j$, where $\omega = 1/\sqrt{\tilde{L}\tilde{C}}$ is a resonator frequency. In addition, the capacitor C leads to the hopping term with $J = -\frac{\omega C}{2\tilde{C}}$. A rotating-wave approximation is assumed, so we ignore the term $(\hat{a}_j^\dagger \hat{a}_{j+1}^\dagger + h.c.)$.

The Josephson junction E_J introduces an anharmonicity to the resonator's frequency. Due to this anharmonicity, a vacuum state $|0\rangle$ and a one-photon Fock state $|1\rangle$ of the resonator can be used as a qubit. A transmon qubit corresponds to the regime with a large $E_{\tilde{L}}/E_{\tilde{C}} > 1$ where $E_{\tilde{C}} = e^2/2\tilde{C}$ and $E_{\tilde{L}} = \Phi_0^2/\tilde{L}$, such that the terms higher than the forth order can be neglected [225]. Hence, a transmon qubit can be thought of as a resonator with an attractive Kerr nonlinearity $U < 0$. Taking into account the normal ordering [218], we get $U = -E_J e^{-\lambda^2} \lambda^4/4$, where $\lambda = (2E_{\tilde{C}}/E_{\tilde{L}})^{1/4}$. This normal ordering also introduces a small normalization factor $\delta\omega$ to the resonator frequency, with $\delta\omega = \lambda^2 E_J e^{-\lambda^2}$.

Note that all Hamiltonian parameters (ω_j, J and U) depend on E_J . Hence, in general, tuning ω also effects other parameters as well. For

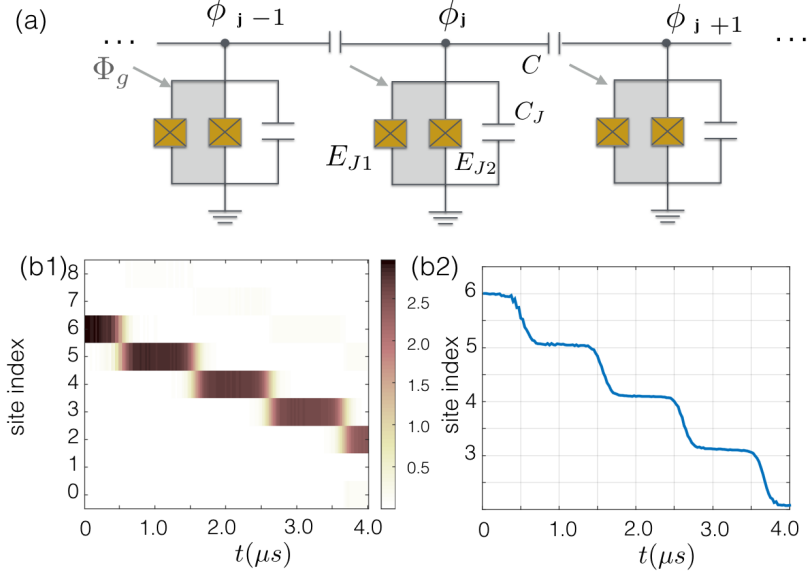


Fig. 4.7. **(a)** Circuit QED diagram showing an implementation of the Hamiltonian $H(t)$. We introduce the flux variable which is defined as $\phi_j = -\int V_j dt$, where V_j is a voltage at the corresponding position. As shown in the Supplemental Material, this quantity can be quantized to the form $\phi_j = \alpha(a_j + a_j^\dagger)$, where α is a constant depending on the circuit's elements. The Josephson junctions E_{J1} , E_{J2} and the shunting capacitor C_J acts as a nonlinear resonator, whose frequency can be tuned via the flux bias Φ_g . Each resonator is coupled by the capacitor C . **(b1)**-**(b2)** Quantum trajectory simulations of nine-site lossy resonator array. **(b1)** Density plot $\langle \hat{n}_j \rangle$ as a function of time in a lossy case. **(b2)** Center-of-mass of the three photons as a function of time. A clear step-like behavior is observed in both plots.

the proposal discussed in this Chapter, we tune the resonator frequency within the range $[\omega_0 - \Delta, \omega_0 + \Delta]$, where $\omega_0 \sim 5$ GHz, $\Delta = 400$ MHz and $J = -U = 40$ MHz. Hence ω_j only changes by $\sim 8\%$. Therefore, subsequent changes in J and U are small compared to Δ and do not alter our discussion in the Chapter 4. We also note that using a magnetic flux to drive the Hamiltonian in the MHz timescale has been experimentally realized [64].

Effect of photon loss

The localization due to attractive interaction and large modulation $\Delta \gg J$ in our system allow signatures of topological pumping to be visible with an existing finite-size array, as small as $L = 9$. In this section, we investigate

our pumping protocol with realistic parameters which are realizable in the superconducting circuit as used in the previous Chapter. We numerically solve the Lindblad master equation involving realistic photon loss, which is expressed as

$$\frac{\partial \hat{\rho}}{\partial t} = -i[\hat{H}(t), \hat{\rho}] + \frac{1}{2T_1} \sum_{j=0}^{L-1} \left(2\hat{a}_j \rho \hat{a}_j^\dagger - \{\hat{n}_j, \rho\} \right), \quad (4.29)$$

where ρ is a density matrix and $T_1 = 20 \mu s$ is a photon lifetime. We choose realistic parameters of the Hamiltonian as $\Delta = 0.4$ GHz, $\Omega = 2$ MHz, $J = 40$ MHz and $U = -40$ MHz. 5% disorder is added to U to mimic the fact that nonlinearities of Josephson junctions are different. Three photons are initialized at the site $m = 6$ with $\phi_0 = 0$. Time evolution is performed using the quantum trajectories [227]. The density and the COM plots as a function of time are shown in Fig. 4.7(b1) and Fig. 4.7(b), respectively. A clear step-like motion is observed in both plots.

Our implementation of the above methods is based on the open-source Tensor Network Theory (TNT) library [261]. We found that the results shown in the manuscript can be sufficiently simulated with $\chi = 100$ and $N_{\max} = 4$. Time evolution is discretized in the timestep of $\delta t = 0.02/J$ and for the dissipative dynamics, time evolution of the density matrix is calculated by averaging over $M = 1000$ trajectories. We observed that increasing χ , N_{\max} , M and reducing δt further do not lead to any significant changes in our results.

4.7 Discussion

In conclusion, we have proposed a new mechanism of topological transport of interacting particles. The interactions enable robust transport of few-photon Fock states against disorder. We also discuss in details how to implement the above in existing circuit QED architectures.

We note that our scheme here can be trivially generalized to Fock states other than three. For example, by initializing two photons per trimer and choosing appropriate U/J , Fock states with a $2/3$ filling can be transported. Also, although we have been focusing on the transport of Fock states, entangled states are also created during the hopping process and can be transported by adjusting the initial conditions. Hence, in the future, it would be interesting to characterize this entanglement, which emerges between the two neighboring sites during population transfer, and seeks applications in quantum information processing.

Chapter 5

Hidden order in driven-dissipative dynamics of interacting photons in coupled resonator arrays

In Chapter 3 and 4, we have explored quantum many-body dynamics of closed quantum systems with superconducting circuits both in a driven and undriven case. In this chapter, we explore exotic driven-dissipative dynamics of quantum many-body systems. Interacting photons provide a natural setting for simulating these open quantum systems because photons dissipate to the environment and because they can be coherently driven.

The coupling between photons and the environment is usually assumed to be weak and the bath is memoryless in which case the system could reach a dynamically-stable steady state that depends on the symmetries of the system [71, 128]. Early theoretical works have shown that such steady states manifest various quantum many-body phases [72, 73, 228, 75, 74, 76, 77, 129, 229, 131] and can exhibit a dissipative phase transition (DPT) [230, 78]. A nonlinear superconducting circuit with up to 72 sites has also

been fabricated to study DPT [80].

Following the success of Landau's symmetry breaking theory in describing classical and ground-state phases of matter, local order parameters have also been used to classify these new non-equilibrium steady-state phases [230, 78, 72, 73, 228, 75, 74, 76, 77, 129, 229, 80]. However, in equilibrium systems, there are phases that do not follow Landau's symmetry breaking theory [231]. The latter can be probed by, for example, non-local order parameters [232, 233] or the existence of edge states [234, 235]. These phases are symmetry protected topological (SPT) phases [236, 237] and phases with topological orders [238, 239]. Experimental realizations of topological phases have been explored in various quantum technology platforms including cold atoms [240] and photonic systems [241, 242].

In this chapter, we study the role of a non-local order parameter in the driven-dissipative dynamics of a quantum many-body system and its connection to the underlying symmetry. Specifically, we consider a non-local hidden order, analogous to the famous SPT phase characterizing the equilibrium Haldane insulator (HI) phase [243, 244, 245]. The system we consider is a lossy nonlinear photonic lattice of the extended Bose-Hubbard type [243, 244, 245] which in the right regime can be mapped to the spin-1 Haldane model [246, 247] and driven by a two-photon parametric process [76, 129, 248]. Using matrix-product-state based calculations [216, 217], we show that this process drives the vacuum into a quantum many-body state with non-zero hidden order. However, the hidden order only remains non-zero for a finite time and eventually fades away at the steady state. We argue that this effect is due to the symmetry of the parametric drive, which cannot be achieved by a conventional one-photon coherent drive. We analyze this symmetry analytically and numerically by showing that the parametric drive respects the symmetry of the HI state. The natural photon loss breaks the symmetry and therefore plays a negative role in

maintaining the hidden order in the dynamics.

This chapter is organized as follows. We first review the concept of hidden order and the Haldane insulator. We then describe our system and analyze the symmetry of the parametric process. Next, we show numerical simulations of the driven-dissipative dynamics showing the evolution of the hidden order are shown. Lastly, we discuss a conventional one-photon coherent drive which breaks the symmetry of the Haldane phase.

5.1 Introduction to Haldane insulator

5.1.1 Hidden order in the Spin-1 Heisenberg antiferromagnetic chain

In 1982, Haldane, using a field theory analysis, predicted that the ground state of the Heisenberg antiferromagnetic (HA) chain was gapped with exponential decay of spin correlations for integer spins, but gapless with power-law decay of spin correlations for half-integer spin [249]. The Hamiltonian describing the HA chain is

$$\hat{H}_{\text{Heisenberg}} = -J \sum_j \hat{\mathbf{S}}_j \cdot \hat{\mathbf{S}}_{j+1}, \quad (5.1)$$

where $\hat{\mathbf{S}}_j$ is a spin operator acting at site n . However, it was later discovered by Den Nijs and Rommelse that the spin-1 Heisenberg antiferromagnetic chain could still exhibit some kind of 'hidden' long-range order [250], measurable by a non-vanishing string order (SO) parameter defined as

$$\mathcal{O}_S^\alpha = \lim_{|i-j| \rightarrow \infty} \langle \hat{S}_i^\alpha e^{i\pi \sum_{k=j+1}^{i-1} \hat{S}_k^\alpha} \hat{S}_j^\alpha \rangle, \quad (5.2)$$

and a vanishing density-wave order (DWO),

$$\mathcal{O}_{\text{DW}}^\alpha = \lim_{|i-j| \rightarrow \infty} \langle \hat{S}_i^\alpha \hat{S}_j^\alpha \rangle, \quad (5.3)$$

where $\alpha \in \{x, y, z\}$. The hidden order of a spin-1 chain can be visualized as a diluted antiferromagnetic order with alternating up spins $|+\rangle$ and down spins $|-\rangle$ with an arbitrary number of zero spins $|0\rangle$ in between, e.g. $|+ - 00 + 00 - \dots\rangle$ or $|00 + 0 - 00 + \dots\rangle$. Since knowing the configuration of one spin does not give informations about the state of the another spin, this structure is ‘hidden’ in the sense that the DWO is zero.

To gain more intuitions on the string order, in 1992, Kennedy and Tasaki proposed a non-local unitary operator which mapped the string order to the ferromagnetic order [246]. The operator can be written compactly as [251],

$$\hat{U} = \prod_{i < j} e^{i\pi \hat{S}_i^z \hat{S}_j^x}, \quad (5.4)$$

so that the non-local SO is mapped to a usual ferromagnetic order (FO), i.e.

$$U \left(\hat{S}_i^\alpha e^{i\pi \sum_{k=i+1}^{j-1} \hat{S}_k^\alpha} \hat{S}_j^\alpha \right) \hat{U}^{-1} = \hat{S}_i^\alpha \hat{S}_j^\alpha. \quad (5.5)$$

In the same paper, Kennedy and Tasaki analyzed some classes of Hamiltonians \hat{H} , whose transformed Hamiltonian $\hat{\hat{H}} = \hat{U} \hat{H} \hat{U}^{-1}$ exhibits the ferromagnetic order. The main observation is that such $\hat{\hat{H}}$ has to be local and the *sufficient* condition is that H itself is local and has the global $D_2 = Z_2 \times Z_2$ symmetry, i.e. π -rotation about about x, y, z axes or equivalently $\hat{T} \hat{H} \hat{T}^{-1} = H$, where $\hat{T} = e^{i\pi \sum_k \hat{S}_k^\alpha}$. One Hamiltonian that satisfies the above conditions is

$$\hat{H}_{\text{spin}} = \sum_j \left(\hat{S}_j^x \hat{S}_{j+1}^x + \hat{S}_j^y \hat{S}_{j+1}^y + \lambda \hat{S}_j^z \hat{S}_{j+1}^z + D(\hat{S}_j^z)^2 \right). \quad (5.6)$$

where λ and D are real numbers. This spin Hamiltonian will be later

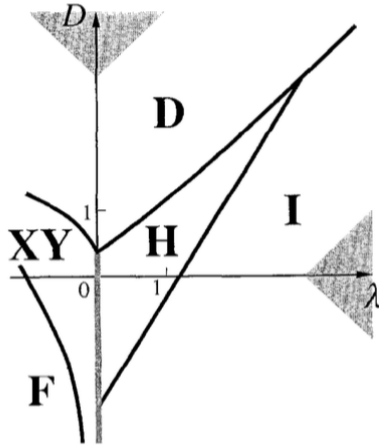


Fig. 5.1. Ground-state phase diagram of a spin chain system in Eq.(5.6). This model is related to the extended Bose-Hubbard model as described later in the text. For $D, \lambda > 0$, it contains the Ferromagnetic or large-D phase (D), the antiferromagnetic phase (I) and the Haldane phase (H). The result is reproduced from Ref. [246].

related to the extended Bose-Hubbard model that exhibits the HI phase. The ground-state phase diagram of Eq.(5.6) is reproduced here in Fig.5.1. It contains the ferromagnetic phase where an eigenvalue of \hat{S}_j^z is zero for all sites, the ferromagnetic phase, the antiferromagnetic phase and the Haldane phase.

The hidden order of the Haldane phase is robust against any small local perturbations that do not break the D_2 symmetry because in the transformed picture, those perturbations are simply local perturbations acting against a robust ferromagnetic order. Later studies also found that the existence of the string order is related to the edge states which are also robust against symmetry-preserving perturbations. The Haldane phase was one of the first examples of a new type of matter which was later known as symmetry-protected topological phases [236, 237].

5.1.2 The Extended Bose-Hubbard model

In 2006, Torre et al [243] made an analogy between the spin-1 chain and the extended Bose-Hubbard model (EBHM) of the bosonic lattice system,

i.e.,

$$\hat{H}_{\text{EBH}} = -J \sum_i \left(\hat{a}_j^\dagger \hat{a}_{j+1} + h.c. \right) + \frac{U}{2} \sum_j \hat{n}_j (\hat{n}_j - 1) + V \sum_j \hat{n}_j \hat{n}_{j+1} \quad (5.7)$$

where J is the hopping coefficient, U is the repulsion term, V is the nearest-neighbour coupling, a is a bosonic annihilator and $n_i = a_i^\dagger a_i$. The analogy can be made explicitly by having a unit-filling, defined by the total number of particles divided by the number of sites, and truncating the particle number on each site to be $n_i = 0, 1, 2$, which is justified by a large enough U/J . Hence we have $a_i \rightarrow S_i^+ / \sqrt{2}$, $a_i^\dagger \rightarrow S_i^- / \sqrt{2}$ and $n_i \rightarrow 1 - S_j^z$ ($\hbar = 1$). By working on the canonical ensemble where the unit-filling condition is fixed by the initial condition, one can map Eq.5.7 to Eq.5.6, where $J = 1$, $D = U/2$ and $V = \lambda$. Therefore, the extended Bose-Hubbard model can exhibit a topologically-nontrivial phase similar to the Haldane phase. This new phase is then named the Haldane insulator (HI). The phase diagram of the EBH model is calculated in [245].

The HI phase can be characterized by a non-vanishing string order, which in this case is expressed as:

$$\mathcal{O}_S = \lim_{|i-j| \rightarrow \infty} \langle \delta n_i e^{i\pi \sum_{k=i+1}^{j-1} \delta n_k} \delta n_j \rangle, \quad (5.8)$$

and a vanishing density-wave order

$$\mathcal{O}_{DW} = \lim_{|i-j| \rightarrow \infty} (-1)^{|i-j|} \langle \delta n_i \delta n_j \rangle, \quad (5.9)$$

where $\delta n_i = n_i - \langle n \rangle$ and $\langle n \rangle$ is a filling factor, set to one by the initial condition. The phase diagram of the extended Bose-Hubbard model, computed numerically by Rossini and Fazio [245], is reproduced here in Fig.5.2. It contains the Mott insulator (MI), the Haldane Insulator (HI) and the density-wave insulator (DW) phases. At large enough U/J , this

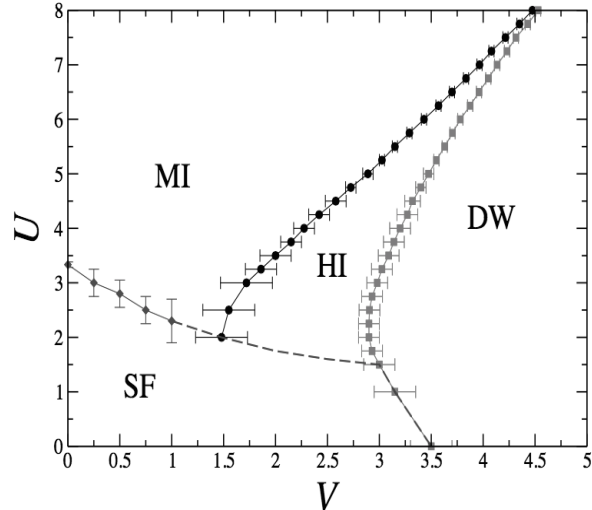


Fig. 5.2. Ground-state phase diagram of the extended Bose-Hubbard model, computed using DMRG by Rossini and Fazio ($J = 1$) [245]. It contains the Mott insulator (MI), the Haldane Insulator (HI) and the density-wave insulator (DW) phases. At large enough U/J , this phase diagram can be related to the phase diagram for the spin chain in Fig.5.1 using the mapping described in the text. MI, HI and DW phases are mapped to the large-D phase, the Haldane phase and the anti-ferromagnetic phase, respectively.

phase diagram can be related to the phase diagram for the spin chain in Fig.5.1 using the above mapping. MI, HI and DW phases are mapped to the large-D phase, the Haldane phase and the anti-ferromagnetic phase, respectively.

5.2 The system

We consider a 1D coupled nonlinear resonator array described by the Hamiltonian $\hat{H}_{\text{tot}}^{\text{Lab}} = \hat{H}_0 + \hat{H}_{\text{drv}}^{\text{par}}$, where \hat{H}_0 is the extended Bose-Hubbard (EBH) model ($\hbar = 1$),

$$\begin{aligned} \hat{H}_0^{\text{Lab}} = & \omega_r \sum_{j=0}^{L-1} \hat{n}_j - J \sum_{j=0}^{L-2} \left(\hat{a}_j^\dagger \hat{a}_{j+1} + H.c. \right) \\ & + \frac{U}{2} \sum_{j=0}^{L-1} \hat{n}_j (\hat{n}_j - 1) + V \sum_{j=0}^{L-2} \hat{n}_j \hat{n}_{j+1}, \end{aligned} \quad (5.10)$$

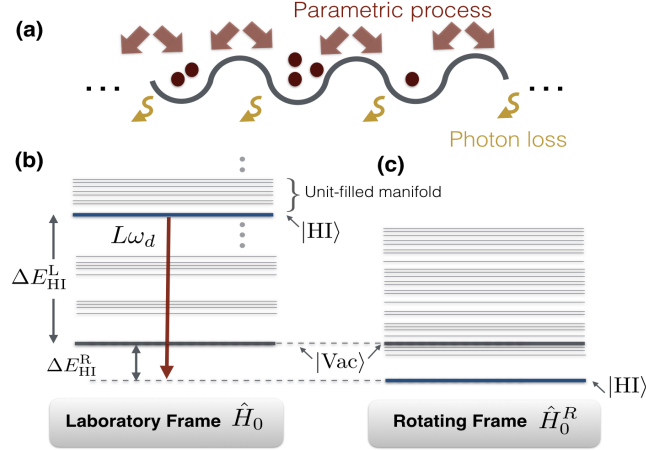


Fig. 5.3. (a) Sketch of the one-dimensional lossy photonic lattice described by the EBH model and driven by parametric drive. Lower panels are energy spectra of the undriven Hamiltonian in Eq.5.10. (b) the laboratory frame and (c) the rotating frame. The red arrow indicates the energy shift $L\omega_d$ of the HI state due to the rotating frame. Since the HI state is a unit-filled state, its energy will be lowered by $L\omega_d$.

where ω_r is the frequency of the resonator. Throughout the paper we will consider the regime $U \gg J$ which allows us to map the bosonic system onto a spin-1 chain as detailed below. The system is subjected to two-photon nearest-neighbor parametric driving [76, 129, 248]

$$\hat{H}_{\text{drv}}^{\text{par}} = \Omega \sum_{j=0}^{L-2} (\hat{a}_j \hat{a}_{j+1} e^{2i\omega_d t} + H.c.), \quad (5.11)$$

where ω_d is the driving frequency and Ω is the amplitude of the drive. A detailed discussion on circuit-QED implementations of this Hamiltonian including parametric drives is presented in Appendix 5.6. We remove the time dependence of the drive by going to the rotating frame defined by $\hat{R} = \exp(i\omega_d t \sum_{j=0}^{L-1} \hat{n}_j)$. The new Hamiltonian is

$$\begin{aligned} \hat{H}_{\text{tot}}^{\text{R}} &= \hat{R} \hat{H}_{\text{tot}}^{\text{Lab}} \hat{R}^\dagger - i \hat{R} \partial_t \hat{R}^\dagger \\ &= \hat{H}_0^{\text{R}} + \hat{H}_{\text{drv}}^{\text{R}}, \end{aligned} \quad (5.12)$$

where

$$\begin{aligned} \hat{H}_0^R = & -\mu \sum_{j=0}^{L-1} \hat{n}_j - J \sum_{j=0}^{L-1} (\hat{a}_j^\dagger \hat{a}_{j+1} + H.c.) \\ & + \frac{U}{2} \sum_{j=0}^{L-1} \hat{n}_j (\hat{n}_j - 1) + V \sum_{j=0}^{L-2} \hat{n}_j \hat{n}_{j+1}, \end{aligned} \quad (5.13)$$

$$\hat{H}_{\text{drv}}^R = \Omega \sum_{j=0}^{L-2} (\hat{a}_j \hat{a}_{j+1} + H.c.), \quad (5.14)$$

and $\mu = \omega_d - \omega_r$ is the detuning. In the following discussion, we will analyze the properties of \hat{H}_{tot}^R both when $\Omega = 0$ and $\Omega > 0$. The driven-dissipative dynamics is governed by the Master equation,

$$\frac{\partial}{\partial t} \hat{\rho} = -i[\hat{H}_{\text{tot}}^R, \hat{\rho}] - \frac{\gamma}{2} \sum_{j=0}^{L-1} (\{\hat{n}_j, \hat{\rho}\} - 2\hat{a}_j \hat{\rho} \hat{a}_j^\dagger), \quad (5.15)$$

where γ is the dissipation rate, ρ is the density matrix of the system.

We study the quantum phase via hidden order defined by a non-vanishing string order (SO) and a vanishing density-wave order (DWO) [243]. The vanishing DWO implies that quantum fluctuations between two distant sites are uncorrelated. Yet the non-vanishing SO implies that these fluctuations exhibit a certain infinitely long-range structure which is ‘hidden’ from DWO. Note that the string order operator is not hermitian, hence SO is not a correlation function. This hidden order is used to characterize the topological Haldane phase with unit filling in the equilibrium context as discussed earlier. Non-equilibrium quench dynamics and thermalization of SO in the context of the spin-chain system have been studied in Ref. [252, 253]. In Ref. [252, 253], the authors assume that the starting state already has SO. In contrast, here we show in Sec. 5.4 that SO can be generated from the vacuum in the driven-dissipative scenario.

5.3 Symmetry of the two-photon parametric process

In this section, we will analyze the symmetry of the two-photon parametric process by mapping the bosonic system into a spin-chain system. Then we analytically and numerically show that SO of the Haldane phase is robust against weak parametric driving.

We first examine the energy spectrum of the EBH model in the context of the coupled resonator array, ignoring dissipation. The EBH model conserves the number particles, hence the excited states can be grouped into manifolds labelled by the total number of particles N which is an eigenvalue of $\sum_j \hat{n}_j$. Since we work in a regime far from the ultra-strong coupling regime, i.e. $\omega_r \gg J, U, V$, the ground state of the undriven system is the vacuum, see Fig. 5.3(b). It has been shown that, at appropriate parameter regimes, the lowest energy state in the unit-filled manifold ($N = L$) shows the topological Haldane insulator (HI) phase, exhibiting the hidden order [243, 244, 245]. We label the many-body state in this phase as $|\text{HI}\rangle$.

As will be shown below, the detuning μ can be chosen such that $|\text{HI}\rangle$ becomes a gapped ground state of \hat{H}_0^{R} , see Fig. 5.3(c). We consider a weak drive $\Omega < U, V, J$ such that the filling factor of $|\text{HI}\rangle$ is approximately unaffected by the drive due to the gap. We numerically confirm that this approximation is valid below. We then map the bosonic system onto a spin-1 chain model by only keeping states with site occupation of up to 2 photons. This is justified by the large on-site interaction $U \gg J$ required for the insulating phases. As a result, the bosonic Fock states $\{|0\rangle_f, |1\rangle_f, |2\rangle_f\}$ can be replaced by the spin-1 states $\{|+\rangle_s, |0\rangle_s, |-\rangle_s\}$. The bosonic operators can be replaced with spin-1 operators, i.e., $\hat{a}_j \rightarrow \hat{S}_j^+/\sqrt{2}$ and $\hat{n}_j \rightarrow \hat{1} - \hat{S}_j^z$.

In the spin-chain picture, the total bosonic Hamiltonian $\hat{H}_{\text{tot}}^{\text{R}}$ becomes

$$\begin{aligned}\hat{H}_{\text{tot,par}}^{\text{S}} &= \sum_{j=0}^{L-2} \left((J + \Omega) \hat{S}_j^x \hat{S}_{j+1}^x + (J - \Omega) \hat{S}_j^y \hat{S}_{j+1}^y \right) \\ &\quad + V \sum_{j=0}^{L-2} \hat{S}_j^z \hat{S}_{j+1}^z + \frac{U}{2} \sum_{j=0}^{L-1} (\hat{S}_j^z)^2.\end{aligned}\quad (5.16)$$

An additional term $(-\mu + U/2 + V) \sum_j \hat{S}_j^z$ has been dropped, as it is approximately zero since we assume that the ground state of the undriven system has unit filling and the drive is weak. The system has the global $D_2 = Z_2 \times Z_2$ symmetry, i.e. π -rotation of all spins about X , Y , and Z axes. One can see that the presence of the weak parametric process does not alter this symmetry.

To understand how symmetry breaking perturbations affect the HI state using a mean-field approximation, let us consider the unitary transformation [246]

$$\hat{U}_{KT} = \prod_{i < j} \exp(i\pi \hat{S}_i^z \hat{S}_j^x). \quad (5.17)$$

This transformation is defined such that the non-local SO will be transformed into local order so that the mean-field approximation can be applied. The transformed Hamiltonian is

$$\begin{aligned}\hat{U}_{KT} \hat{H}_{\text{tot,par}}^{\text{S}} \hat{U}_{KT}^{-1} &= - (J + \Omega) \sum_{j=0}^{L-2} \hat{S}_j^x \hat{S}_{j+1}^x \\ &\quad - (J - \Omega) \sum_{j=0}^{L-2} \hat{S}_j^y \exp\left(i\pi(\hat{S}_j^z + \hat{S}_{j+1}^x)\right) \hat{S}_{j+1}^y \\ &\quad - V \sum_{j=0}^{L-2} \hat{S}_j^z \hat{S}_{j+1}^z + \frac{U}{2} \sum_{j=0}^{L-1} (\hat{S}_j^z)^2.\end{aligned}\quad (5.18)$$

We see that this Hamiltonian still involves only nearest-neighbor terms even though the transformation is non-local. This is due to the global

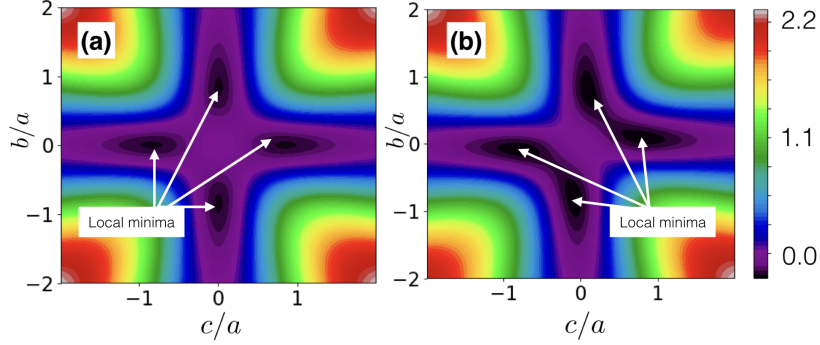


Fig. 5.4. Mean-field energy landscape E_{MF} plotted against b/a and c/a with $V = 2.8J$ and $U = 5J$. (a) In the absence of drive $\Omega = 0$, the variational ferromagnetic ground state has 4-fold ground-state degeneracy, reflecting the global D_2 symmetry of the HI phase. (b) With a weak parametric drive $\Omega = 0.1J$, the ground states remain 4-fold degenerate. Hence the symmetry is unbroken.

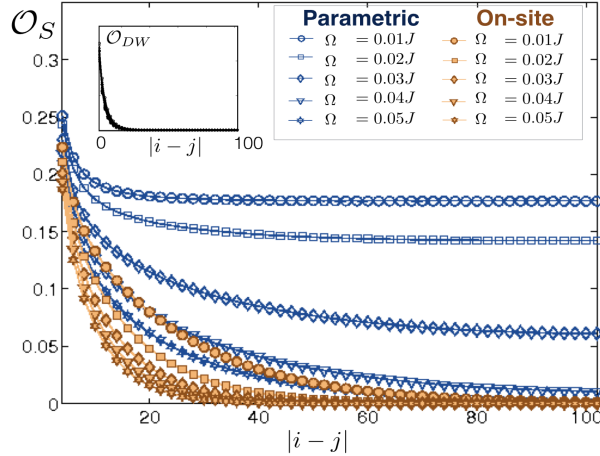


Fig. 5.5. DMRG calculations of SO and DWO of the ground state of \hat{H}_{tot}^R with $\mu = 7.5J$, $U = 5J$ and $V = 3.3J$. It shows that weak parametric drives preserve the HI phase which is characterized by a non-vanishing SO and a vanishing DWO. Both SO and DWO are zero when on-site drives are used, indicating that the HI phase is destroyed. The DMRG calculations were performed with open boundary conditions and the bond dimension of 200. The system's size is $L = 300$. The local Hilbert space in the numerics is truncated at the four photon Fock state. ($\Delta E_{\text{HI}}^R = \langle \text{HI} | \hat{H}_0^R | \text{HI} \rangle \approx -1.22LJ$ and $\Delta E_{\text{HI}}^L = \langle \text{HI} | \hat{H}_0^L | \text{HI} \rangle \approx 6.28LJ$).

D_2 symmetry of the Hamiltonian. Local terms that break the global D_2 symmetry will be transformed into non-local terms in this picture. As shown in Ref. [246], the motivation for using \hat{U}_{KT} is that SO in the original picture will be transformed into ferromagnetic order (FMO), i.e.,

$$\hat{U}_{KT} \left(\hat{S}_j^z e^{i\pi \sum_{k=j+1}^{j-1} \hat{S}_k^z} \hat{S}_j^z \right) \hat{U}_{KT}^{-1} = \hat{S}_j^z \hat{S}_j^z. \quad (5.19)$$

Below we show that FMO is stable against weak parametric driving using a simple mean-field analysis as in Ref. [246] which is then backed up quantitatively by density matrix renormalization group (DMRG) calculations [26].

The mean-field energy is defined as $E_{\text{MF}} \equiv \langle \Phi | \hat{U}_{KT} \hat{H}_{\text{tot}}^S \hat{U}_{KT}^{-1} | \Phi \rangle$, where $|\Phi\rangle = \otimes_j A_j |\phi\rangle_j$ is a homogenous product state ansatz, $|\phi\rangle_j = a|0\rangle_j + b|+\rangle_j + c|-\rangle_j$ is a local state, $A_j = 0/\sqrt{|a|^2 + |b|^2 + |c|^2}$ is a normalization factor, and a, b, c are complex numbers. The mean-field energy takes the form

$$\begin{aligned} E_{\text{MF}} = & \{|a|^2 + |b|^2 + |c|^2\}^{-2} \left[\left(\frac{U}{2} - V \right) (|b|^4 + |c|^4) \right. \\ & + 2 \left(\frac{U}{2} + V \right) |b|^2 |c|^2 + \left(\frac{U}{2} - 2J \right) |a|^2 (|b|^2 + |c|^2) \\ & \left. - \text{Re} \{ 2Ja^2 (b^{*2} + c^{*2}) + 4\Omega |a|^2 b (c + c^*) \} \right] \end{aligned} \quad (5.20)$$

where $\bar{\cdot}$ indicates a complex conjugate. E_{MF} is minimized when the last two terms inside $\text{Re}\{\dots\}$ are maximized. This happens when when a, b and c are real. Without loss of generality, we can set $a = 1$ and get

$$\begin{aligned} E_{\text{MF}} = & \{1 + b^2 + c^2\}^{-2} \left[\left(\frac{U}{2} - V \right) (b^4 + c^4) + 2 \left(\frac{U}{2} + V \right) b^2 c^2 \right. \\ & \left. + \left(\frac{U}{2} - 4J \right) (b^2 + c^2) - 8\Omega bc \right]. \end{aligned} \quad (5.21)$$

The mean-field energy landscape is shown in Fig. 5.4 with $U = 5J$ and $V = 2.8J$. When $\Omega = 0$, E_{MF} displays four degenerate FM ground states.

This reflects the global D_2 symmetry of the corresponding HI phase because the global D_2 symmetry implies that the state is invariant under the global π -rotation about x, y, z axes. Nevertheless, π -rotation around x and y axes also implies π -rotation around z axis. Hence the degeneracy is 4-fold. With weak parametric drive $\Omega = 0.1J$, the FM ground states remain four-fold degenerate, confirming that the D_2 symmetry is unbroken.

To corroborate the mean-field picture quantitatively we performed DMRG calculations on the bosonic Hamiltonian $\hat{H}_{\text{tot}}^{\text{R}}$ in the rotating frame. The degenerate ground states of the HI phase are lifted by forcing the edge sites to have no photon at one end and two photons at another end. The HI state was found as the ground state of \hat{H}_0^{R} by numerically scanning μ . When $\Omega > 0$, the SO and the DWO of the ground state for different Ω are shown in Fig. 5.5. It confirms that the HI phase is stable against weak parametric driving.

5.4 The emergence of the hidden order

In this section, we turn into the driven-dissipative scenario far from equilibrium which involves photon loss. The dynamics of the system is now described by the Lindblad master equation Eq. 5.15. Time evolution is obtained by solving the Lindblad Master equation (Eq. 5.15) using the quantum trajectories [227] and the Time-Evolving Block Decimation (TEBD) algorithm [216, 217]. We start from the vacuum and switch on suddenly the parametric drive.

In Fig. 5.6, we plot SO and DWO measured at the time $t' = 0.25/J$ as a function of $|i-j|$ for different driving amplitudes $\Omega/J = 0.5, 1.0, 1.25, 1.5, 2.0$. The parameters are chosen such that the lowest energy state in the unit-filled manifold of \hat{H}_0 is in the Haldane state $|\text{HI}\rangle$. The frequency ω_d is chosen to be resonant with the transition between the vacuum state and

$|\text{HI}\rangle$, i.e. $\omega_d = \Delta E_{\text{HI}}^L/L$. Note that this frequency is different than the one used in the previous section. It can be seen that at this time SO is finite and increases with the driving amplitude Ω , while DWO remains zero.

In Fig. 5.7(a)-(c), we plot the filling factor, OS, and DWO as a function of time. We observe the hidden order in the transient dynamics emerging from the vacuum but eventually dies out at the steady state. We observe that the maximum value of the hidden order is increased with the amplitude of the drive, as also seen in Fig. 5.6. However, the duration that the hidden order exists is reduced for a stronger drive. We found that the optimal value of the driving amplitude is around $1.25J - 1.5J$, where the maximum OS is ~ 0.05 and the existence duration is $\sim 1/\Omega$.

We found that when OS is at maximum, the overlap $\text{Tr}(\hat{\rho}(t)|\text{HI}\rangle\langle\text{HI}|)$ is in the order of 10^{-3} . This small overlap implies that the system is far from the equilibrium Haldane state. This is expected as the latter is defined for an insulating unit-filled state, while here the number of particles is not conserved due to the coherent drive and losses. However, the emergence of the string order here is intimately related to the symmetry of the equilibrium Haldane phase. As will be discussed in the next section, when the parametric drive is replaced by an on-site driving that breaks the symmetry of the equilibrium Haldane phase, the hidden order cannot emerge from the vacuum. Finally, we note that the emergence of the hidden order from the vacuum here does not imply that two distant spins are correlated immediately after the quench since $\text{DWO} = 0$.

In Fig. 5.7(d)-(f) we study the effect of photon loss. For the parameter regime given in the caption of Fig. 5.7(d)-(f), we find that without loss OS reaches its maximum of $\text{OS} \sim 0.1$ at $Jt \sim 2$. The maximum OS is reduced to 0.05 when $\gamma = 0.05J$ and continues to decrease as γ is increased. The rapid reduction of OS when γ is non-zero comes from the fact that a single photon loss can destroy OS since it breaks the symmetry and becomes

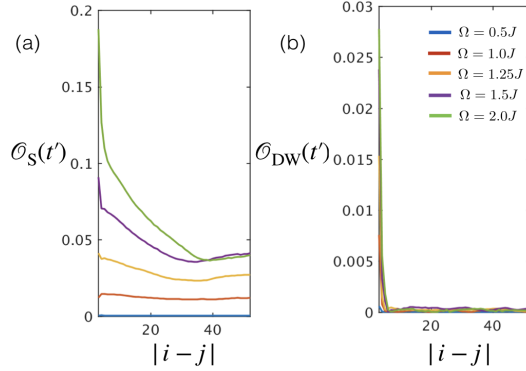


Fig. 5.6. **Hidden order at a transient time during the driven-dissipative dynamics.** Time evolution of the system ($L = 100$) evolving under Eq. (5.15) with parametric drive, obtained using the quantum trajectories with 200 trajectories and the TEBD algorithm with the bond dimension of 100. (a) SO and (b) DWO measured at the time $t' = 0.25/J$ as a function of $|i - j|$ for different driving amplitudes $\Omega/J = 0.5, 1.0, 1.25, 1.5, 2.0$.

non-local in the transformed picture discussed in Sec 5.3. At $Jt = 2$, there are about $\bar{n}(2/J)L \sim 50$ photons in the system. Hence the decay rate is $\sim 50\gamma = 2.5J$ comparable to the hopping rate.

In Fig. 5.7(e)-(i), we study the effect of the V -term. We found that when $V = 0$, a transient SO order still exists. However, in the same regime we observe a large transient DWO whose magnitude is larger than SO. This implies that there is no hidden order during the evolution [246]. As V is increased, this DWO is strongly suppressed while the SO remains appreciable leading to the transient hidden order.

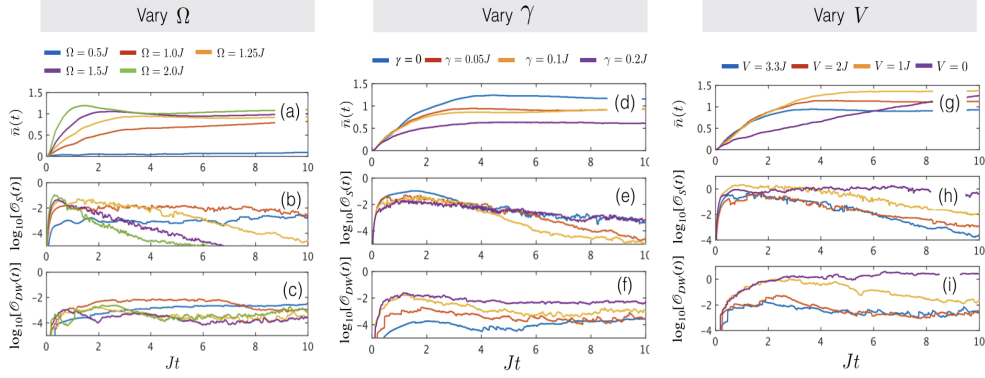


Fig. 5.7. **Rise and fall of the hidden order in the driven-dissipative dynamics.** Time evolution of the system ($L = 50$) evolving under Eq. (5.15) with parametric drive, obtained using the quantum trajectories with 100 trajectories and the TEBD algorithm with the bond dimension of 100. In (a)-(c), we vary the amplitude of the drive with $\mu = 6.28J$, $U = 5J$, $V = 3.3J$, and $\gamma = 0.05J$. In (d)-(f), we vary the photon loss rate with $\mu = 6.28J$, $U = 5J$, $V = 3.3J$, and $\Omega = 1.25J$. In (g)-(i), we vary V with $\mu = 6.28J$, $U = 5J$, $\gamma = 0.05J$, and $\Omega = 1.25J$.

5.5 Comparison with on-site coherent drive

Although the nearest-neighbor parametric driving discussed so far has been experimentally realized [248]. It is not a common drive used in quantum optics. Previous literatures instead consider a more conventional one-photon drive [254, 255, 256, 128, 257, 258, 259, 131]

$$\hat{H}_{\text{local}} = \Omega \sum_{j=0}^{L-1} (\hat{a}_j e^{i\omega_d t} + \hat{a}_j^\dagger e^{-i\omega_d t}). \quad (5.22)$$

In this section we will show that this drive has a different symmetry than the two-photon drive discussed in the previous section. To see this, let us consider the rotating frame defined by \hat{R} as before. In this frame the drive becomes

$$\hat{H}_{\text{local}}^{\text{R}} = -\omega_p \sum_{j=0}^{L-1} \hat{n}_j + \Omega \sum_{j=0}^{L-1} (\hat{a}_j + \hat{a}_j^\dagger). \quad (5.23)$$

Assuming a weak drive and mapping the system to a spin-chain system, the total Hamiltonian becomes

$$\begin{aligned} \hat{H}_{\text{tot,loc}}^S = & \sum_{j=0}^{L-1} \left(J \hat{S}_j^x \hat{S}_{j+1}^x + J \hat{S}_j^y \hat{S}_{j+1}^y + V \hat{S}_j^z \hat{S}_{j+1}^z \right) \\ & + \sum_{j=0}^{L-1} \left(\frac{U}{2} (\hat{S}_j^z)^2 + \Omega \hat{S}_j^x \right). \end{aligned} \quad (5.24)$$

Again the term $\sum_j \hat{S}_j^z$ is dropped due to the unit-filling condition. We can see that the term $\Omega \hat{S}_j^x$ is not invariant under the transformation $\hat{S}_j^x \rightarrow -\hat{S}_j^x$. Hence it breaks the global D_2 symmetry. When applying the non-local unitary transformation \hat{U}_{KT} , the terms becomes

$$\hat{U}_{\text{KT}} \left(\sum_{j=0}^{L-1} \hat{S}_j^x \right) \hat{U}_{\text{KT}}^{-1} = \sum_{j=0}^L \hat{S}_j^x \exp \left(i\pi \sum_{k=j+1}^L \hat{S}_k^x \right), \quad (5.25)$$

which is highly non-local. Hence the FM phase in the transformed picture will be destroyed even for a weak drive. In the original picture, this means that $|\text{HI}\rangle$ and its string order is destroyed in the presence of the on-site drive. This is confirmed by DMRG calculations, shown in Fig. 5.5. When performing the time evolution including dissipation using TEBD calculations, we also found that the SO remains zero throughout the time evolution.

5.6 Implementation of parametric pumping using circuit QED

In this section, we propose an implementation of the Bose-Hubbard model driven by parametric pumping, using circuit-QED architecture. The cross-Kerr nonlinearity term $V n_j n_{j+1}$ has already been discussed and implemented in the literature [77] and can be integrated to our circuit. Nevertheless, circuit designs discussed in [77] do lead to extra terms in the

Hamiltonian that needed further investigation.

Our circuit diagram is shown in Fig.5.8. The flux variable is defined as $\phi_j = -\int V_j dt$, where V_j is a voltage at the corresponding position. As will be shown below, this quantity can be quantized to the form $\hat{\phi}_j = \alpha(\hat{a}_j + \hat{a}_j^\dagger)$, where $\hat{a}_j, \hat{a}_j^\dagger$ are bosonic operators of an ‘artificial’ photon at site j and α is some constant that depends on the circuit’s elements. We first describe the rules of Josephson junctions which introduce various kinds of nonlinearities to the system and then explicitly show how to quantize the circuit.

The first Josephson junction $E_{J,U}$ (labelled in orange in Fig.5.8) corresponds to a $\chi^{(3)}$ nonlinear material, which gives rise to the on-site Kerr nonlinearity $\frac{U}{2}n_j(n_j - 1)$. The junction is biased by the magnetic flux $\Phi_g = \pi\phi_0$, where $\phi_0 = \hbar/2e$, and shunted by a small inductor L' to produce a repulsive interaction $U > 0$. The second Josephson junction E_{J,Ω_p} (labelled in yellow in Fig.5.8) corresponds to a $\chi^{(2)}$ nonlinear material, which responsible for a parametric-down-conversion (PDC) process. The PDC process converts a pumped photon with frequency $2\omega_p$ into a pair of photons with frequency ω_p . Here the pumped photons come from an oscillating flux bias $\Phi_b(t) = \pi\phi_0/2 + \phi_b(t)$.

As discussed in [76], this PDC process leads to both nearest-neighbor parametric pumping of the form $(\hat{a}_j^\dagger \hat{a}_{j+1}^\dagger + h.c.)$ and on-site parametric pumping of the form $(\hat{a}_j^{\dagger 2} + \hat{a}_j^2)$. The latter can be eliminated by introducing an extra on-site PDC process (labelled in a dotted box in Fig.5.8). This extra component is driven by a coherent voltage source ψ , whose phase differs from that of $\phi_b(t)$ by π .

We now show how to quantize the the circuit by following the standard procedure [135]. We first write down the circuit’s Lagrangian as $\mathcal{L} =$

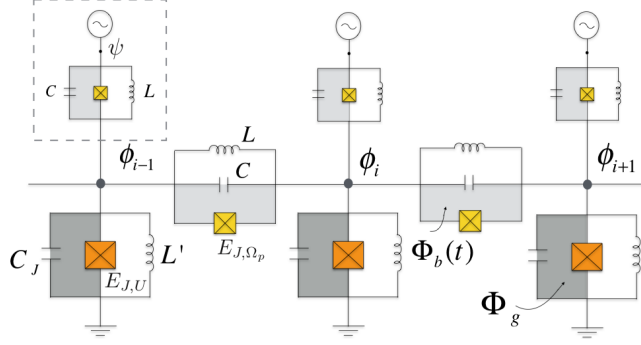


Fig. 5.8. Proposed circuit diagram that implements the Bose-Hubbard model and parametric driving.

$\sum_j (\mathcal{L}_j^{\text{on-site}} + \mathcal{L}_j^{\text{hopping}} + \mathcal{L}_j^{\text{pump}} + \mathcal{L}_j^{\text{onsite-PDC}})$ where

$$\mathcal{L}_j^{\text{on-site}} = \frac{1}{2} C_J \dot{\phi}_j^2 - \frac{1}{2L'} \phi_j^2 + E_{J,U} \cos\left(\frac{\phi_j + \pi\phi_0}{\phi_0}\right), \quad (5.26)$$

$$\mathcal{L}_j^{\text{hopping}} = \frac{1}{2} C (\dot{\phi}_j - \dot{\phi}_{j+1})^2 - \frac{1}{2L} (\phi_j - \phi_{j+1})^2, \quad (5.27)$$

$$\mathcal{L}_j^{\text{pump}} = E_{J,\Omega_p} \cos\left(\frac{\phi_j - \phi_{j+1} + \pi\phi_0/2 + \phi_b(t)}{\phi_0}\right), \quad (5.28)$$

$$\mathcal{L}_j^{\text{onsite-PDC}} = \frac{1}{2} C (\dot{\phi}_j - \dot{\psi})^2 + E_{J,\Omega_p} \cos\left(\frac{\phi_j - \psi + \pi\phi_0/2}{\phi_0}\right) \quad (5.29)$$

Assuming $C/(C_J + 3C) \ll 1$, the Hamiltonian can then be obtained using the Legendre transformation [226]. A conjugate momentum of ϕ_j is defined as $q_j = \sqrt{3C + C_J} \partial \mathcal{L} / \partial \dot{\phi}_j$. Both ϕ_j and q_j are then quantized by defining ladder operators $\hat{a}_j, \hat{a}_j^\dagger$ according to

$$\hat{\phi}_j = (\tilde{L}/4\tilde{C})^{1/4} (\hat{a}_j + \hat{a}_j^\dagger), \quad (5.30)$$

$$\hat{q}_j = i(\tilde{C}/4\tilde{L})^{1/4} (-\hat{a}_j + \hat{a}_j^\dagger), \quad (5.31)$$

where $\tilde{C} = C_J + 3C$ and $\tilde{L} = [1/L' + 3/L - E_{J,U}/\phi_0^2]^{-1}$ are effective capacitance and effective inductance, respectively. It follows that $[\hat{a}_j, \hat{a}_j^\dagger] = \delta_{ij}$. In addition, after the Legendre transformation, the quadratic terms in \mathcal{L} are transformed into $\sum_j \omega_c \hat{a}_j^\dagger \hat{a}_j$, where $\omega_c = 1/\sqrt{\tilde{L}\tilde{C}}$ is a frequency of the artificial photon. We can see that by adding a small shunting inductor L' , ω_c is guaranteed to be real.

To see the emergence of the on-site Kerr nonlinearity U and PDC, we first notice that the Legendre transformation only introduces a minus sign to the ‘potential’ terms, including all the cosine terms in \mathcal{L} . Hence, the onsite-Kerr nonlinearity can be seen by expanding the cosine function in Eq.(5.26), taking into account the normal ordering as [137]

$$E_{J,U} \cos \left(\lambda(\hat{a}_j + \hat{a}_j^\dagger) \right) = E_{J,U} e^{-\lambda^2/2} \left(1 - \lambda^2 \hat{a}_j^\dagger \hat{a}_j + \frac{\lambda^4}{4} \hat{a}_j^\dagger \hat{a}_j^\dagger \hat{a}_j \hat{a}_j + \dots \right).$$

where $\lambda = (2E_{\tilde{C}}/E_{\tilde{L}})^{1/4}$, with $E_{\tilde{C}} = e^2/2\tilde{C}$ and $E_{\tilde{L}} = \phi_0^2/\tilde{L}$. For a large $E_{\tilde{L}}/E_{\tilde{C}}$, we can neglect the terms that are higher than the fourth order.

The parametric pumping term comes directly from the sine expansion in Eq.(5.28). For illustrative purpose, we neglect the normal-ordering and consider the sine expansion up to the third order as

$$E_{J,\Omega_p} \sin \left(\frac{\phi_j - \phi_{j+1} + \phi_b}{\phi_0} \right) \approx \frac{E_{J,\Omega_p}}{\phi_0} (\phi_j - \phi_{j+1}) - \frac{E_{J,\Omega_p}}{3!\phi_0^3} (\phi_j - \phi_{j+1} + \phi_b)^3,$$

where we neglect the term $E_{JJ}\phi_b/\phi_0$, since it does not act on the system. The linear term can also be eliminated by applying a current bias I at both ends of the array. After rotating wave approximation, the only third-order terms that survive are of the forms $(\hat{b}^\dagger \hat{a}_j \hat{a}_{j+1} + h.c.)$ and $(\hat{b}^\dagger \hat{a}_j^2 + \hat{b}^\dagger \hat{a}_{j+1}^2 + h.c.)$, where \hat{b}^\dagger is a creator of the field ϕ_b . The latter is cancelled by the onsite PDC process in Eq.5.29.

Finally by explicitly writing down the time dependence of \hat{b} and \hat{b}^\dagger and replacing them with c -numbers, the Hamiltonian can be cast into the form

$$\hat{\mathcal{H}} = \sum_j (\omega + \delta\omega) \hat{a}_j^\dagger \hat{a}_j + \frac{U}{2} \hat{a}_j^\dagger \hat{a}_j^\dagger \hat{a}_j \hat{a}_j - J(\hat{a}_j^\dagger \hat{a}_{j+1} + h.c.) + \Omega_p (e^{i2\omega_p t} \hat{a}_j \hat{a}_{j+1} + h.c.), \quad (5.32)$$

where $\omega = 1/\sqrt{\tilde{L}\tilde{C}}$, $\delta\omega = E_J \lambda^2 (1 - e^{-\lambda^2/2})$, $U/2 = E_J \lambda^4 e^{-\lambda^2/2}/4$ and

$J = \omega/2(\tilde{L}/L - C/\tilde{C})$. The parametric pumping coefficient Ω_p is directly proportional to E_{JJ} . However, its explicit form depends on the relation between ϕ_b and $(\hat{b} + \hat{b}^\dagger)$ and hence depends on how ϕ_b is generated.

Our circuit allows the Hamiltonian parameters to be tuned independently: μ can be tuned directly by changing ω_p , U comes from the first Josephson junction E_{JU} , J comes from the coupling LC oscillator while Ω_p independently comes from the second Josephson junction E_{J,Ω_p} . As an example, $U/J \sim 10$ can be realistically obtained by using $\tilde{L}/L \sim 5 \times 10^{-3}$, $\lambda \sim 0.4$ and $E_J/E_C \sim 10^5$ [146]. For this setting, we would have a negligible frequency correction $\delta\omega/\omega \sim 0.02$. Noted that this value of λ also ensures that it is a good approximation to expand the cosine term in Eq.(5.32) up to the fourth order, as for the case of a transmon qubit [225].

5.7 Conclusion

We have shown that the dynamics of quantum many-body system driven by parametric process can exhibit hidden order which goes beyond local order parameters. The hidden order can arise in a transient case even when symmetry-breaking dissipation is included. We show that this drive respects the symmetry of the HI phase while the conventional on-site drive does not. Our work opens a new direction to explore the role of the non-local order and symmetry in non-equilibrium settings as well as its connection to the equilibrium SPT phases.

Chapter 6

Conclusions

In this thesis, we have discussed the use of interacting photons in superconducting circuits for quantum simulations. We have explored the dynamics of quantum many-body both in the equilibrium scenario and out of equilibrium scenario including a periodically driven system, and a driven-dissipative system.

6.1 Summary of results

In Chapter 3, we experimentally implement a novel many-body spectroscopy technique based on time evolution. Using this technique, we can probe signatures of a localized to a thermalized transition of two-interacting photons by directly measuring the spreading of the energy eigenstates and statistics of the eigenenergies. These signatures are following what is expected from a many-body localization phase transition which happens in the thermodynamic limit. Moving from an equilibrium system to a periodically driven system, in Chapter 4 we explore the concept of topological pumping of interacting photons in superconducting circuits which allows reliable transport of Fock states. Our proposal can be implemented in the superconducting chip used in Chapter 3. Lastly, in Chapter 5, we study the rise of hidden order in driven-dissipative dynamics of interacting photons in coupled

resonator arrays. This infinitely-long-range order resembles that characterizing the Haldane insulator in the equilibrium context. We show that with the nearest-neighbor parametric down-conversion process, the hidden order can be driven out of the vacuum in the transient case. We argue that this behavior is due to the symmetry of drive which respects the symmetry of the Haldane phase. Our work opens a new direction to explore the use of non-local order parameters to characterize driven-dissipative dynamics of quantum many-body systems.

6.2 Future prospects

Although implementing a universal quantum simulator which requires full control over quantum many-body systems may still be decades away, tremendous experimental progress has been made during the past two decades. Two main approaches have emerged. The first approach such cold atom systems provide a global control a large ensemble of quantum particles, with possible local manipulation and measurement in some cases. The second approach such as interacting photons in superconducting circuits provide more flexibility on the local control and measurement while scaling up to 50-100 site are in current progress. For the latter, one needs to develop both new experimental techniques and new theoretical frameworks to maintain such controllability when scaling up. For example, using our spectroscopy technique developed in Chapter 3, we were able to resolve all energy eigenstates and eigenenergies of the system. This result allows us to benchmark the experiment with the theory and to reconstruct matrix elements of many-body Hamiltonians that a given circuit implements. However, when scaling up eigenenergies of the system will become too dense to be resolved by the current resolution which is limited by the coherent time of the system. Hence, obtaining full information of the Hamiltonian

of the circuit is not possible for a large system. To what extent, the disregarded information becomes essential to the physics of the system is still an open question. Constructing the Hamiltonian of the system with limited details also require a new theoretical framework. The latter also raises the question of how to systematically benchmark a quantum simulator as it approaches the limit of classical computers. Identifying problems beyond quantum physics that can only be solved with near-term quantum simulators is also an important question that drives the field forwards. With these in mind, we conclude that, due to exceptional local control systems, interacting photons in superconducting circuits, although still in its early state, is one of the promising candidates for quantum simulation.

In the future, we would like to explore possibilities to realize signatures of the fractional Hall states of light in near-term superconducting circuits as well as finding an optimized driving protocol for achieving quantum supremacy. The latter aims to demonstrate the capability of quantum devices beyond the reach of currently-available classical computers.

Bibliography

- [1] J. I. Cirac and P. Zoller, “Goals and opportunities in quantum simulation,” *Nat Phys*, vol. 8, p. 264, 04 2012. [Online]. Available: <http://dx.doi.org/10.1038/nphys2275>
- [2] P. Hauke, F. M. Cucchietti, L. Tagliacozzo, I. Deutsch, and M. Lewenstein, “Can one trust quantum simulators?” *Reports on Progress in Physics*, vol. 75, no. 8, p. 082401, 2012. [Online]. Available: <http://stacks.iop.org/0034-4885/75/i=8/a=082401>
- [3] T. H. Johnson, S. R. Clark, and D. Jaksch, “What is a quantum simulator?” *EPJ Quantum Technology*, vol. 1, no. 1, p. 10, Jul 2014. [Online]. Available: <https://doi.org/10.1140/epjqt10>
- [4] R. Blatt and C. F. Roos, “Quantum simulations with trapped ions,” *Nature Physics*, vol. 8, pp. 277 EP –, 04 2012. [Online]. Available: <http://dx.doi.org/10.1038/nphys2252>
- [5] C. Gross and I. Bloch, “Quantum simulations with ultracold atoms in optical lattices,” *Science*, vol. 357, no. 6355, pp. 995–1001, 2017. [Online]. Available: <http://science.sciencemag.org/content/357/6355/995>
- [6] G. Tosi, F. A. Mohiyaddin, V. Schmitt, S. Tenberg, R. Rahman, G. Klimeck, and A. Morello, “Silicon quantum processor with robust long-distance qubit couplings,” *Nature Communications*,

- vol. 8, no. 1, p. 450, 2017. [Online]. Available: <https://doi.org/10.1038/s41467-017-00378-x>
- [7] D. E. Chang, V. Vuletić, and M. D. Lukin, “Quantum nonlinear optics —photon by photon,” *Nature Photonics*, vol. 8, pp. 685 EP –, 08 2014. [Online]. Available: <http://dx.doi.org/10.1038/nphoton.2014.192>
- [8] T. Hensgens, T. Fujita, L. Janssen, X. Li, C. J. Van Diepen, C. Reichl, W. Wegscheider, S. Das Sarma, and L. M. K. Vandersypen, “Quantum simulation of a fermi–hubbard model using a semiconductor quantum dot array,” *Nature*, vol. 548, pp. 70 EP –, 08 2017. [Online]. Available: <http://dx.doi.org/10.1038/nature23022>
- [9] A. A. Houck, H. E. Türeci, and J. Koch, “On-chip quantum simulation with superconducting circuits,” *Nature Physics*, vol. 8, pp. 292 EP –, 04 2012. [Online]. Available: <http://dx.doi.org/10.1038/nphys2251>
- [10] N. Y. Yao, L. Jiang, A. V. Gorshkov, P. C. Maurer, G. Giedke, J. I. Cirac, and M. D. Lukin, “Scalable architecture for a room temperature solid-state quantum information processor,” *Nature Communications*, vol. 3, pp. 800 EP –, 04 2012. [Online]. Available: <http://dx.doi.org/10.1038/ncomms1788>
- [11] J. Banks, J. Carson, B. Nelson, and D. Nicol, *Discrete-Event System Simulation*, 5th ed. Prentice Hall, 2010.
- [12] N. Stephen and N. Stephen, *Cancer Drug Design and Discovery*, 1st ed. Academic Press, 2007.
- [13] D. Vallespin, K. Badcock, A. D. Ronch, M. White, P. Perfect, and M. Ghoreyshi, “Computational fluid dynamics framework for aerodynamic model assessment,” *Progress in Aerospace Sciences*,

- vol. 52, pp. 2 – 18, 2012, applied Computational Aerodynamics and High Performance Computing in the UK. [Online]. Available: <http://www.sciencedirect.com/science/article/pii/S0376042112000139>
- [14] A. Gilchrist, “Numerical simulation of climate and climatic change,” *Nature*, vol. 276, pp. 342 EP –, 11 1978. [Online]. Available: <http://dx.doi.org/10.1038/276342a0>
- [15] C. E. Carr, N. C. Bryan, K. N. Saboda, S. A. Bhattaru, G. Ruvkun, and M. T. Zuber, “Acceleration profiles and processing methods for parabolic flight,” *npj Microgravity*, vol. 4, no. 1, p. 14, 2018. [Online]. Available: <https://doi.org/10.1038/s41526-018-0050-3>
- [16] D. Benov, “The manhattan project, the first electronic computer and the monte carlo method. monte carlo methods and applications,” *Monte Carlo Methods and Applications*, vol. 22(1), pp. 73–79, 2016.
- [17] R. U. Seydel, *Tools for Computational Finance*. Springer International Publishing, 2006.
- [18] T. Häner and D. S. Steiger, “0.5 Petabyte Simulation of a 45-Qubit Quantum Circuit,” *ArXiv e-prints*, Apr. 2017.
- [19] E. Pednault, J. A. Gunnels, G. Nannicini, L. Horesh, T. Magerlein, E. Solomonik, and R. Wisnieff, “Breaking the 49-Qubit Barrier in the Simulation of Quantum Circuits,” *ArXiv e-prints*, Oct. 2017.
- [20] P. A. Lee, “From high temperature superconductivity to quantum spin liquid: progress in strong correlation physics,” *Reports on Progress in Physics*, vol. 71, no. 1, p. 012501, 2008. [Online]. Available: <http://stacks.iop.org/0034-4885/71/i=1/a=012501>
- [21] T. H. Hansson, M. Hermanns, S. H. Simon, and S. F. Viefers, “Quantum hall physics: Hierarchies and conformal field theory

- techniques,” *Rev. Mod. Phys.*, vol. 89, p. 025005, May 2017. [Online]. Available: <https://link.aps.org/doi/10.1103/RevModPhys.89.025005>
- [22] R. P. Feynman, “Simulating physics with computers,” *International Journal of Theoretical Physics*, vol. 21, no. 6, pp. 467–488, Jun 1982. [Online]. Available: <https://doi.org/10.1007/BF02650179>
- [23] S. Lloyd, “Universal quantum simulators,” *Science*, vol. 273, no. 5278, pp. 1073–1078, 1996. [Online]. Available: <http://science.sciencemag.org/content/273/5278/1073>
- [24] G. Carleo and M. Troyer, “Solving the quantum many-body problem with artificial neural networks,” *Science*, vol. 355, no. 6325, pp. 602–606, 2017. [Online]. Available: <http://science.sciencemag.org/content/355/6325/602>
- [25] R. Orus, “A practical introduction to tensor networks: Matrix product states and projected entangled pair states,” *Annals of Physics*, vol. 349, pp. 117 – 158, 2014. [Online]. Available: <http://www.sciencedirect.com/science/article/pii/S0003491614001596>
- [26] U. Schollwoeck, “The density-matrix renormalization group in the age of matrix product states,” *Annals of Physics*, vol. 96, p. 326, 2011.
- [27] R. G. Parr, “Density functional theory of atoms and molecules,” in *Horizons of Quantum Chemistry*, K. Fukui and B. Pullman, Eds. Dordrecht: Springer Netherlands, 1980, pp. 5–15.
- [28] W. von der Linden, “A quantum monte carlo approach to many-body physics,” *Physics Reports*, vol. 220, no. 2, pp. 53 – 162, 1992. [Online]. Available: <http://www.sciencedirect.com/science/article/pii/037015739290029Y>

- [29] A. J. Leggett, “What do we know about high t_c ?” *Nature Physics*, vol. 2, pp. 134 EP –, 03 2006. [Online]. Available: <http://dx.doi.org/10.1038/nphys254>
- [30] R. Nandkishore and D. A. Huse, “Many-body localization and thermalization in quantum statistical mechanics,” *Annual Review of Condensed Matter Physics*, vol. 6, no. 1, pp. 15–38, 2015. [Online]. Available: <https://doi.org/10.1146/annurev-conmatphys-031214-014726>
- [31] I. Kassal, J. D. Whitfield, A. Perdomo-Ortiz, M.-H. Yung, and A. Aspuru-Guzik, “Simulating chemistry using quantum computers,” *Annual Review of Physical Chemistry*, vol. 62, no. 1, pp. 185–207, 2011, pMID: 21166541. [Online]. Available: <https://doi.org/10.1146/annurev-physchem-032210-103512>
- [32] B. P. Lanyon, J. D. Whitfield, G. G. Gillett, M. E. Goggin, M. P. Almeida, I. Kassal, J. D. Biamonte, M. Mohseni, B. J. Powell, M. Barbieri, A. Aspuru-Guzik, and A. G. White, “Towards quantum chemistry on a quantum computer,” *Nature Chemistry*, vol. 2, pp. 106 EP –, 01 2010. [Online]. Available: <http://dx.doi.org/10.1038/nchem.483>
- [33] I. Bloch, J. Dalibard, and S. Nascimbène, “Quantum simulations with ultracold quantum gases,” *Nature Physics*, vol. 8, pp. 267 EP –, 04 2012. [Online]. Available: <http://dx.doi.org/10.1038/nphys2259>
- [34] I. Bloch, J. Dalibard, and W. Zwerger, “Many-body physics with ultracold gases,” *Rev. Mod. Phys.*, vol. 80, pp. 885–964, Jul 2008. [Online]. Available: <https://link.aps.org/doi/10.1103/RevModPhys.80.885>
- [35] M. Greiner, O. Mandel, T. Esslinger, T. W. Hänsch, and I. Bloch, “Quantum phase transition from a superfluid to a mott insulator in

- a gas of ultracold atoms,” *Nature*, vol. 415, pp. 39 EP –, 01 2002. [Online]. Available: <http://dx.doi.org/10.1038/415039a>
- [36] J. F. Sherson, C. Weitenberg, M. Endres, M. Cheneau, I. Bloch, and S. Kuhr, “Single-atom-resolved fluorescence imaging of an atomic mott insulator,” *Nature*, vol. 467, pp. 68 EP –, 08 2010. [Online]. Available: <http://dx.doi.org/10.1038/nature09378>
- [37] M. Lewenstein and A. Sanpera, “Probing quantum magnetism with cold atoms,” *Science*, vol. 319, no. 5861, pp. 292–293, 2008. [Online]. Available: <http://science.sciencemag.org/content/319/5861/292>
- [38] N. Goldman, J. C. Budich, and P. Zoller, “Topological quantum matter with ultracold gases in optical lattices,” *Nature Physics*, vol. 12, pp. 639 EP –, 06 2016. [Online]. Available: <http://dx.doi.org/10.1038/nphys3803>
- [39] L. W. Cheuk, M. A. Nichols, M. Okan, T. Gersdorf, V. V. Ramasesh, W. S. Bakr, T. Lompe, and M. W. Zwierlein, “Quantum-gas microscope for fermionic atoms,” *Phys. Rev. Lett.*, vol. 114, p. 193001, May 2015. [Online]. Available: <https://link.aps.org/doi/10.1103/PhysRevLett.114.193001>
- [40] E. Haller, J. Hudson, A. Kelly, D. A. Cotta, B. Peaudecerf, G. D. Bruce, and S. Kuhr, “Single-atom imaging of fermions in a quantum-gas microscope,” *Nature Physics*, vol. 11, pp. 738 EP –, 07 2015. [Online]. Available: <http://dx.doi.org/10.1038/nphys3403>
- [41] M. F. Parsons, F. Huber, A. Mazurenko, C. S. Chiu, W. Setiawan, K. Wooley-Brown, S. Blatt, and M. Greiner, “Site-resolved imaging of fermionic ${}^6\text{Li}$ in an optical lattice,” *Phys. Rev. Lett.*, vol. 114, p. 213002, May 2015. [Online]. Available: <https://link.aps.org/doi/10.1103/PhysRevLett.114.213002>

- [42] A. Omran, M. Boll, T. A. Hilker, K. Kleinlein, G. Salomon, I. Bloch, and C. Gross, “Microscopic observation of pauli blocking in degenerate fermionic lattice gases,” *Phys. Rev. Lett.*, vol. 115, p. 263001, Dec 2015. [Online]. Available: <https://link.aps.org/doi/10.1103/PhysRevLett.115.263001>
- [43] W. Zwerger, *The BCS-BEC Crossover and the Unitary Fermi Gas*. Springer-Verlag Berlin Heidelberg, 2012.
- [44] J.-y. Choi, S. Hild, J. Zeiher, P. Schauß, A. Rubio-Abadal, T. Yefsah, V. Khemani, D. A. Huse, I. Bloch, and C. Gross, “Exploring the many-body localization transition in two dimensions,” *Science*, vol. 352, no. 6293, pp. 1547–1552, 2016. [Online]. Available: <http://science.sciencemag.org/content/352/6293/1547>
- [45] H. Bernien, S. Schwartz, A. Keesling, H. Levine, A. Omran, H. Pichler, S. Choi, A. S. Zibrov, M. Endres, M. Greiner, V. Vuletić, and M. D. Lukin, “Probing many-body dynamics on a 51-atom quantum simulator,” *Nature*, vol. 551, pp. 579 EP –, 11 2017. [Online]. Available: <http://dx.doi.org/10.1038/nature24622>
- [46] R. Blatt and C. F. Roos, “Quantum simulations with trapped ions,” *Nature Physics*, vol. 8, pp. 277 EP –, 04 2012. [Online]. Available: <http://dx.doi.org/10.1038/nphys2252>
- [47] D. Porras and J. I. Cirac, “Effective quantum spin systems with trapped ions,” *Phys. Rev. Lett.*, vol. 92, p. 207901, May 2004. [Online]. Available: <https://link.aps.org/doi/10.1103/PhysRevLett.92.207901>
- [48] R. Islam, E. E. Edwards, K. Kim, S. Korenblit, C. Noh, H. Carmichael, G. D. Lin, L. M. Duan, C. C. Joseph Wang, J. K. Freericks, and C. Monroe, “Onset of a quantum phase

- transition with a trapped ion quantum simulator,” *Nature Communications*, vol. 2, pp. 377 EP –, 07 2011. [Online]. Available: <http://dx.doi.org/10.1038/ncomms1374>
- [49] E. E. Edwards, S. Korenblit, K. Kim, R. Islam, M.-S. Chang, J. K. Freericks, G.-D. Lin, L.-M. Duan, and C. Monroe, “Quantum simulation and phase diagram of the transverse-field ising model with three atomic spins,” *Phys. Rev. B*, vol. 82, p. 060412, Aug 2010. [Online]. Available: <https://link.aps.org/doi/10.1103/PhysRevB.82.060412>
- [50] J. Zhang, P. W. Hess, A. Kyprianidis, P. Becker, A. Lee, J. Smith, G. Pagano, I. D. Potirniche, A. C. Potter, A. Vishwanath, N. Y. Yao, and C. Monroe, “Observation of a discrete time crystal,” *Nature*, vol. 543, pp. 217 EP –, 03 2017. [Online]. Available: <http://dx.doi.org/10.1038/nature21413>
- [51] H. Häffner, C. Roos, and R. Blatt, “Quantum computing with trapped ions,” *Physics Reports*, vol. 469, no. 4, pp. 155 – 203, 2008. [Online]. Available: <http://www.sciencedirect.com/science/article/pii/S0370157308003463>
- [52] P. Schindler, D. Nigg, T. Monz, J. T. Barreiro, E. Martinez, S. X. Wang, S. Quint, M. F. Brandl, V. Nebendahl, C. F. Roos, M. Chwalla, M. Hennrich, and R. Blatt, “A quantum information processor with trapped ions,” *New Journal of Physics*, vol. 15, no. 12, p. 123012, 2013. [Online]. Available: <http://stacks.iop.org/1367-2630/15/i=12/a=123012>
- [53] J. W. Britton, B. C. Sawyer, A. C. Keith, C. C. J. Wang, J. K. Freericks, H. Uys, M. J. Biercuk, and J. J. Bollinger, “Engineered two-dimensional ising interactions in a trapped-ion quantum

- simulator with hundreds of spins,” *Nature*, vol. 484, pp. 489 EP –, 04 2012. [Online]. Available: <http://dx.doi.org/10.1038/nature10981>
- [54] S. Debnath, N. M. Linke, C. Figgatt, K. A. Landsman, K. Wright, and C. Monroe, “Demonstration of a small programmable quantum computer with atomic qubits,” *Nature*, vol. 536, pp. 63 EP –, 08 2016. [Online]. Available: <http://dx.doi.org/10.1038/nature18648>
- [55] A. Morello, “What would you do with 1000 qubits?” *Quantum Science and Technology*, vol. 3, no. 3, p. 030201, 2018. [Online]. Available: <http://stacks.iop.org/2058-9565/3/i=3/a=030201>
- [56] T. F. Watson, S. G. J. Philips, E. Kawakami, D. R. Ward, P. Scarlino, M. Veldhorst, D. E. Savage, M. G. Lagally, M. Friesen, S. N. Coppersmith, M. A. Eriksson, and L. M. K. Vandersypen, “A programmable two-qubit quantum processor in silicon,” *Nature*, vol. 555, pp. 633 EP –, 02 2018. [Online]. Available: <http://dx.doi.org/10.1038/nature25766>
- [57] C. Noh and D. G. Angelakis, “Quantum simulations and many-body physics with light,” *Reports on Progress in Physics*, vol. 80, no. 1, p. 016401, 2017. [Online]. Available: <http://stacks.iop.org/0034-4885/80/i=1/a=016401>
- [58] D. G. Angelakis, *Quantum Simulations with Photons and Polaritons*. Springer International Publishing, 2007.
- [59] D. G. Angelakis, M. F. Santos, and S. Bose, “Photon-blockade-induced mott transitions and xy spin models in coupled cavity arrays,” *Phys. Rev. A*, vol. 76, p. 031805, Sep 2007.
- [60] M. J. Hartmann, F. G. S. L. Brandao, and M. B. Plenio, “Strongly interacting polaritons in coupled arrays of cavities,” *Nat Phys*, vol. 2, no. 12, pp. 849–855, 12 2006.

- [61] A. D. Greentree, C. Tahan, J. H. Cole, and L. C. L. Hollenberg, “Quantum phase transitions of light,” *Nat Phys*, vol. 2, no. 12, pp. 856–861, 12 2006.
- [62] J. Cho, D. G. Angelakis, and S. Bose, “Fractional quantum hall state in coupled cavities,” *Phys. Rev. Lett.*, vol. 101, p. 246809, Dec 2008. [Online]. Available: <https://link.aps.org/doi/10.1103/PhysRevLett.101.246809>
- [63] A. Nunnenkamp, J. Koch, and S. M. Girvin, “Synthetic gauge fields and homodyne transmission in jaynes–cummings lattices,” *New Journal of Physics*, vol. 13, no. 9, p. 095008, 2011.
- [64] P. Roushan, C. Neill, A. Megrant, Y. Chen, R. Babbush, R. Barends, B. Campbell, Z. Chen, B. Chiaro, A. Dunsworth, A. Fowler, E. Jeffrey, J. Kelly, E. Lucero, J. Mutus, P. J. J. O’Malley, M. Neeley, C. Quintana, D. Sank, A. Vainsencher, J. Wenner, T. White, E. Kapit, H. Neven, and J. Martinis, “Chiral ground-state currents of interacting photons in a synthetic magnetic field,” *Nature Physics*, vol. 13, pp. 146 EP –, 10 2016. [Online]. Available: <http://dx.doi.org/10.1038/nphys3930>
- [65] M. J. Hartmann, F. G. S. L. Brandão, and M. B. Plenio, “Effective spin systems in coupled microcavities,” *Phys. Rev. Lett.*, vol. 99, p. 160501, Oct 2007. [Online]. Available: <https://link.aps.org/doi/10.1103/PhysRevLett.99.160501>
- [66] A. Kay and D. G. Angelakis, “Reproducing spin lattice models in strongly coupled atom-cavity systems,” *EPL (Europhysics Letters)*, vol. 84, no. 2, p. 20001, 2008. [Online]. Available: <http://stacks.iop.org/0295-5075/84/i=2/a=20001>

- [67] P. B. Li, Y. Gu, Q. H. Gong, and G. C. Guo, “Generation of ising interaction and cluster states in a one-dimensional coupled resonator waveguide,” *The European Physical Journal D*, vol. 55, no. 1, p. 205, Jun 2009. [Online]. Available: <https://doi.org/10.1140/epjd/e2009-00188-3>
- [68] S. Sarkar, “Quantum field theoretical study of an effective spin model in coupled optical cavity arrays,” *Physica B: Condensed Matter*, vol. 407, no. 1, pp. 44 – 48, 2012. [Online]. Available: <http://www.sciencedirect.com/science/article/pii/S0921452611009483>
- [69] J. Tangpanitanon, V. M. Bastidas, S. Al-Assam, P. Roushan, D. Jaksch, and D. G. Angelakis, “Topological pumping of photons in nonlinear resonator arrays,” *Phys. Rev. Lett.*, vol. 117, p. 213603, Nov 2016. [Online]. Available: <https://link.aps.org/doi/10.1103/PhysRevLett.117.213603>
- [70] P. Roushan, C. Neill, J. Tangpanitanon, V. M. Bastidas, A. Megrant, R. Barends, Y. Chen, Z. Chen, B. Chiaro, A. Dunsworth, A. Fowler, B. Foxen, M. Giustina, E. Jeffrey, J. Kelly, E. Lucero, J. Mutus, M. Neeley, C. Quintana, D. Sank, A. Vainsencher, J. Wenner, T. White, H. Neven, D. G. Angelakis, and J. Martinis, “Spectroscopic signatures of localization with interacting photons in superconducting qubits,” *Science*, vol. 358, no. 6367, pp. 1175–1179, 2017. [Online]. Available: <http://science.sciencemag.org/content/358/6367/1175>
- [71] V. V. Albert and L. Jiang, “Symmetries and conserved quantities in lindblad master equations,” *Phys. Rev. A*, vol. 89, p. 022118, Feb 2014. [Online]. Available: <https://link.aps.org/doi/10.1103/PhysRevA.89.022118>
- [72] I. Carusotto, D. Gerace, H. E. Tureci, S. De Liberato, C. Ciuti, and A. Imamoglu, “Fermionized photons in an

- array of driven dissipative nonlinear cavities,” *Phys. Rev. Lett.*, vol. 103, p. 033601, Jul 2009. [Online]. Available: <http://link.aps.org/doi/10.1103/PhysRevLett.103.033601>
- [73] M. J. Hartmann, “Polariton crystallization in driven arrays of lossy nonlinear resonators,” *Phys. Rev. Lett.*, vol. 104, p. 113601, Mar 2010. [Online]. Available: <http://link.aps.org/doi/10.1103/PhysRevLett.104.113601>
- [74] T. Grujic, S. R. Clark, D. Jaksch, and D. G. Angelakis, “Non-equilibrium many-body effects in driven nonlinear resonator arrays,” *New Journal of Physics*, vol. 14, no. 10, p. 103025, 2012. [Online]. Available: <http://stacks.iop.org/1367-2630/14/i=10/a=103025>
- [75] R. O. Umucalilar and I. Carusotto, “Fractional quantum hall states of photons in an array of dissipative coupled cavities,” *Phys. Rev. Lett.*, vol. 108, p. 206809, May 2012. [Online]. Available: <http://link.aps.org/doi/10.1103/PhysRevLett.108.206809>
- [76] C.-E. Bardyn and A. Imamoglu, “Majorana-like modes of light in a one-dimensional array of nonlinear cavities,” *Phys. Rev. Lett.*, vol. 109, p. 253606, Dec 2012. [Online]. Available: <http://link.aps.org/doi/10.1103/PhysRevLett.109.253606>
- [77] J. Jin, D. Rossini, R. Fazio, M. Leib, and M. J. Hartmann, “Photon solid phases in driven arrays of nonlinearly coupled cavities,” *Phys. Rev. Lett.*, vol. 110, p. 163605, Apr 2013.
- [78] E. M. Kessler, G. Giedke, A. Imamoglu, S. F. Yelin, M. D. Lukin, and J. I. Cirac, “Dissipative phase transition in a central spin system,” *Phys. Rev. A*, vol. 86, p. 012116, Jul 2012. [Online]. Available: <https://link.aps.org/doi/10.1103/PhysRevA.86.012116>

- [79] H. Wilming, M. J. Kastoryano, A. H. Werner, and J. Eisert, “Emergence of spontaneous symmetry breaking in dissipative lattice systems,” *Journal of Mathematical Physics*, vol. 58, no. 3, p. 033302, 2017.
- [80] M. Fitzpatrick, N. M. Sundaresan, A. C. Y. Li, J. Koch, and A. A. Houck, “Observation of a dissipative phase transition in a one-dimensional circuit qed lattice,” *Phys. Rev. X*, vol. 7, p. 011016, Feb 2017. [Online]. Available: <https://link.aps.org/doi/10.1103/PhysRevX.7.011016>
- [81] I. Carusotto and C. Ciuti, “Quantum fluids of light,” *Rev. Mod. Phys.*, vol. 85, pp. 299–366, Feb 2013. [Online]. Available: <https://link.aps.org/doi/10.1103/RevModPhys.85.299>
- [82] I. Carusotto, T. Volz, and A. Imamoglu, “Feshbach blockade: Single-photon nonlinear optics using resonantly enhanced cavity polariton scattering from biexciton states,” *EPL (Europhysics Letters)*, vol. 90, no. 3, p. 37001, 2010. [Online]. Available: <http://stacks.iop.org/0295-5075/90/i=3/a=37001>
- [83] J. Kasprzak, M. Richard, S. Kundermann, A. Baas, P. Jeambrun, J. M. J. Keeling, F. M. Marchetti, M. H. Szymańska, R. André, J. L. Staehli, V. Savona, P. B. Littlewood, B. Deveaud, and L. S. Dang, “Bose–einstein condensation of exciton polaritons,” *Nature*, vol. 443, pp. 409 EP –, 09 2006. [Online]. Available: <http://dx.doi.org/10.1038/nature05131>
- [84] J. D. Plumhof, T. Stöferle, L. Mai, U. Scherf, and R. F. Mahrt, “Room-temperature bose–einstein condensation of cavity exciton–polaritons in a polymer,” *Nature Materials*, vol. 13, pp. 247 EP –, 12 2013. [Online]. Available: <http://dx.doi.org/10.1038/nmat3825>

- [85] K. G. Lagoudakis, M. Wouters, M. Richard, A. Baas, I. Carusotto, R. André, L. S. Dang, and B. Deveaud-Plédran, “Quantized vortices in an exciton–polariton condensate,” *Nature Physics*, vol. 4, pp. 706 EP –, 08 2008. [Online]. Available: <http://dx.doi.org/10.1038/nphys1051>
- [86] A. Amo, J. Lefrère, S. Pigeon, C. Adrados, C. Ciuti, I. Carusotto, R. Houdré, E. Giacobino, and A. Bramati, “Superfluidity of polaritons in semiconductor microcavities,” *Nature Physics*, vol. 5, pp. 805 EP –, 09 2009. [Online]. Available: <http://dx.doi.org/10.1038/nphys1364>
- [87] D. L. Underwood, W. E. Shanks, J. Koch, and A. A. Houck, “Low-disorder microwave cavity lattices for quantum simulation with photons,” *Phys. Rev. A*, vol. 86, p. 023837, Aug 2012. [Online]. Available: <https://link.aps.org/doi/10.1103/PhysRevA.86.023837>
- [88] J. Q. You and F. Nori, “Superconducting circuits and quantum information,” *Physics Today*, 2005.
- [89] A. Wallraff, D. I. Schuster, A. Blais, L. Frunzio, R. S. Huang, J. Majer, S. Kumar, S. M. Girvin, and R. J. Schoelkopf, “Strong coupling of a single photon to a superconducting qubit using circuit quantum electrodynamics,” *Nature*, vol. 431, pp. 162 EP –, 09 2004. [Online]. Available: <http://dx.doi.org/10.1038/nature02851>
- [90] F. Yoshihara, T. Fuse, S. Ashhab, K. Kakuyanagi, S. Saito, and K. Semba, “Superconducting qubit–oscillator circuit beyond the ultrastrong-coupling regime,” *Nature Physics*, vol. 13, pp. 44 EP –, 10 2016. [Online]. Available: <http://dx.doi.org/10.1038/nphys3906>
- [91] A. Kandala, A. Mezzacapo, K. Temme, M. Takita, M. Brink, J. M. Chow, and J. M. Gambetta, “Hardware-efficient variational

- quantum eigensolver for small molecules and quantum magnets,” *Nature*, vol. 549, pp. 242 EP –, 09 2017. [Online]. Available: <http://dx.doi.org/10.1038/nature23879>
- [92] J. S. Otterbach, R. Manenti, N. Alidoust, A. Bestwick, M. Block, B. Bloom, S. Caldwell, N. Didier, E. Schuyler Fried, S. Hong, P. Karalekas, C. B. Osborn, A. Papageorge, E. C. Peterson, G. Prawiroatmodjo, N. Rubin, C. A. Ryan, D. Scarabelli, M. Scheer, E. A. Sete, P. Sivarajah, R. S. Smith, A. Staley, N. Tezak, W. J. Zeng, A. Hudson, B. R. Johnson, M. Reagor, M. P. da Silva, and C. Rigetti, “Unsupervised Machine Learning on a Hybrid Quantum Computer,” *ArXiv e-prints*, Dec. 2017.
- [93] S. Sachdev, *Quantum Phase Transitions*, 2nd ed. Cambridge, UK: Cambridge University Press, Apr 2011. [Online]. Available: <http://www.cambridge.org/9780521514682>
- [94] “Electron correlations in narrow energy bands,” *Proceedings of the Royal Society of London A: Mathematical, Physical and Engineering Sciences*, vol. 276, no. 1365, pp. 238–257, 1963. [Online]. Available: <http://rspa.royalsocietypublishing.org/content/276/1365/238>
- [95] H. A. Gersch and G. C. Knollman, “Quantum cell model for bosons,” *Phys. Rev.*, vol. 129, pp. 959–967, Jan 1963. [Online]. Available: <https://link.aps.org/doi/10.1103/PhysRev.129.959>
- [96] M. P. A. Fisher, P. B. Weichman, G. Grinstein, and D. S. Fisher, “Boson localization and the superfluid-insulator transition,” *Phys. Rev. B*, vol. 40, pp. 546–570, Jul 1989. [Online]. Available: <https://link.aps.org/doi/10.1103/PhysRevB.40.546>
- [97] S. Ejima, H. Fehske, and F. Gebhard, “Dynamic properties of the one-dimensional bose-hubbard model,” *EPL (Europhysics*

- Letters*), vol. 93, no. 3, p. 30002, 2011. [Online]. Available: <http://stacks.iop.org/0295-5075/93/i=3/a=30002>
- [98] R. Boyd, *Nonlinear Optics*. Elsevier, 2008.
- [99] B. Darquié, M. P. A. Jones, J. Dingjan, J. Beugnon, S. Bergamini, Y. Sortais, G. Messin, A. Browaeys, and P. Grangier, “Controlled single-photon emission from a single trapped two-level atom,” *Science*, vol. 309, no. 5733, pp. 454–456, 2005. [Online]. Available: <http://science.sciencemag.org/content/309/5733/454>
- [100] G. Wrigge, I. Gerhardt, J. Hwang, G. Zumofen, and V. Sandoghdar, “Efficient coupling of photons to a single molecule and the observation of its resonance fluorescence,” *Nature Physics*, vol. 4, pp. 60 EP –, 12 2007. [Online]. Available: <http://dx.doi.org/10.1038/nphys812>
- [101] M. K. Tey, Z. Chen, S. A. Aljunid, B. Chng, F. Huber, G. Maslennikov, and C. Kurtsiefer, “Strong interaction between light and a single trapped atom without the need for a cavity,” *Nature Physics*, vol. 4, pp. 924 EP –, 10 2008. [Online]. Available: <http://dx.doi.org/10.1038/nphys1096>
- [102] G. Hétet, L. Slodička, M. Hennrich, and R. Blatt, “Single atom as a mirror of an optical cavity,” *Phys. Rev. Lett.*, vol. 107, p. 133002, Sep 2011. [Online]. Available: <https://link.aps.org/doi/10.1103/PhysRevLett.107.133002>
- [103] D. Walls and G. J. Milburn, *Quantum Optics*. Springer International Publishing, 2008.
- [104] B. W. Shore and P. L. Knight, “The jaynes-cummings model,” *Journal of Modern Optics*, vol. 40, no. 7, pp. 1195–1238, 1993.
- [105] P. Goy, J. M. Raimond, M. Gross, and S. Haroche, “Observation of cavity-enhanced single-atom spontaneous emission,” *Phys. Rev.*

- Lett.*, vol. 50, pp. 1903–1906, Jun 1983. [Online]. Available: <https://link.aps.org/doi/10.1103/PhysRevLett.50.1903>
- [106] R. G. Hulet, E. S. Hilfer, and D. Kleppner, “Inhibited spontaneous emission by a rydberg atom,” *Phys. Rev. Lett.*, vol. 55, pp. 2137–2140, Nov 1985. [Online]. Available: <https://link.aps.org/doi/10.1103/PhysRevLett.55.2137>
- [107] W. Jhe, A. Anderson, E. A. Hinds, D. Meschede, L. Moi, and S. Haroche, “Suppression of spontaneous decay at optical frequencies: Test of vacuum-field anisotropy in confined space,” *Phys. Rev. Lett.*, vol. 58, pp. 666–669, Feb 1987. [Online]. Available: <https://link.aps.org/doi/10.1103/PhysRevLett.58.666>
- [108] R. J. Thompson, G. Rempe, and H. J. Kimble, “Observation of normal-mode splitting for an atom in an optical cavity,” *Phys. Rev. Lett.*, vol. 68, pp. 1132–1135, Feb 1992. [Online]. Available: <https://link.aps.org/doi/10.1103/PhysRevLett.68.1132>
- [109] M. Brune, F. Schmidt-Kaler, A. Maali, J. Dreyer, E. Hagley, J. M. Raimond, and S. Haroche, “Quantum rabi oscillation: A direct test of field quantization in a cavity,” *Phys. Rev. Lett.*, vol. 76, pp. 1800–1803, Mar 1996. [Online]. Available: <https://link.aps.org/doi/10.1103/PhysRevLett.76.1800>
- [110] Q. A. Turchette, C. J. Hood, W. Lange, H. Mabuchi, and H. J. Kimble, “Measurement of conditional phase shifts for quantum logic,” *Phys. Rev. Lett.*, vol. 75, pp. 4710–4713, Dec 1995. [Online]. Available: <https://link.aps.org/doi/10.1103/PhysRevLett.75.4710>
- [111] E. Hagley, X. Maître, G. Nogues, C. Wunderlich, M. Brune, J. M. Raimond, and S. Haroche, “Generation of einstein-podolsky-rosen

- pairs of atoms,” *Phys. Rev. Lett.*, vol. 79, pp. 1–5, Jul 1997. [Online]. Available: <https://link.aps.org/doi/10.1103/PhysRevLett.79.1>
- [112] D. V. Averin and K. K. Likharev, “Coulomb blockade of single-electron tunneling, and coherent oscillations in small tunnel junctions,” *Journal of Low Temperature Physics*, vol. 62, no. 3, pp. 345–373, Feb 1986. [Online]. Available: <https://doi.org/10.1007/BF00683469>
- [113] K. M. Birnbaum, A. Boca, R. Miller, A. D. Boozer, T. E. Northup, and H. J. Kimble, “Photon blockade in an optical cavity with one trapped atom,” *Nature*, vol. 436, no. 7047, pp. 87–90, 07 2005. [Online]. Available: <http://dx.doi.org/10.1038/nature03804>
- [114] H. Schmidt and A. Imamoglu, “Giant kerr nonlinearities obtained by electromagnetically induced transparency,” *Opt. Lett.*, vol. 21, no. 23, pp. 1936–1938, Dec 1996. [Online]. Available: <http://ol.osa.org/abstract.cfm?URI=ol-21-23-1936>
- [115] T. Peyronel, O. Firstenberg, Q.-Y. Liang, S. Hofferberth, A. V. Gorshkov, T. Pohl, M. D. Lukin, and V. Vuletić, “Quantum nonlinear optics with single photons enabled by strongly interacting atoms,” *Nature*, vol. 488, pp. 57 EP –, 07 2012. [Online]. Available: <http://dx.doi.org/10.1038/nature11361>
- [116] O. Firstenberg, T. Peyronel, Q.-Y. Liang, A. V. Gorshkov, M. D. Lukin, and V. Vuletić, “Attractive photons in a quantum nonlinear medium,” *Nature*, vol. 502, pp. 71 EP –, 09 2013. [Online]. Available: <https://doi.org/10.1038/nature12512>
- [117] M. Hafezi, P. Adhikari, and J. M. Taylor, “Chemical potential for light by parametric coupling,” *Phys. Rev. B*, vol. 92, p. 174305,

- Nov 2015. [Online]. Available: <https://link.aps.org/doi/10.1103/PhysRevB.92.174305>
- [118] D. Rossini and R. Fazio, “Mott-insulating and glassy phases of polaritons in 1d arrays of coupled cavities,” *Phys. Rev. Lett.*, vol. 99, p. 186401, Oct 2007. [Online]. Available: <https://link.aps.org/doi/10.1103/PhysRevLett.99.186401>
- [119] A. Mering, M. Fleischhauer, P. A. Ivanov, and K. Singer, “Analytic approximations to the phase diagram of the jaynes-cummings-hubbard model,” *Phys. Rev. A*, vol. 80, p. 053821, Nov 2009. [Online]. Available: <https://link.aps.org/doi/10.1103/PhysRevA.80.053821>
- [120] M. I. Makin, J. H. Cole, C. D. Hill, A. D. Greentree, and L. C. L. Hollenberg, “Time evolution of the one-dimensional jaynes-cummings-hubbard hamiltonian,” *Phys. Rev. A*, vol. 80, p. 043842, Oct 2009. [Online]. Available: <https://link.aps.org/doi/10.1103/PhysRevA.80.043842>
- [121] P. Phipps, H. G. Evertz, and M. Hohenadler, “Excitation spectra of strongly correlated lattice bosons and polaritons,” *Phys. Rev. A*, vol. 80, p. 033612, Sep 2009. [Online]. Available: <https://link.aps.org/doi/10.1103/PhysRevA.80.033612>
- [122] R. Chakrabarti and G. Sreeumari, “Propagation of single-excitation quantum states through jaynes-cummings-hubbard arrays,” *Journal of Physics B: Atomic, Molecular and Optical Physics*, vol. 44, no. 11, p. 115505, 2011. [Online]. Available: <http://stacks.iop.org/0953-4075/44/i=11/a=115505>
- [123] M. X. Huo, Y. Li, Z. Song, and C. P. Sun, “Atomic entanglement versus visibility of photon interference for quantum criticality of a

- hybrid system,” *Phys. Rev. A*, vol. 77, p. 022103, Feb 2008. [Online]. Available: <https://link.aps.org/doi/10.1103/PhysRevA.77.022103>
- [124] E. K. Irish, “Ground-state entanglement in a coupled-cavity model,” *Phys. Rev. A*, vol. 80, p. 043825, Oct 2009. [Online]. Available: <https://link.aps.org/doi/10.1103/PhysRevA.80.043825>
- [125] M. Hohenadler, M. Aichhorn, S. Schmidt, and L. Pollet, “Dynamical critical exponent of the jaynes-cummings-hubbard model,” *Phys. Rev. A*, vol. 84, p. 041608, Oct 2011. [Online]. Available: <https://link.aps.org/doi/10.1103/PhysRevA.84.041608>
- [126] S. Bose, D. G. Angelakis, and D. Burgarth, “Transfer of a polaritonic qubit through a coupled cavity array,” *Journal of Modern Optics*, vol. 54, no. 13-15, pp. 2307–2314, 2007.
- [127] F. M. Hu, L. Zhou, T. Shi, and C. P. Sun, “Coupled cavity qed for coherent control of photon transmission: Green-function approach for hybrid systems with two-level doping,” *Phys. Rev. A*, vol. 76, p. 013819, Jul 2007. [Online]. Available: <https://link.aps.org/doi/10.1103/PhysRevA.76.013819>
- [128] T. Grujic, S. R. Clark, D. Jaksch, and D. G. Angelakis, “Non-equilibrium many-body effects in driven nonlinear resonator arrays,” *New Journal of Physics*, vol. 14, no. 10, p. 103025, 2012. [Online]. Available: <http://stacks.iop.org/1367-2630/14/i=10/a=103025>
- [129] C. Joshi, F. Nissen, and J. Keeling, “Quantum correlations in the one-dimensional driven dissipative xy model,” *Phys. Rev. A*, vol. 88, p. 063835, Dec 2013. [Online]. Available: <http://link.aps.org/doi/10.1103/PhysRevA.88.063835>
- [130] T. F. See, V. M. Bastidas, J. Tangpanitanon, and D. G. Angelakis, “Strongly correlated photon transport in nonlinear photonic

lattice with disorder: Probing signatures of the localization transition,” *ArXiv e-prints*, Jul. 2018.

- [131] J. J. Mendoza-Arenas, S. R. Clark, S. Felicetti, G. Romero, E. Solano, D. G. Angelakis, and D. Jaksch, “Beyond mean-field bistability in driven-dissipative lattices: Bunching-antibunching transition and quantum simulation,” *Phys. Rev. A*, vol. 93, p. 023821, Feb 2016. [Online]. Available: <https://link.aps.org/doi/10.1103/PhysRevA.93.023821>
- [132] B. Josephson, “Possible new effects in superconductive tunnelling,” *Physics Letters*, vol. 1, no. 7, pp. 251 – 253, 1962. [Online]. Available: <http://www.sciencedirect.com/science/article/pii/0031916362913690>
- [133] V. Bouchiat, D. Vion, P. Joyez, D. Esteve, and M. H. Devoret, “Quantum coherence with a single cooper pair,” *Physica Scripta*, vol. 1998, no. T76, p. 165, 1998. [Online]. Available: <http://stacks.iop.org/1402-4896/1998/i=T76/a=024>
- [134] Y. Nakamura, Y. A. Pashkin, and J. S. Tsai, “Coherent control of macroscopic quantum states in a single-cooper-pair box,” *Nature*, vol. 398, pp. 786 EP –, 04 1999. [Online]. Available: <http://dx.doi.org/10.1038/19718>
- [135] M. H. Devoret, “Quantum fluctuations in electrical circuits,” *Les Houches Session LXIII, Quantum Fluctuations*, 1995.
- [136] M. Leib, F. Deppe, A. Marx, R. Gross, and M. J. Hartmann, “Networks of nonlinear superconducting transmission line resonators,” *New Journal of Physics*, vol. 14, no. 7, p. 075024, 2012. [Online]. Available: <http://stacks.iop.org/1367-2630/14/i=7/a=075024>

- [137] V. V. Mikhailov, “Normal ordering and generalised stirling numbers,” *Journal of Physics A: Mathematical and General*, vol. 18, no. 2, p. 231, 1985. [Online]. Available: <http://stacks.iop.org/0305-4470/18/i=2/a=012>
- [138] A. A. Houck, J. Koch, M. H. Devoret, S. M. Girvin, and R. J. Schoelkopf, “Life after charge noise: recent results with transmon qubits,” *Quantum Information Processing*, vol. 8, no. 2, pp. 105–115, Jun 2009. [Online]. Available: <https://doi.org/10.1007/s11128-009-0100-6>
- [139] H. Paik, D. I. Schuster, L. S. Bishop, G. Kirchmair, G. Catelani, A. P. Sears, B. R. Johnson, M. J. Reagor, L. Frunzio, L. I. Glazman, S. M. Girvin, M. H. Devoret, and R. J. Schoelkopf, “Observation of high coherence in josephson junction qubits measured in a three-dimensional circuit qed architecture,” *Phys. Rev. Lett.*, vol. 107, p. 240501, Dec 2011. [Online]. Available: <https://link.aps.org/doi/10.1103/PhysRevLett.107.240501>
- [140] T. P. Orlando, J. E. Mooij, L. Tian, C. H. van der Wal, L. S. Levitov, S. Lloyd, and J. J. Mazo, “Superconducting persistent-current qubit,” *Phys. Rev. B*, vol. 60, pp. 15 398–15 413, Dec 1999. [Online]. Available: <https://link.aps.org/doi/10.1103/PhysRevB.60.15398>
- [141] J. R. Friedman, V. Patel, W. Chen, S. K. Tolpygo, and J. E. Lukens, “Quantum superposition of distinct macroscopic states,” *Nature*, vol. 406, pp. 43 EP –, 07 2000. [Online]. Available: <http://dx.doi.org/10.1038/35017505>
- [142] J. M. Martinis, S. Nam, J. Aumentado, and C. Urbina, “Rabi oscillations in a large josephson-junction qubit,” *Phys. Rev. Lett.*, vol. 89, p. 117901, Aug 2002. [Online]. Available: <https://link.aps.org/doi/10.1103/PhysRevLett.89.117901>

- [143] J. M. Martinis, “Superconducting phase qubits,” *Quantum Information Processing*, vol. 8, no. 2, pp. 81–103, Jun 2009. [Online]. Available: <https://doi.org/10.1007/s11128-009-0105-1>
- [144] C. H. van der Wal, A. C. J. ter Haar, F. K. Wilhelm, R. N. Schouten, C. J. P. M. Harmans, T. P. Orlando, S. Lloyd, and J. E. Mooij, “Quantum superposition of macroscopic persistent-current states,” *Science*, vol. 290, no. 5492, pp. 773–777, 2000. [Online]. Available: <http://science.sciencemag.org/content/290/5492/773>
- [145] S. Boixo, T. F. Rønnow, S. V. Isakov, Z. Wang, D. Wecker, D. A. Lidar, J. M. Martinis, and M. Troyer, “Evidence for quantum annealing with more than one hundred qubits,” *Nature Physics*, vol. 10, pp. 218 EP –, 02 2014. [Online]. Available: <http://dx.doi.org/10.1038/nphys2900>
- [146] M. H. Devoret and R. J. Schoelkopf, “Superconducting circuits for quantum information: An outlook,” *Science*, vol. 339, no. 6124, pp. 1169–1174, 2013. [Online]. Available: <http://science.sciencemag.org/content/339/6124/1169>
- [147] M. A. Sillanpaa, J. I. Park, and R. W. Simmonds, “Coherent quantum state storage and transfer between two phase qubits via a resonant cavity,” *Nature*, vol. 449, no. 7161, pp. 438–442, 09 2007. [Online]. Available: <http://dx.doi.org/10.1038/nature06124>
- [148] J. Majer, J. M. Chow, J. M. Gambetta, J. Koch, B. R. Johnson, J. A. Schreier, L. Frunzio, D. I. Schuster, A. A. Houck, A. Wallraff, A. Blais, M. H. Devoret, S. M. Girvin, and R. J. Schoelkopf, “Coupling superconducting qubits via a cavity bus,” *Nature*, vol. 449, no. 7161, pp. 443–447, 09 2007. [Online]. Available: <http://dx.doi.org/10.1038/nature06184>

- [149] Y. Chen, C. Neill, P. Roushan, N. Leung, M. Fang, R. Barends, J. Kelly, B. Campbell, Z. Chen, B. Chiaro, A. Dunsworth, E. Jeffrey, A. Megrant, J. Y. Mutus, P. J. J. O’Malley, C. M. Quintana, D. Sank, A. Vainsencher, J. Wenner, T. C. White, M. R. Geller, A. N. Cleland, and J. M. Martinis, “Qubit architecture with high coherence and fast tunable coupling,” *Phys. Rev. Lett.*, vol. 113, p. 220502, Nov 2014. [Online]. Available: <https://link.aps.org/doi/10.1103/PhysRevLett.113.220502>
- [150] M. R. Geller, E. Donate, Y. Chen, M. T. Fang, N. Leung, C. Neill, P. Roushan, and J. M. Martinis, “Tunable coupler for superconducting qubits: Perturbative nonlinear model,” *Phys. Rev. A*, vol. 92, p. 012320, Jul 2015. [Online]. Available: <https://link.aps.org/doi/10.1103/PhysRevA.92.012320>
- [151] D. Kafri, C. Quintana, Y. Chen, A. Shabani, J. M. Martinis, and H. Neven, “Tunable inductive coupling of superconducting qubits in the strongly nonlinear regime,” *Phys. Rev. A*, vol. 95, p. 052333, May 2017. [Online]. Available: <https://link.aps.org/doi/10.1103/PhysRevA.95.052333>
- [152] C. Neill, P. Roushan, K. Kechedzhi, S. Boixo, S. V. Isakov, V. Smelyanskiy, A. Megrant, B. Chiaro, A. Dunsworth, K. Arya, R. Barends, B. Burkett, Y. Chen, Z. Chen, A. Fowler, B. Foxen, M. Giustina, R. Graff, E. Jeffrey, T. Huang, J. Kelly, P. Klimov, E. Lucero, J. Mutus, M. Neeley, C. Quintana, D. Sank, A. Vainsencher, J. Wenner, T. C. White, H. Neven, and J. M. Martinis, “A blueprint for demonstrating quantum supremacy with superconducting qubits,” *Science*, vol. 360, no. 6385, pp. 195–199, 2018. [Online]. Available: <http://science.sciencemag.org/content/360/6385/195>

- [153] P. W. Anderson, “Absence of diffusion in certain random lattices,” *Phys. Rev.*, vol. 109, pp. 1492–1505, Mar 1958. [Online]. Available: <https://link.aps.org/doi/10.1103/PhysRev.109.1492>
- [154] D. Basko, I. Aleiner, and B. Altshuler, “Metal–insulator transition in a weakly interacting many-electron system with localized single-particle states,” *Annals of Physics*, vol. 321, no. 5, pp. 1126 – 1205, 2006. [Online]. Available: <http://www.sciencedirect.com/science/article/pii/S0003491605002630>
- [155] E. Altman and R. Vosk, “Universal dynamics and renormalization in many-body-localized systems,” *Annual Review of Condensed Matter Physics*, vol. 6, no. 1, pp. 383–409, 2015. [Online]. Available: <https://doi.org/10.1146/annurev-conmatphys-031214-014701>
- [156] N. Y. Yao, C. R. Laumann, S. Gopalakrishnan, M. Knap, M. Müller, E. A. Demler, and M. D. Lukin, “Many-body localization in dipolar systems,” *Phys. Rev. Lett.*, vol. 113, p. 243002, Dec 2014. [Online]. Available: <https://link.aps.org/doi/10.1103/PhysRevLett.113.243002>
- [157] A. Pal and D. A. Huse, “Many-body localization phase transition,” *Phys. Rev. B*, vol. 82, p. 174411, Nov 2010. [Online]. Available: <https://link.aps.org/doi/10.1103/PhysRevB.82.174411>
- [158] A. Chandran, V. Khemani, C. R. Laumann, and S. L. Sondhi, “Many-body localization and symmetry-protected topological order,” *Phys. Rev. B*, vol. 89, p. 144201, Apr 2014. [Online]. Available: <https://link.aps.org/doi/10.1103/PhysRevB.89.144201>
- [159] M. Serbyn, M. Knap, S. Gopalakrishnan, Z. Papić, N. Y. Yao, C. R. Laumann, D. A. Abanin, M. D. Lukin, and E. A. Demler, “Interferometric probes of many-body localization,” *Phys.*

- Rev. Lett.*, vol. 113, p. 147204, Oct 2014. [Online]. Available: <https://link.aps.org/doi/10.1103/PhysRevLett.113.147204>
- [160] J. A. Kjäll, J. H. Bardarson, and F. Pollmann, “Many-body localization in a disordered quantum ising chain,” *Phys. Rev. Lett.*, vol. 113, p. 107204, Sep 2014. [Online]. Available: <https://link.aps.org/doi/10.1103/PhysRevLett.113.107204>
- [161] M. Serbyn, Z. Papić, and D. A. Abanin, “Criterion for many-body localization-delocalization phase transition,” *Phys. Rev. X*, vol. 5, p. 041047, Dec 2015. [Online]. Available: <https://link.aps.org/doi/10.1103/PhysRevX.5.041047>
- [162] Y. Bahri, R. Vosk, E. Altman, and A. Vishwanath, “Localization and topology protected quantum coherence at the edge of hot matter,” *Nature Communications*, vol. 6, pp. 7341 EP –, 07 2015. [Online]. Available: <http://dx.doi.org/10.1038/ncomms8341>
- [163] J. Z. Imbrie, “Diagonalization and many-body localization for a disordered quantum spin chain,” *Phys. Rev. Lett.*, vol. 117, p. 027201, Jul 2016. [Online]. Available: <https://link.aps.org/doi/10.1103/PhysRevLett.117.027201>
- [164] F. Iemini, A. Russomanno, D. Rossini, A. Scardicchio, and R. Fazio, “Signatures of many-body localization in the dynamics of two-site entanglement,” *Phys. Rev. B*, vol. 94, p. 214206, Dec 2016. [Online]. Available: <https://link.aps.org/doi/10.1103/PhysRevB.94.214206>
- [165] M. Schreiber, S. S. Hodgman, P. Bordia, H. P. Lüschen, M. H. Fischer, R. Vosk, E. Altman, U. Schneider, and I. Bloch, “Observation of many-body localization of interacting fermions in a quasirandom optical lattice,” *Science*, vol. 349, no. 6250, pp.

- 842–845, 2015. [Online]. Available: <http://science.sciencemag.org/content/349/6250/842>
- [166] A. M. Kaufman, M. E. Tai, A. Lukin, M. Rispoli, R. Schittko, P. M. Preiss, and M. Greiner, “Quantum thermalization through entanglement in an isolated many-body system,” *Science*, vol. 353, no. 6301, pp. 794–800, 2016. [Online]. Available: <http://science.sciencemag.org/content/353/6301/794>
- [167] J. Smith, A. Lee, P. Richerme, B. Neyenhuis, P. W. Hess, P. Hauke, M. Heyl, D. A. Huse, and C. Monroe, “Many-body localization in a quantum simulator with programmable random disorder,” *Nature Physics*, vol. 12, pp. 907 EP –, 06 2016. [Online]. Available: <http://dx.doi.org/10.1038/nphys3783>
- [168] K. Xu, J.-J. Chen, Y. Zeng, Y.-R. Zhang, C. Song, W. Liu, Q. Guo, P. Zhang, D. Xu, H. Deng, K. Huang, H. Wang, X. Zhu, D. Zheng, and H. Fan, “Emulating many-body localization with a superconducting quantum processor,” *Phys. Rev. Lett.*, vol. 120, p. 050507, Feb 2018. [Online]. Available: <https://link.aps.org/doi/10.1103/PhysRevLett.120.050507>
- [169] P. Jurcevic, P. Hauke, C. Maier, C. Hempel, B. P. Lanyon, R. Blatt, and C. F. Roos, “Spectroscopy of interacting quasiparticles in trapped ions,” *Phys. Rev. Lett.*, vol. 115, p. 100501, Sep 2015. [Online]. Available: <https://link.aps.org/doi/10.1103/PhysRevLett.115.100501>
- [170] C. Senko, J. Smith, P. Richerme, A. Lee, W. C. Campbell, and C. Monroe, “Coherent imaging spectroscopy of a quantum many-body spin system,” *Science*, vol. 345, no. 6195, pp. 430–433, 2014. [Online]. Available: <http://science.sciencemag.org/content/345/6195/430>

- [171] Y. E. Kraus, Y. Lahini, Z. Ringel, M. Verbin, and O. Zilberberg, “Topological States and Adiabatic Pumping in Quasicrystals,” *Phys. Rev. Lett.*, vol. 109, p. 106402, Sep 2012. [Online]. Available: <http://link.aps.org/doi/10.1103/PhysRevLett.109.106402>
- [172] D. R. Hofstadter, “Energy levels and wave functions of bloch electrons in rational and irrational magnetic fields,” *Phys. Rev. B*, vol. 14, pp. 2239–2249, Sep 1976. [Online]. Available: <https://link.aps.org/doi/10.1103/PhysRevB.14.2239>
- [173] L. A. Ponomarenko, R. V. Gorbachev, G. L. Yu, D. C. Elias, R. Jalil, A. A. Patel, A. Mishchenko, A. S. Mayorov, C. R. Woods, J. R. Wallbank, M. Mucha-Kruczynski, B. A. Piot, M. Potemski, I. V. Grigorieva, K. S. Novoselov, F. Guinea, V. I. Fal’ko, and A. K. Geim, “Cloning of dirac fermions in graphene superlattices,” *Nature*, vol. 497, pp. 594 EP –, 05 2013. [Online]. Available: <http://dx.doi.org/10.1038/nature12187>
- [174] C. R. Dean, L. Wang, P. Maher, C. Forsythe, F. Ghahari, Y. Gao, J. Katoch, M. Ishigami, P. Moon, M. Koshino, T. Taniguchi, K. Watanabe, K. L. Shepard, J. Hone, and P. Kim, “Hofstadter’s butterfly and the fractal quantum hall effect in moirésuperlattices,” *Nature*, vol. 497, pp. 598 EP –, 05 2013. [Online]. Available: <http://dx.doi.org/10.1038/nature12186>
- [175] B. Hunt, J. D. Sanchez-Yamagishi, A. F. Young, M. Yankowitz, B. J. LeRoy, K. Watanabe, T. Taniguchi, P. Moon, M. Koshino, P. Jarillo-Herrero, and R. C. Ashoori, “Massive dirac fermions and hofstadter butterfly in a van der waals heterostructure,” *Science*, vol. 340, no. 6139, pp. 1427–1430, 2013. [Online]. Available: <http://science.sciencemag.org/content/340/6139/1427>

- [176] H. Miyake, G. A. Siviloglou, C. J. Kennedy, W. C. Burton, and W. Ketterle, “Realizing the harper hamiltonian with laser-assisted tunneling in optical lattices,” *Phys. Rev. Lett.*, vol. 111, p. 185302, Oct 2013. [Online]. Available: <https://link.aps.org/doi/10.1103/PhysRevLett.111.185302>
- [177] M. Aidelsburger, M. Atala, M. Lohse, J. T. Barreiro, B. Paredes, and I. Bloch, “Realization of the hofstadter hamiltonian with ultracold atoms in optical lattices,” *Phys. Rev. Lett.*, vol. 111, p. 185301, Oct 2013. [Online]. Available: <https://link.aps.org/doi/10.1103/PhysRevLett.111.185301>
- [178] Y. Lahini, R. Pugatch, F. Pozzi, M. Sorel, R. Morandotti, N. Davidson, and Y. Silberberg, “Observation of a Localization Transition in Quasiperiodic Photonic Lattices,” *Phys. Rev. Lett.*, vol. 103, p. 013901, Jun 2009. [Online]. Available: <http://link.aps.org/doi/10.1103/PhysRevLett.103.013901>
- [179] O. Manela, M. Segev, D. N. Christodoulides, and D. Kip, “Hofstadter butterflies in nonlinear Harper lattices, and their optical realizations,” *New Journal of Physics*, vol. 12, no. 5, p. 053017, 2010. [Online]. Available: <http://stacks.iop.org/1367-2630/12/i=5/a=053017>
- [180] Z. Zhang, P. Tong, J. Gong, and B. Li, “Wave packet dynamics in one-dimensional linear and nonlinear generalized Fibonacci lattices,” *Phys. Rev. E*, vol. 83, p. 056205, May 2011. [Online]. Available: <http://link.aps.org/doi/10.1103/PhysRevE.83.056205>
- [181] M. Larcher, T. V. Lapyteva, J. D. Bodyfelt, F. Dalfovo, M. Modugno, and S. Flach, “Subdiffusion of nonlinear waves in quasiperiodic potentials,” *New Journal of Physics*, vol. 14, no. 10, p. 103036,

2012. [Online]. Available: <http://stacks.iop.org/1367-2630/14/i=10/a=103036>
- [182] K. M. Frahm and D. L. Shepelyansky, “Freed by interaction kinetic states in the harper model,” *The European Physical Journal B*, vol. 88, no. 12, p. 337, Dec 2015. [Online]. Available: <https://doi.org/10.1140/epjb/e2015-60733-9>
- [183] S. Flach, M. Ivanchenko, and R. Khomeriki, “Correlated metallic two-particle bound states in quasiperiodic chains,” *EPL (Europhysics Letters)*, vol. 98, no. 6, p. 66002, 2012. [Online]. Available: <http://stacks.iop.org/0295-5075/98/i=6/a=66002>
- [184] T. Guhr, A. Müller-Groeling, and H. A. Weidenmüller, “Random-matrix theories in quantum physics: common concepts,” *Physics Reports*, vol. 299, no. 4–6, pp. 189–425, 1998. [Online]. Available: <http://www.sciencedirect.com/science/article/pii/S0370157397000884>
- [185] S. Iyer, V. Oganesyan, G. Refael, and D. A. Huse, “Many-body localization in a quasiperiodic system,” *Phys. Rev. B*, vol. 87, p. 134202, Apr 2013. [Online]. Available: <https://link.aps.org/doi/10.1103/PhysRevB.87.134202>
- [186] J. M. G. Gomez, R. A. Molina, A. Relano, and J. Retamosa, “Misleading signatures of quantum chaos,” *Phys. Rev. E*, vol. 66, p. 036209, Sep 2002. [Online]. Available: <https://link.aps.org/doi/10.1103/PhysRevE.66.036209>
- [187] L. DAlessio and M. Rigol, “Long-time Behavior of Isolated Periodically Driven Interacting Lattice Systems,” *Phys. Rev. X*, vol. 4, p. 041048, Dec 2014. [Online]. Available: <https://link.aps.org/doi/10.1103/PhysRevX.4.041048>

- [188] V. Oganesyan and D. A. Huse, “Localization of interacting fermions at high temperature,” *Phys. Rev. B*, vol. 75, p. 155111, Apr 2007. [Online]. Available: <https://link.aps.org/doi/10.1103/PhysRevB.75.155111>
- [189] Y. Y. Atas, E. Bogomolny, O. Giraud, and G. Roux, “Distribution of the ratio of consecutive level spacings in random matrix ensembles,” *Phys. Rev. Lett.*, vol. 110, p. 084101, Feb 2013. [Online]. Available: <https://link.aps.org/doi/10.1103/PhysRevLett.110.084101>
- [190] O. Bohigas, M. J. Giannoni, and C. Schmit, “Characterization of chaotic quantum spectra and universality of level fluctuation laws,” *Phys. Rev. Lett.*, vol. 52, pp. 1–4, Jan 1984. [Online]. Available: <https://link.aps.org/doi/10.1103/PhysRevLett.52.1>
- [191] W. De Roeck, F. Huveneers, M. Müller, and M. Schiulaz, “Absence of many-body mobility edges,” *Phys. Rev. B*, vol. 93, p. 014203, Jan 2016. [Online]. Available: <https://link.aps.org/doi/10.1103/PhysRevB.93.014203>
- [192] O. Bohigas and M. Pato, “Missing levels in correlated spectra,” *Physics Letters B*, vol. 595, no. 1–4, pp. 171–176, 2004. [Online]. Available: <http://www.sciencedirect.com/science/article/pii/S0370269304008809>
- [193] S. Johri, R. Nandkishore, and R. N. Bhatt, “Many-body localization in imperfectly isolated quantum systems,” *Phys. Rev. Lett.*, vol. 114, p. 117401, Mar 2015. [Online]. Available: <https://link.aps.org/doi/10.1103/PhysRevLett.114.117401>
- [194] R. Nandkishore, S. Gopalakrishnan, and D. A. Huse, “Spectral features of a many-body-localized system weakly coupled to a bath,”

- Phys. Rev. B*, vol. 90, p. 064203, Aug 2014. [Online]. Available: <https://link.aps.org/doi/10.1103/PhysRevB.90.064203>
- [195] D. J. Thouless, “Quantization of particle transport,” *Phys. Rev. B*, vol. 27, pp. 6083–6087, May 1983. [Online]. Available: <https://link.aps.org/doi/10.1103/PhysRevB.27.6083>
- [196] J. K. Asbóth, L. Oroszlány, and A. Pályi, *A Short Course on Topological Insulators*. Springer International Publishing, 2016, vol. 919.
- [197] J. E. Avron and R. Seiler, “Quantization of the Hall Conductance for General, Multiparticle Schrödinger Hamiltonians,” *Phys. Rev. Lett.*, vol. 54, pp. 259–262, Jan 1985. [Online]. Available: <http://link.aps.org/doi/10.1103/PhysRevLett.54.259>
- [198] F. Mei, J.-B. You, D.-W. Zhang, X. C. Yang, R. Fazio, S.-L. Zhu, and L. C. Kwek, “Topological insulator and particle pumping in a one-dimensional shaken optical lattice,” *Phys. Rev. A*, vol. 90, p. 063638, Dec 2014. [Online]. Available: <http://link.aps.org/doi/10.1103/PhysRevA.90.063638>
- [199] P. Marra, R. Citro, and C. Ortix, “Fractional quantization of the topological charge pumping in a one-dimensional superlattice,” *Phys. Rev. B*, vol. 91, p. 125411, Mar 2015. [Online]. Available: <http://link.aps.org/doi/10.1103/PhysRevB.91.125411>
- [200] L. Zhou, D. Y. Tan, and J. Gong, “Effects of dephasing on quantum adiabatic pumping with nonequilibrium initial states,” *Phys. Rev. B*, vol. 92, p. 245409, Dec 2015. [Online]. Available: <http://link.aps.org/doi/10.1103/PhysRevB.92.245409>
- [201] R. W. Bomantara, G. N. Raghava, L. Zhou, and J. Gong, “Floquet topological semimetal phases of an extended kicked Harper model,”

- Phys. Rev. E*, vol. 93, p. 022209, Feb 2016. [Online]. Available: <http://link.aps.org/doi/10.1103/PhysRevE.93.022209>
- [202] M. Lohse, C. Schweizer, O. Zilberberg, M. Aidelsburger, and I. Bloch, “A Thouless quantum pump with ultracold bosonic atoms in an optical superlattice,” *Nat. Phys.*, vol. 12, no. 4, pp. 350–354, 04 2016. [Online]. Available: <http://dx.doi.org/10.1038/nphys3584>
- [203] S. Nakajima, T. Tomita, S. Taie, T. Ichinose, H. Ozawa, L. Wang, M. Troyer, and Y. Takahashi, “Topological Thouless pumping of ultracold fermions,” *Nat. Phys.*, vol. 12, no. 4, pp. 296–300, 04 2016. [Online]. Available: <http://dx.doi.org/10.1038/nphys3622>
- [204] M. Verbin, O. Zilberberg, Y. Lahini, Y. E. Kraus, and Y. Silberberg, “Topological pumping over a photonic Fibonacci quasicrystal,” *Phys. Rev. B*, vol. 91, p. 064201, Feb 2015. [Online]. Available: <http://link.aps.org/doi/10.1103/PhysRevB.91.064201>
- [205] R. Citro, N. Andrei, and Q. Niu, “Pumping in an interacting quantum wire,” *Phys. Rev. B*, vol. 68, p. 165312, Oct 2003. [Online]. Available: <http://link.aps.org/doi/10.1103/PhysRevB.68.165312>
- [206] I. L. Aleiner and A. V. Andreev, “Adiabatic Charge Pumping in Almost Open Dots,” *Phys. Rev. Lett.*, vol. 81, pp. 1286–1289, Aug 1998. [Online]. Available: <http://link.aps.org/doi/10.1103/PhysRevLett.81.1286>
- [207] J. Splettstoesser, M. Governale, J. König, and R. Fazio, “Adiabatic Pumping through Interacting Quantum Dots,” *Phys. Rev. Lett.*, vol. 95, p. 246803, Dec 2005. [Online]. Available: <http://link.aps.org/doi/10.1103/PhysRevLett.95.246803>
- [208] D. Fioretto and A. Silva, “Phase Coherence, Inelastic Scattering, and Interaction Corrections in Pumping Through Quantum Dots,”

- Phys. Rev. Lett.*, vol. 100, p. 236803, Jun 2008. [Online]. Available: <http://link.aps.org/doi/10.1103/PhysRevLett.100.236803>
- [209] E. Sela and Y. Oreg, “Adiabatic Pumping in Interacting Systems,” *Phys. Rev. Lett.*, vol. 96, p. 166802, Apr 2006. [Online]. Available: <http://link.aps.org/doi/10.1103/PhysRevLett.96.166802>
- [210] E. Berg, M. Levin, and E. Altman, “Quantized Pumping and Topology of the Phase Diagram for a System of Interacting Bosons,” *Phys. Rev. Lett.*, vol. 106, p. 110405, Mar 2011. [Online]. Available: <http://link.aps.org/doi/10.1103/PhysRevLett.106.110405>
- [211] D. Rossini, M. Gibertini, V. Giovannetti, and R. Fazio, “Topological pumping in the one-dimensional Bose-Hubbard model,” *Phys. Rev. B*, vol. 87, p. 085131, Feb 2013. [Online]. Available: <http://link.aps.org/doi/10.1103/PhysRevB.87.085131>
- [212] D. Meidan, T. Micklitz, and P. W. Brouwer, “Topological classification of interaction-driven spin pumps,” *Phys. Rev. B*, vol. 84, p. 075325, Aug 2011. [Online]. Available: <http://link.aps.org/doi/10.1103/PhysRevB.84.075325>
- [213] F. Letscher, F. Grusdt, and M. Fleischhauer, “Growing quantum states with topological order,” *Phys. Rev. B*, vol. 91, p. 184302, May 2015. [Online]. Available: <https://link.aps.org/doi/10.1103/PhysRevB.91.184302>
- [214] C. Cohen-Tannoudji, J. Dupont-Roc, and G. Grynberg, *Atom-Photon interaction: Basic process and application*. Wiley, New York (Chap B1.), 1998.
- [215] N. V. Vitanov, A. A. Rangelov, B. W. Shore, and K. Bergmann, “Stimulated raman adiabatic passage in physics, chemistry, and

- beyond,” *Rev. Mod. Phys.*, vol. 89, p. 015006, Mar 2017. [Online]. Available: <https://link.aps.org/doi/10.1103/RevModPhys.89.015006>
- [216] G. Vidal, “Efficient Classical Simulation of Slightly Entangled Quantum Computations,” *Phys. Rev. Lett.*, vol. 91, p. 147902, Oct 2003. [Online]. Available: <http://link.aps.org/doi/10.1103/PhysRevLett.91.147902>
- [217] S. Al-Assam, S. R. Clark, and D. Jaksch, “The tensor network theory library,” *Journal of Statistical Mechanics: Theory and Experiment*, vol. 2017, no. 9, p. 093102, 2017. [Online]. Available: <http://stacks.iop.org/1742-5468/2017/i=9/a=093102>
- [218] M. Leib, F. Deppe, A. Marx, R. Gross, and M. J. Hartmann, “Networks of nonlinear superconducting transmission line resonators,” *New Journal of Physics*, vol. 14, no. 7, p. 075024, 2012. [Online]. Available: <http://stacks.iop.org/1367-2630/14/i=7/a=075024>
- [219] J. Majer, J. M. Chow, J. M. Gambetta, J. Koch, B. R. Johnson, J. A. Schreier, L. Frunzio, D. I. Schuster, A. A. Houck, A. Wallraff, A. Blais, M. H. Devoret, S. M. Girvin, and R. J. Schoelkopf, “Coupling superconducting qubits via a cavity bus,” *Nature*, vol. 449, no. 7161, pp. 443–447, 09 2007. [Online]. Available: <http://dx.doi.org/10.1038/nature06184>
- [220] M. A. Sillanpaa, J. I. Park, and R. W. Simmonds, “Coherent quantum state storage and transfer between two phase qubits via a resonant cavity,” *Nature*, vol. 449, no. 7161, pp. 438–442, 09 2007. [Online]. Available: <http://dx.doi.org/10.1038/nature06124>
- [221] P. Macha, G. Oelsner, J.-M. Reiner, M. Marthaler, S. André, G. Schön, U. Hübner, H.-G. Meyer, E. Il’ichev, and A. V. Ustinov, “Implementation of a quantum metamaterial using superconducting

- qubits,” *Nature Communications*, vol. 5, pp. 5146 EP –, 10 2014. [Online]. Available: <http://dx.doi.org/10.1038/ncomms6146>
- [222] P. Jung, A. V. Ustinov, and S. M. Anlage, “Progress in superconducting metamaterials,” *Superconductor Science and Technology*, vol. 27, no. 7, p. 073001, 2014. [Online]. Available: <http://stacks.iop.org/0953-2048/27/i=7/a=073001>
- [223] V. Pierro and G. Filatrella, “Fabry–perot filters with tunable josephson junction defects,” *Physica C: Superconductivity and its Applications*, vol. 517, pp. 37 – 40, 2015. [Online]. Available: <http://www.sciencedirect.com/science/article/pii/S0921453415002373>
- [224] H. R. Mohebbi and A. H. Majedi, “Shock wave generation and cut off condition in nonlinear series connected discrete josephson transmission line,” *IEEE Transactions on Applied Superconductivity*, vol. 19, no. 3, pp. 891–894, June 2009.
- [225] J. Koch, T. M. Yu, J. Gambetta, A. A. Houck, D. I. Schuster, J. Majer, A. Blais, M. H. Devoret, S. M. Girvin, and R. J. Schoelkopf, “Charge-insensitive qubit design derived from the cooper pair box,” *Phys. Rev. A*, vol. 76, p. 042319, Oct 2007. [Online]. Available: <http://link.aps.org/doi/10.1103/PhysRevA.76.042319>
- [226] A. Nunnenkamp, J. Koch, and S. M. Girvin, “Synthetic gauge fields and homodyne transmission in jaynes–cummings lattices,” *New Journal of Physics*, vol. 13, no. 9, p. 095008, 2011.
- [227] A. J. Daley, “Quantum trajectories and open many-body quantum systems,” *Advances in Physics*, pp. 77–149, 2014.
- [228] M. Knap, E. Arrigoni, W. von der Linden, and J. H. Cole, “Emission characteristics of laser-driven dissipative coupled-cavity systems,”

- Phys. Rev. A*, vol. 83, p. 023821, Feb 2011. [Online]. Available: <https://link.aps.org/doi/10.1103/PhysRevA.83.023821>
- [229] M. Biondi, E. P. L. van Nieuwenburg, G. Blatter, S. D. Huber, and S. Schmidt, “Incompressible polaritons in a flat band,” *Phys. Rev. Lett.*, vol. 115, p. 143601, Sep 2015. [Online]. Available: <https://link.aps.org/doi/10.1103/PhysRevLett.115.143601>
- [230] H. Wilming, M. J. Kastoryano, A. H. Werner, and J. Eisert, “Emergence of spontaneous symmetry breaking in dissipative lattice systems,” *Journal of Mathematical Physics*, vol. 58, no. 3, p. 033302, 2017. [Online]. Available: <https://doi.org/10.1063/1.4978328>
- [231] X.-G. Wen, “Colloquium: Zoo of quantum-topological phases of matter,” *Rev. Mod. Phys.*, vol. 89, p. 041004, Dec 2017. [Online]. Available: <https://link.aps.org/doi/10.1103/RevModPhys.89.041004>
- [232] D. Pérez-García, M. M. Wolf, M. Sanz, F. Verstraete, and J. I. Cirac, “String order and symmetries in quantum spin lattices,” *Phys. Rev. Lett.*, vol. 100, p. 167202, Apr 2008. [Online]. Available: <https://link.aps.org/doi/10.1103/PhysRevLett.100.167202>
- [233] J. Haegeman, D. Pérez-García, I. Cirac, and N. Schuch, “Order parameter for symmetry-protected phases in one dimension,” *Phys. Rev. Lett.*, vol. 109, p. 050402, Jul 2012. [Online]. Available: <https://link.aps.org/doi/10.1103/PhysRevLett.109.050402>
- [234] M. Z. Hasan and C. L. Kane, “*Colloquium* : Topological insulators,” *Rev. Mod. Phys.*, vol. 82, pp. 3045–3067, Nov 2010. [Online]. Available: <http://link.aps.org/doi/10.1103/RevModPhys.82.3045>
- [235] X.-L. Qi and S.-C. Zhang, “Topological insulators and superconductors,” *Rev. Mod. Phys.*, vol. 83, pp. 1057–1110, Oct 2011. [Online]. Available: <http://link.aps.org/doi/10.1103/RevModPhys.83.1057>

- [236] Z.-C. Gu and X.-G. Wen, “Tensor-entanglement-filtering renormalization approach and symmetry-protected topological order,” *Phys. Rev. B*, vol. 80, p. 155131, Oct 2009. [Online]. Available: <http://link.aps.org/doi/10.1103/PhysRevB.80.155131>
- [237] X. Chen, Z.-C. Gu, and X.-G. Wen, “Local unitary transformation, long-range quantum entanglement, wave function renormalization, and topological order,” *Phys. Rev. B*, vol. 82, p. 155138, Oct 2010. [Online]. Available: <http://link.aps.org/doi/10.1103/PhysRevB.82.155138>
- [238] X. G. Wen, “Topological orders in rigid states,” *International Journal of Modern Physics B*, vol. 04, no. 02, pp. 239–271, 1990.
- [239] C. Nayak, S. H. Simon, A. Stern, M. Freedman, and S. Das Sarma, “Non-abelian anyons and topological quantum computation,” *Rev. Mod. Phys.*, vol. 80, pp. 1083–1159, Sep 2008. [Online]. Available: <https://link.aps.org/doi/10.1103/RevModPhys.80.1083>
- [240] N. Goldman, J. C. Budich, and P. Zoller, “Topological quantum matter with ultracold gases in optical lattices,” *Nat. Phys.*, vol. 12, pp. 639 EP –, 06 2016. [Online]. Available: <http://dx.doi.org/10.1038/nphys3803>
- [241] T. Ozawa, H. M. Price, A. Amo, N. Goldman, M. Hafezi, L. Lu, M. Rechtsman, D. Schuster, J. Simon, O. Zilberberg, and I. Carusotto, “Topological Photonics,” *ArXiv e-prints*, Feb. 2018.
- [242] L. Lu, J. D. Joannopoulos, and M. Soljačić, “Topological photonics,” *Nat. Photonics*, vol. 8, pp. 821 EP –, 10 2014. [Online]. Available: <http://dx.doi.org/10.1038/nphoton.2014.248>

- [243] E. G. Dalla Torre, E. Berg, and E. Altman, “Hidden order in 1d bose insulators,” *Phys. Rev. Lett.*, vol. 97, p. 260401, Dec 2006. [Online]. Available: <http://link.aps.org/doi/10.1103/PhysRevLett.97.260401>
- [244] E. Berg, E. G. Dalla Torre, T. Giamarchi, and E. Altman, “Rise and fall of hidden string order of lattice bosons,” *Phys. Rev. B*, vol. 77, p. 245119, Jun 2008. [Online]. Available: <http://link.aps.org/doi/10.1103/PhysRevB.77.245119>
- [245] D. Rossini and R. Fazio, “Phase diagram of the extended bose–hubbard model,” *New Journal of Physics*, vol. 14, no. 6, p. 065012, 2012. [Online]. Available: <http://stacks.iop.org/1367-2630/14/i=6/a=065012>
- [246] T. Kennedy and H. Tasaki, “Hidden symmetry breaking and the haldane phase ins=1 quantum spin chains,” *Communications in Mathematical Physics*, vol. 147, no. 3, pp. 431–484, 1992. [Online]. Available: <http://dx.doi.org/10.1007/BF02097239>
- [247] F. Pollmann, E. Berg, A. M. Turner, and M. Oshikawa, “Symmetry protection of topological phases in one-dimensional quantum spin systems,” *Phys. Rev. B*, vol. 85, p. 075125, Feb 2012. [Online]. Available: <http://link.aps.org/doi/10.1103/PhysRevB.85.075125>
- [248] B. Abdo, A. Kamal, and M. Devoret, “Nondegenerate three-wave mixing with the josephson ring modulator,” *Phys. Rev. B*, vol. 87, p. 014508, Jan 2013. [Online]. Available: <http://link.aps.org/doi/10.1103/PhysRevB.87.014508>
- [249] F. D. M. Haldane, “Nonlinear field theory of large-spin heisenberg antiferromagnets: Semiclassically quantized solitons of the one-dimensional easy-axis néel state,” *Phys. Rev. Lett.*, vol. 50, pp.

- 1153–1156, Apr 1983. [Online]. Available: <http://link.aps.org/doi/10.1103/PhysRevLett.50.1153>
- [250] M. den Nijs and K. Rommelse, “Preroughening transitions in crystal surfaces and valence-bond phases in quantum spin chains,” *Phys. Rev. B*, vol. 40, pp. 4709–4734, Sep 1989. [Online]. Available: <http://link.aps.org/doi/10.1103/PhysRevB.40.4709>
- [251] M. Oshikawa, “Hidden $z^2 \times z^2$ symmetry in quantum spin chains with arbitrary integer spin,” *Journal of Physics: Condensed Matter*, vol. 4, no. 36, p. 7469, 1992. [Online]. Available: <http://stacks.iop.org/0953-8984/4/i=36/a=019>
- [252] L. Mazza, D. Rossini, M. Endres, and R. Fazio, “Out-of-equilibrium dynamics and thermalization of string order,” *Phys. Rev. B*, vol. 90, p. 020301, Jul 2014. [Online]. Available: <http://link.aps.org/doi/10.1103/PhysRevB.90.020301>
- [253] M. Calvanese Strinati, L. Mazza, M. Endres, D. Rossini, and R. Fazio, “Destruction of string order after a quantum quench,” *Phys. Rev. B*, vol. 94, p. 024302, Jul 2016. [Online]. Available: <https://link.aps.org/doi/10.1103/PhysRevB.94.024302>
- [254] I. Carusotto, D. Gerace, H. E. Türeci, S. De Liberato, C. Ciuti, and A. Imamoglu, “Fermionized photons in an array of driven dissipative nonlinear cavities,” *Phys. Rev. Lett.*, vol. 103, p. 033601, Jul 2009. [Online]. Available: <http://link.aps.org/doi/10.1103/PhysRevLett.103.033601>
- [255] M. J. Hartmann, “Polariton crystallization in driven arrays of lossy nonlinear resonators,” *Phys. Rev. Lett.*, vol. 104, p. 113601, Mar 2010. [Online]. Available: <http://link.aps.org/doi/10.1103/PhysRevLett.104.113601>

- [256] R. O. Umucalilar and I. Carusotto, “Fractional quantum hall states of photons in an array of dissipative coupled cavities,” *Phys. Rev. Lett.*, vol. 108, p. 206809, May 2012. [Online]. Available: <http://link.aps.org/doi/10.1103/PhysRevLett.108.206809>
- [257] J. Jin, D. Rossini, R. Fazio, M. Leib, and M. J. Hartmann, “Photon solid phases in driven arrays of nonlinearly coupled cavities,” *Phys. Rev. Lett.*, vol. 110, p. 163605, Apr 2013.
- [258] T. Grujic, S. R. Clark, D. Jaksch, and D. G. Angelakis, “Repulsively induced photon superbunching in driven resonator arrays,” *Phys. Rev. A*, vol. 87, p. 053846, May 2013. [Online]. Available: <https://link.aps.org/doi/10.1103/PhysRevA.87.053846>
- [259] M. Fitzpatrick, N. M. Sundaresan, A. C. Y. Li, J. Koch, and A. A. Houck, “Observation of a dissipative phase transition in a one-dimensional circuit QED lattice,” *ArXiv e-prints*, Jul. 2016.
- [260] V. M. Bastidas, I. Omelchenko, A. Zakharova, E. Schöll, and T. Brandes, *Control of Self-Organizing Nonlinear Systems*. Cham: Springer International Publishing, 2016, ch. Chimera States in Quantum Mechanics, pp. 315–336. [Online]. Available: http://dx.doi.org/10.1007/978-3-319-28028-8_16
- [261] S. Al-Assam, S. Clark, D. Jaksch, and T. D. team, *Tensor Network Theory Library, Beta Version 1.1*, p. www.tensornetworktheory.org, 2016.

Appendix A

Field quantization: mode of a simple optical resonator

Let us consider an optical cavity consisting of two parallel perfectly reflecting mirrors, lying on the x-y plane at $z = 0$ and $z = L$. The electric field and the magnetic field inside the cavity take the form

$$\mathbf{E}(\mathbf{r}, t) = \mathbf{e}_x E_x(z, t), \quad (\text{A.1})$$

$$\mathbf{B}(\mathbf{r}, t) = \mathbf{e}_y B_y(z, t), \quad (\text{A.2})$$

respectively. By solving Maxwell's equations assuming the boundary conditions $E_x(0, t) = E_x(L, t) = 0$, we get

$$E_x^{(m)}(z, t) = E_0 \sin(\omega_c^{(m)} t) \sin(k_m z), \quad (\text{A.3})$$

$$B_y^{(m)}(z, t) = B_0 \cos(\omega_c^{(m)} t) \cos(kz), \quad (\text{A.4})$$

where $k_m = m\pi/L$, m is a positive integer, $\omega_c^{(m)} = ck_m$, c is the speed of light, E_0 is the amplitude of the electric field, and $B_0 = E_0/c$ is the amplitude of the magnetic field. The energy of the electromagnetic field

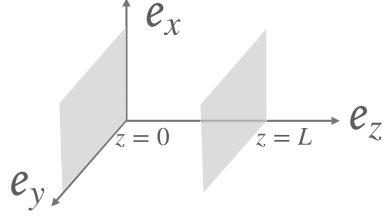


Fig. A.1. A sketch of a simplified optical cavity consisting of two plane mirrors at $z = 0$ and $z = L$.

inside the cavity is

$$\begin{aligned}
 E^{(m)} &= \frac{1}{2} \int dV \left[\epsilon_0 |E_x^{(m)}(z, t)|^2 + \frac{1}{\mu_0} |B_y^{(m)}(z, t)|^2 \right] \\
 &= \frac{1}{4} \epsilon_0 E_0^2 V (\sin^2(\omega_c^{(m)} t) + \cos^2(\omega_c^{(m)} t)) \\
 &= \frac{1}{2} [(p^{(m)}(t))^2 + (\omega_c^{(m)})^2 (q^{(m)}(t))^2], \tag{A.5}
 \end{aligned}$$

where V is the volume of the cavity, $q^{(m)}(t) = \sqrt{\frac{\epsilon_0 V}{2(\omega_c^{(m)})^2}} E_0 \sin(\omega_c^{(m)} t)$, and $p^{(m)}(t) = \sqrt{\frac{V}{2\mu_0}} B_0 \cos(\omega_c^{(m)} t)$. One can see that the energy $E^{(m)}$ takes the form of the energy of a simple Harmonic oscillator where $p^{(m)}(t)$ and $q^{(m)}(t)$ are position and momentum coordinates, respectively. From now on we will consider the lowest mode $m = 1$ and drop the superscript (m) .

Next, we perform second quantization by promoting $p(t)$ and $q(t)$ to operators, i.e.

$$E^{(m)} \rightarrow \hat{H}_{\text{cavity}} = \frac{1}{2} (\hat{p}^2 + \omega_c^2 \hat{q}^2), \tag{A.6}$$

where $[\hat{q}, \hat{p}] = i\hbar$. We then define the ladder operators as

$$\hat{a}^\dagger = \frac{\omega_c \hat{q} - i\hat{p}}{\sqrt{2\hbar\omega_c}}, \tag{A.7}$$

$$\hat{a} = \frac{\omega_c \hat{q} + i\hat{p}}{\sqrt{2\hbar\omega_c}}, \tag{A.8}$$

where $[\hat{a}, \hat{a}^\dagger] = 1$. The Hamiltonian is then written as $\hat{H}_{\text{cavity}} = \hbar\omega_c (\hat{a}^\dagger \hat{a} + \frac{1}{2})$ which is the form of a quantum harmonic oscillator. We will set $\hbar = 1$ for now on for simplicity.

Appendix B

Mean-field description for the interacting Harper model

To discuss the critical properties of the model Eq. [4.9], we resort on the mean field analysis [260]. With this aim, we consider a lattice with L sites and periodic boundary conditions $a_0 = a_{L-1}$. We introduce a new set of displaced bosonic operators

$$a_j = b_j + \alpha_j , \tag{B.1}$$

where a_m are the original bosonic operators, and b_m describes the quantum fluctuation about the mean field α_m .

Let us focus now on the particular case of a time independent phase $\phi(t) = \phi_0$ in Eq. [1] and $b = 1/3$. In this particular case, the one dimensional lattice is composed by $L/3$ trimers with on-site energies

$$\begin{aligned} \omega_A &= \omega_{3l} = \omega_0 + \Delta \cos \phi_0 \\ \omega_B &= \omega_{3l+1} = \omega_0 + \Delta \cos(\phi_0 + 2\pi/3) \\ \omega_C &= \omega_{3l+2} = \omega_0 + \Delta \cos(\phi_0 + 4\pi/3) . \end{aligned} \tag{B.2}$$

This motivates us to introduce the label $l \in \{0, \dots, L/3 - 1\}$ for each unit

cell or trimer. Within each trimer one has three species of bosons $b_{A,l} = b_{3l}$, $b_{B,l} = b_{3l+1}$ and $b_{C,l} = b_{3l+2}$ with a similar convention for the mean fields $\alpha_{A,l}$, $\alpha_{B,l}$ and $\alpha_{C,l}$. In the semi-classical limit $|\alpha_m| \gg 1$, one can consider the effect of the quantum fluctuations at a Gaussian level, which enables us to make the decomposition

$$\hat{H}_{\alpha} = \frac{L}{3} \mathcal{H}_{\text{Class}}(\alpha) + \hat{H}_{\text{Lin}}(\mathbf{b}, \alpha) + \hat{H}_{\text{Quad}}(\mathbf{b}, \alpha), \quad (\text{B.3})$$

where $\mathbf{b} = (b_0, \dots, b_{L-1})$, and $\alpha = (\alpha_0, \alpha_2, \dots, \alpha_{L-1})$. The terms $\hat{H}_{\text{Lin}}(\mathbf{b}, \alpha)$ and $\hat{H}_{\text{Quad}}(\mathbf{b}, \alpha)$ are linear and quadratic in the bosonic operators, respectively. In addition, if we assume that the mean field do not depend on the position l of the unit cell, we obtain the Hamilton function

$$\begin{aligned} \mathcal{H}_{\text{Class}}(\alpha) = & \omega_A |\alpha_A|^2 + \omega_B |\alpha_B|^2 + \omega_C |\alpha_C|^2 \\ & - J (\alpha_A^* \alpha_B + \alpha_B^* \alpha_C + \alpha_C^* \alpha_A + H.c.) \\ & + \frac{U}{2} [|\alpha_A|^2 (|\alpha_A|^2 - 1) + |\alpha_B|^2 (|\alpha_B|^2 - 1) + |\alpha_C|^2 (|\alpha_C|^2 - 1)]. \end{aligned} \quad (\text{B.4})$$

The quantum fluctuations are governed by the quadratic Hamiltonian

$$\begin{aligned} \hat{H}_{\text{Quad}}(\mathbf{a}, \alpha) = & \sum_{j=0}^{L-1} \left(\omega_j - \frac{U}{2} \right) b_j^\dagger b_j - J \sum_{j=0}^{L-2} \left(b_j^\dagger b_{j+1} + h.c. \right) \\ & + \frac{U}{2} \sum_{j=0}^{L-1} \left(|\alpha_j|^2 b_j^\dagger b_j + \alpha_j^2 (b_j^\dagger)^2 + (\alpha_j^*)^2 b_j^2 \right), \end{aligned} \quad (\text{B.5})$$

where $\alpha_{3l} = \alpha_A$, $\alpha_{3l+1} = \alpha_B$ and $\alpha_{3l+2} = \alpha_C$. One can interpret the Hamiltonian \hat{H}_{α} as the Hamiltonian in neighborhood of a stationary points of the energy landscape Eq. (B.4). To obtain the stationary points, we require vanishing linear bosonic terms in Eq. (B.3), i.e., $\hat{H}_{\text{Lin}}(\mathbf{a}, \alpha) = 0$. This conditions is satisfied as long as the mean fields α_A , α_B and α_C are a solution of the semi-classical equations of motion. The simplest solution to these equations is $\alpha_A = \alpha_B = \alpha_C = 0$. In this case, the Hamiltonian in

Eq. (B.5) takes a simple form

$$\hat{H}_{\text{Quad}}(\mathbf{a}, \boldsymbol{\alpha}) = \sum_{l=0}^{L/3-1} (\boldsymbol{\Psi}_l^\dagger)^T \mathcal{M} \boldsymbol{\Psi}_l + \sum_{l=0}^{L/3-2} J \left[(\boldsymbol{\Psi}_l^\dagger)^T \mathcal{N} \boldsymbol{\Psi}_{l+1} + H.c \right], \quad (\text{B.6})$$

where $(\boldsymbol{\Psi}_l^\dagger)^T = (b_{A,l}^\dagger, b_{B,l}^\dagger, b_{C,l}^\dagger)$. Correspondingly, the matrices are

$$\mathcal{M} = \begin{pmatrix} \omega_A - U/2 & -J & 0 \\ -J & \omega_B - U/2 & -J \\ 0 & -J & \omega_C - U/2 \end{pmatrix}, \quad \mathcal{N} = \begin{pmatrix} 0 & 0 & -J \\ 0 & 0 & 0 \\ -J & 0 & 0 \end{pmatrix}. \quad (\text{B.7})$$

We introduce here a discrete Fourier transformation $\boldsymbol{\Psi}_l = \sqrt{\frac{3}{L}} \sum_k \boldsymbol{\Phi}_k e^{ikl}$, where $(\boldsymbol{\Phi}_k^\dagger)^T = (b_{A,k}^\dagger, b_{B,k}^\dagger, b_{C,k}^\dagger)$, and $b_{\mu,l} = \sqrt{\frac{3}{L}} \sum_k b_{\mu,k} e^{ikl}$ with $\mu \in \{A, B, C\}$. Now we can write Hamiltonian Eq. (B.6) as $\hat{H}_{\text{Quad}}(\mathbf{a}, \boldsymbol{\alpha}) = \sum_k (\boldsymbol{\Phi}_k^\dagger)^T \mathbf{H}_k \boldsymbol{\Phi}_k$ with the Bogoliubov de Gennes Hamiltonian

$$\mathbf{H}_k = \begin{pmatrix} \omega_A - U/2 & -J & -J \cos k \\ -J & \omega_B - U/2 & -J \\ -J \cos k & -J & \omega_C - U/2 \end{pmatrix}. \quad (\text{B.8})$$

Finally, by considering $U = -J$, and by diagonalizing the Hamiltonian of Eq. (B.8), one obtains the excitation energies $E_{A,k}$, $E_{B,k}$, and $E_{C,k}$. From this, one can see that when $\omega_A = \omega_B = \omega_C$, we obtain gapless excitations and therefore, a quantum phase transition.

Appendix C

Numerical methods: matrix product states

Simulating quantum many-body systems exactly requires resources that grow exponentially with system size, and therefore we use approximate numerical methods. We use the matrix product state (MPS) representation and algorithms [26, 25] which have been shown to be very successful for 1D gapped systems. The MPS representation encodes the many-body wave function as a network of order-3 tensors, each possessing two internal indices of maximum dimension χ , and a physical index of dimension $(N_{\max} + 1)$ which represents the local Hilbert space. To see this. Here, N_{\max} is the maximum number of particles per site. The more entanglement there is in the system the larger χ must be to ensure accurate results. To see this, let consider a wave-function $|\psi\rangle$ that describes a quantum state of a one-dimensional system with L sites. We then label the first l site on the left as the subsystem A and the rest as the subsystem B. The wavefunction $|\psi\rangle$ according to Schmidt decomposition can be written as

$$|\psi\rangle = \sum_{\alpha=1}^{\chi_A} \lambda_{\alpha} |\Phi_{\alpha}^{[A]}\rangle |\Phi_{\alpha}^{[B]}\rangle, \quad (\text{C.1})$$

where $|\Phi_\alpha^{[A]}\rangle$ and $|\Phi_\alpha^{[B]}\rangle$ describe the state of the subsystem A and B respectively and λ_α is a Schmidt coefficient. In the following, we will also write $[A] = [1, 2, \dots, l]$ and $[B] = [l, l + 1, \dots, L]$. Starting with $l = 1$, we get

$$\begin{aligned} |\psi\rangle &= \sum_{\alpha_1}^{[1]} \lambda_{\alpha_1}^{[1]} |\Phi_{\alpha_1}^{[1]}\rangle |\Phi_{\alpha_1}^{[2, \dots, N]}\rangle \\ &= \sum_{\alpha_1, \sigma_1} \Gamma_{1, \alpha_1}^{[1] \sigma_1} \lambda_{\alpha_1}^{[1]} |\sigma_1\rangle |\Phi_{\alpha_1}^{[2, \dots, N]}\rangle, \end{aligned} \quad (\text{C.2})$$

where $|\Phi_{\alpha_1}^{[1]}\rangle = \sum_{\sigma_1} \Gamma_{1, \alpha_1}^{[1] \sigma_1} |\sigma_1\rangle$ and $|\sigma_1\rangle$ is the basis of a local system with dimension N . For example for a spin-1/2 we have $N = 2$ and $\{|\sigma_1\rangle\} = \{|\uparrow\rangle, |\downarrow\rangle\}$. Next we decompose the subsystem B $[2, \dots, N]$ into another two subsystems $[2]$ and $[3, \dots, N]$, i.e.

$$|\psi\rangle = \sum_{\alpha_1, \sigma_1, \sigma_2, \alpha_2} \Gamma_{1, \alpha_1}^{[1] \sigma_1} \lambda_{\alpha_1}^{[1]} \Gamma_{\alpha_1, \alpha_2}^{[2] \sigma_2} \lambda_{\alpha_2}^{[2]} |\sigma_1, \sigma_2\rangle |\Phi_{\alpha_2}^{[3, \dots, N]}\rangle. \quad (\text{C.3})$$

Iterating the above procedure, we get

$$\begin{aligned} |\psi\rangle &= \sum_{\{\sigma_i\}} c_{\sigma_1 \dots \sigma_N} |\sigma_1, \dots, \sigma_N\rangle \\ c_{\sigma_1 \dots \sigma_N} &= \sum_{\alpha}^{\chi} \Gamma_{1, \alpha_1}^{[1] \sigma_1} \lambda_{\alpha_1}^{[1]} \Gamma_{\alpha_1, \alpha_2}^{[2] \sigma_2} \lambda_{\alpha_2}^{[2]} \dots \Gamma_{\alpha_{N-1}, 1}^{[N] \sigma_N}. \end{aligned} \quad (\text{C.4})$$

Graphical representation of $c_{\sigma_1 \dots \sigma_N}$ is shown in Fig. C.1(a). This representation is exact when $\chi \rightarrow \infty$. Approximation can be made by truncating χ at a finite value.

Based on the MPS representation, the time evolution of a pure quantum state can be done using Time-Evolving Block Decimation (TEBD) [216, 217], shown in Fig. C.1(b)-(c). The idea is to consider a 1D Hamiltonian with nearest neighbour interactions $\hat{H} = \sum_{l=1}^L \hat{K}_1^{[l]} + \sum_{l=1}^L \hat{K}_2^{[l, l+1]}$, where $\hat{K}_1^{[l]}$ and $\hat{K}_2^{[l, l+1]}$ represent on-site Hamiltonian and nearest-neighbor

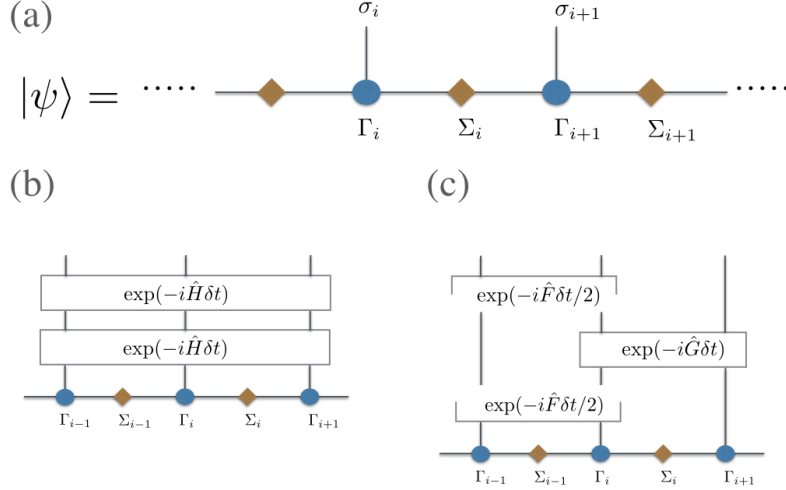


Fig. C.1. **(a)** A graphical representation of a matrix product state (MPS) representation of a quantum state in one dimension. Γ_i is a tensor of rank 3 with dimension $N \times \chi \times \chi$. Σ_i is a diagonal matrix containing Schmidt coefficients $\lambda_{\alpha_{i-1}, \alpha_i}^{[i]}$'s. **(b)** time evolution of the MPS with a full Hamiltonian \hat{H} . The error in this case goes as $\mathcal{O}(\delta t^2)$. **(c)** time evolution of the MPS with TEBD. The error in this case goes as $\mathcal{O}(\delta t^3)$.

Hamiltonian at site i , respectively. We then write

$$\hat{H} = \hat{F} + \hat{G}, \quad (\text{C.5})$$

$$\hat{F} = \sum_{\text{even}} \left(\hat{K}_1^{[l]} + \hat{K}_2^{[l, l+1]} \right), \quad (\text{C.6})$$

$$\hat{G} = \sum_{\text{odd}} \left(\hat{K}_1^{[l]} + \hat{K}_2^{[l, l+1]} \right), \quad (\text{C.7})$$

so that $[\hat{F}^{[l]}, \hat{F}^{[l']}] = [\hat{G}^{[l]}, \hat{G}^{[l']}] = 0$. The time evolution can be approximated as

$$\exp(-i\hat{H}t) = \prod_{n=1}^t \exp\left(-\frac{i}{2}\hat{F}\delta t\right) \exp(-i\hat{G}\delta t) \exp\left(-\frac{i}{2}\hat{F}\delta t\right) + \mathcal{O}(\delta t^3), \quad (\text{C.8})$$

where δt is small timestep and the error goes as δt^3 .

For dissipative dynamics, we solve the Lindblad Master equation using quantum trajectories [227]. Since each trajectory is the time evolution of a pure state, the latter can also be performed efficiently within the TEBD framework. Our implementation of the above methods is based on the

open-source Tensor Network Theory (TNT) library [261]. We found that the results shown in Chapter 4 and Chapter 5 can be sufficiently simulated with $\chi = 100$ and $N_{\max} = 4$. Time evolution is discretized in the timestep of $\delta t = 0.02/J$ and for the dissipative dynamics, time evolution of the density matrix is calculated by averaging over $M = 1000$ trajectories. We observed that increasing χ , N_{\max} , M and reducing δt further do not lead to any significant changes in our results.

